# STRUCTURES AND DYNAMICS OF STEREOISOMERIC POLY(PROPYLENE), POLY(PROPYLENE-CO-1-BUTENE) AND END-FUNCTIONALIZED POLY(CIS-1,4-ISOPRENE)

**Natchamon Sukhonthamethirat**

**A Thesis Submitted in Partial Fulfillment of the Requirements for the**

**Degree of Master of Science in Chemistry**

**Suranaree University of Technology**

**Academic Year 2020**

# การศึกษาโครงสร้างและพลวัตของพอลิ(โพรพิลิน)ที่มีไอโซเมอร์เชิงโครงสร้าง, พอลิ(โพรพิลิน-โค-1-บิวทีน) และพอลิ(ซิส-1,4-ไอโซพรีน) ที่มีการปรับแต่งหมู่ฟังก์ชันปลาย

**นางสาวนัชชามนต์ สุคนธเมธีรัตน์**

**วิทยานิพนธ์นี้เป็นส่วนหนึ่งของการศึกษาตามหลักสูตรปริญญาวิทยาศาสตรมหาบัณฑิต**
**สาขาวิชาเคมี**
**มหาวิทยาลัยเทคโนโลยีสุรนารี**
**ปีการศึกษา 2563**

# STRUCTURES AND DYNAMICS OF STEREOISOMERIC POLY(PROPYLENE), POLY(PROPYLENE-CO-1-BUTENE) AND END-FUNCTIONALIZED POLY(CIS-1,4-ISOPRENE)

Suranaree University of Technology has approved this thesis submitted in partial fulfillment of the requirements for a Master's Degree.

Thesis Examining Committee

(Prof. Dr. James R. Ketudat-Cairns)
Chairperson

(Assoc. Prof. Dr. Visit Vao-soongnern)
Member (Thesis Advisor)

(Prof. Dr. Kritsana Sagarik)
Member

(Assoc. Prof. Dr. Chaiwat Ruksakulpiwat)
Member

(Assoc. Prof. Dr. Piyarat Nimmanpipug)
Member

(Assoc. Prof. Flt. Lt. Dr. Kontorn Chamniprasart)
Vice Rector for Academic Affairs
and Internationalization

(Assoc. Prof. Dr. Worawat Meevasana)
Dean of Institute of Science

นัชชามนต์ สุคนธเมธีรัตน์ : การศึกษาโครงสร้างและพลวัติของพอลิ(โพรพิลิน) ที่มีไอโซเมอร์เชิงโครงสร้าง, พอลิ(โพรพิลิน-โค-1-บิวทีน) และพอลิ(ซิส-1,4-ไอโซพรีน) ที่มีการปรับแต่งหมู่ฟังก์ชันปลาย (STRUCTURES AND DYNAMICS OF STEREOISOMERIC POLY(PROPYLENE), POLY(PROPYLENE-CO-1,4-BUTENE) AND END-FUNCTIONALIZED POLY(CIS-1,4-ISOPRENE)) อาจารย์ที่ปรึกษา : รองศาสตราจารย์ ดร.วิสิษฐ์ แววสูงเนิน, 181 หน้า.

วิทยานิพนธ์เล่มนี้ประกอบด้วยสามหัวข้อ ในส่วนแรกคือการศึกษาผลของข้อบกพร่องจาก 1-บิวทีน บางส่วนต่อการตกผลึกและสัณฐานวิทยาของไอโซแทกทิกพอลิ(โพรพิลิน) (*i*PP) ด้วยเทคนิคกล้องจุลทรรศน์ออปติคอลโพลาไรซ์ (POM) เครื่องวัดความร้อนแบบดิฟเฟอเรนเชียลสแกน (DSC) และการกระเจิง/การเลี้ยวเบนของรังสีเอกซ์จากแสงซินโครตรอนในมุมแคบ/มุมกว้าง (SAXS/WAXD) ตัวอย่างของโฮโมพอลิเมอร์ *i*PP คือ V30G และตัวอย่างที่มีข้อบกพร่องของ 1-บิวทีน คือ MT12-s และ MT18-s จากการศึกษาการตกผลึกที่อุณหภูมิคงที่พบว่า ข้อบกพร่อง 1-บิวทีน มีผลกระทบบางอย่างต่อการก่อตัวและขนาดของสเฟียรูไลต์และเร่งกระบวนการตกผลึกของ iPP รวมถึงระดับของการตกผลึกจะต่ำกว่าสำหรับพอลิโพรพิลินที่มีหมู่กิ่งสั้นซึ่งสังเกตได้จากการทดลอง DSC SAXS และ WAXD ส่วนของผลึก (L) และส่วนที่รวมกันของผลึกและอสัณฐาน (long period, D) มีค่าเพิ่มขึ้นแต่อัตราส่วน L/D มีขนาดลดลงสำหรับพอลิโพรพิลินที่มีหมู่กิ่งสั้น

ต่อจากนั้นเป็นการศึกษาผลของน้ำหนักโมเลกุลผสมแบบ bimodal และข้อบกพร่องที่ผิดปกติของสเตอริโอต่อการตกผลึกของแบบจำลองโพลีเอทิลีน (PE) และ *i*PP ซึ่งศึกษาด้วยเทคนิคการจำลองแบบมอนติคาร์โล (MC) ในส่วนนี้มีการสร้าง monodisperse PE ส่วนผสมของ bidisperse PE และ iPP ที่มีข้อบกพร่องเกี่ยวกับสเตอริโอผิดปกติเพียงเล็กน้อยโดยใช้โมเลกุลแบบหยาบบนโครงตาข่ายที่มีเลขโคออร์ดิเนชันสูง ผลการจำลองพบว่า monodisperse PE สามารถทำได้สมบูรณ์ภายในเวลาคำนวณที่เหมาะสมและมีการแยกเฟสระหว่างโซ่สั้นและยาวก่อนที่จะเริ่มการตกผลึกสำหรับ bidisperse PE หากองค์ประกอบของโซ่สั้นมีจำนวนมากพอจะส่งผลให้โซ่ที่สั้นกว่ากลายเป็นผลึกได้เร็วกว่าส่วนประกอบโซ่ยาว ในส่วนของระบบ iPP ข้อบกพร่องของ racemic ขัดขวางการก่อตัวของผลึกแบบเกลียว $3_1$ รวมทั้งชะลอการตกผลึกและลดแนวโน้มการตกผลึก การศึกษาโครงสร้างที่ถูกล้อมรอบและเชิงพลวัตของคาร์บอกซิเลตพอลิ(ซิส-1,4-ไอโซพรีน) และพอลิ(ซิส-1,4-ไอโซพรีน) ที่มีการปรับแต่งฟังก์ชันหมู่ปลาย โดยไอออน $Li^+$, $K^+$ หรือ $Ca^{2+}$ ถูกศึกษาด้วยเทคนิคโมเลกูลาร์ไดนามิกส์ (MD) แต่สำหรับการทดลอง EXAFS จะใช้เฉพาะ $K^+$ และ $Ca^{2+}$

รูปแบบ EXAFS ของ $(PI_{30}COO)_2Ca$ และ $PI_{30}COOK$ ถูกเปรียบเทียบกับสารมาตรฐานที่รู้จักโครงสร้างของผลึกที่แน่นอน เช่น แคลเซียมอะซิเตท $(CH_3COO)_2Ca$ และ โพแทสเซียมฟอเมต (HCOOK) ซึ่งพบว่าโครงสร้างของตัวอย่างที่ศึกษาทั้งสองตัวอย่างมีโครงสร้างแตกต่างจากผลึกอ้างอิงเนื่องจากจำนวนโคออร์ดิเนชันของอะตอมออกซิเจนรอบไอออนบวกต่างกัน ดังนั้นจึงใช้วิธีการหาโครงสร้างที่เหมาะสมของสเปกตรัมของ EXAFS โดยใช้พิกัดอะตอมที่ถูกเลือกซึ่งสร้างขึ้นโดยเทคนิค MD จากผลของ MD-EXAFS นี้ พบว่าอะตอมแคลเซียมใน $(PI_nCOO)_2Ca$ จะถูกล้อมรอบด้วยอะตอมออกซิเจนห้าอะตอม ซึ่งมาจากหมู่คาร์บอกซิเลทสี่โมเลกุล โดยสามโมเลกุลให้ออกซิเจนหนึ่งอะตอมและอีกหนึ่งโมเลกุลให้ออกซิเจนสองอะตอม สำหรับกรณีของ $PI_nCOOK$ นั้น เปลือกโคออร์ดิเนชันแรกของอะตอมโพแทสเซียมถูกล้อมรอบด้วยออกซิเจนสี่อะตอมซึ่งมาจากหมู่คาร์บอกซิเลทสองโมเลกุลที่ให้ออกซิเจนรวมทั้งหมดสี่อะตอม

สาขาวิชาเคมี

ปีการศึกษา 2563

ลายชื่อนักศึกษา ปัชชาวณต์ สุคนธเมธีรัตน์

ลายชื่ออาจารย์ที่ปรึกษา

NATCHAMON SUKHONTHAMETHIRAT: STRUCTURES AND DYNAMICS OF STEREOISOMERIC POLY(PROPYLENE), POLY(PROPYLENE-CO-1,4-BUTENE) AND END-FUNCTIONALIZED POLY(CIS-1,4-ISOPRENE). THESIS ADVISOR: ASSOC. PROF. VISIT VAO-SOONGNERN, Ph.D. 181 PP.

IPP/G-RESIN/PE/PICOOM/CRYSTALLIZATION/MONTE CARLO SIMULATION/EXAFS/MOLECULAR DYNAMICS SIMULATIONS

There are three parts in this thesis. The first part is to investigate the effect of some 1-butene defects on crystallization and phase morphology of isotactic polypropylene (*i*PP) via polarized optical microscopy (POM), differential scanning calorimeter (DSC) and synchrotron small- and wide-angle X-ray scattering/diffraction (SAXS/WAXD). The sample of *i*PP homopolymer is V30G and samples with short-branched defects are MT12-s and MT18-s. From isothermal crystallization, 1-butene defects have some impact on the formation and size of spherulites and accelerate the crystallization process of *i*PP. The degree of crystallinities are lower for short branched PP, which were observed by DSC, SAXS and WAXD. Both crystalline (L) and the long period (D; amorphous + crystalline thickness) are increased, but the L/D ratio is decreased for short branched PP.

The effect of bimodal mixed molecular weight and stereo-irregular defects on crystallization of polyethylene (PE) and *i*PP models are studied by Monte Carlo (MC) simulation. In this part, the monodisperse PE, bidisperse PE mixtures and *i*PP with few

stereo-irregular defects were created based on the coarse-grained chains on a high coordination lattice. The results showed that monodisperse PE can be achieved within reasonable computational time and there is phase separation between short and long chains before crystallization starts for bidisperse PE. The shorter chains crystallize faster than the long chain components, if their composition is high enough. For *i*PP systems, the racemic defects hinder the formation of $3_1$ helices, retard the crystallization and decrease the crystallization tendency.

The solvation structure and dynamics of cation-doped carboxylated poly(cis-1,4-isoprene), PICOOM (where M is $Li^+$, $K^+$ or $Ca^{2+}$ were used for Molecular Dynamic (MD) studies but only $K^+$ and $Ca^{2+}$ were used for EXAFS experiments). The EXAFS patterns of $(PI_{30}COO)_2Ca$ and $PI_{30}COOK$ were compared with standard materials, which have known crystal structures *i.e.* calcium acetate $(CH_3COO)_2Ca$ and potassium formate (HCOOK). The solvation structure of $(PI_{30}COO)_2Ca$ and $PI_{30}COOK$ should be different from the reference crystals, because the coordination number of the oxygen atoms around the cation were different. So, a procedure of the fitting EXAFS spectra using the selected atomic coordinates generated by molecular dynamic trajectories were used. From the MD-EXAFS fitting results, there have four carboxyl groups with three groups that give one oxygen each and the other gives two oxygens to solvate the $Ca^{2+}$ ion to give the average number about 5.4 oxygen atoms for the $(PI_nCOO)_2Ca$ system. In the case of $PI_nCOOK$, the first coordination shell of the $K^+$ ion is mainly from two carboxyl groups with give four oxygens to solvate.

School of Chemistry

Academic Year 2020

Student's Signature ฉัชชานนท์ สุคนธเวชรัตน์

Advisor's Signature

# ACKNOWLEDGEMENTS

I am grateful to my thesis advisor, Assoc. Prof. Dr. Visit Vao-Soongnern, for his valuable advice, comments for research work and for kindness and suggestions about positive thinking. I am also very thankful for thesis examining committee for reading and comments throughout the entire thesis. Special thanks for Prof. Hiroshi Watanabe, Institute for Chemical Research, Kyoto University, Japan, for calcium and potassium carboxylate salt polyisoprene samples and valuable advice. I would like to express my sincere thanks to Prof. Shinichi Sakurai and his students at the Department of Polymer Science and Engineering, Kyoto Institute of Technology, Japan, for his valuable suggestions, instruments and software to analyze SAXS/WAXD data and Ms. Neha Manojkumar Mulchandini for NMR spectra, which is an important part of this research. I would like to thanks to the Beijing Research Institute of Chemistry and Industry, SINOPEC, China for polypropylene samples.

I am thankful to all members in Laboratory of Computational and Applied of Polymer Science (LCAPS), and all graduate students in the School of Chemistry, SUT for their support, encouragement and making this a fun time.

I would like to thank the Synchrotron Light Research Institute (Public Organization) for SAXS/WAXD and EAXFS measurements.

Last, but certainly not least, I would like to thank my beloved family who provided support, believe and encouragement.

Natchamon Sukhonthamethirat

# CONTENTS

**Page**

**CHAPTER**

# CONTENTS (Continued)

**Page**

# CONTENTS (Continued)

**Page**

# CONTENTS (Continued)

**Page**

# LIST OF TABLES

**Table** **Page**

# LIST OF TABLES (Continued)

**Table** **Page**

# LIST OF FIGURES

# LIST OF FIGURES (Continued)

**Figure** **Page**

# LIST OF FIGURES (Continued)

**Figure** **Page**

# LIST OF FIGURES (Continued)

**Figure** **Page**

# LIST OF FIGURES (Continued)

# LIST OF FIGURES (Continued)

**Figure** **Page**

# LIST OF FIGURES (Continued)

**Figure** **Page**

# LIST OF FIGURES (Continued)

**Figure** **Page**

# LIST OF ABBREVIATIONS

| | |
|---|---|
| $\emptyset_{\mathrm{DSC}}$ | Degree of crystallinity from DSC |
| $t_0$ | Induction period |
| $T_m^0$ | Equilibrium melting temperature |
| $\phi_{\mathrm{WAXD}}$ | Degree of crystallinity from WAXD |
| $E_0$ | Absorption edge energy |
| $S_0^2(k)$ | Amplitude of the reduction factor |
| $m_e$ | Electro mass |
| $\sigma_j$ | Debye-Waller factor |
| $\phi_{ij}$ | Photoelectron phase shift |
| $< R_g^2 >$ | Mean Square Radius of Gyration |
| $<\mathbf{m}(t).\mathbf{m}(0)>$ | Orientational autocorrelation function of bond vector |
| $<\mathbf{R}(t).\mathbf{R}(0)>$ | Chain end-to-end vector orientational autocorrelation |
| $\Delta H_m^0$ | Enthalpy of fusion at 100% |
| *2nnd* | The Second Nearest Neighbor Diamond |
| Å | Angstroms |
| ACF | Autocorrelation Function |
| *a*PP | Atactic polypropylene |
| Bz | Benzene |
| CN | Coordination number |
| $d_{ac}$ | Long spacing |

# LIST OF ABBREVIATIONS (Continued)

| | |
|---|---|
| $d_c$ | Crystalline thickness |
| DPE | Diphenylethylene |
| DSC | Differential Scanning Calorimetry |
| elPP | Elastomeric polypropylene |
| EM | Energy Minimization |
| EXAFS | Extended X-ray Absorption Fine Structure function |
| GPC | Gel Permeation Chromatography |
| *h* | Planck's constant |
| H(t) | Enthalpy of crystallization |
| HDPE | High density polyethylene |
| *i*PB | Isotactic poly(1-butene) |
| *i*PP | Isotactic polypropylene |
| iPPBu | Polypropylene random copolymer with 1-butene |
| iPPEt | Polypropylene random copolymer with ethylene |
| *k* | Crystallization rate constant |
| L | Sample-to-detector distance |
| $L_c$ or L | Average lamellar thickness |
| LDPE | Low density polyethylene |
| LINCS | Linear Constraint Solver |
| LJ | Lennard-Jones |

# LIST OF ABBREVIATIONS (Continued)

| | |
|---|---|
| $L_p$ or D | Long period |
| MC | Monte Carlo |
| MCS | Monte Carlo Step |
| MD | Molecular Dynamic |
| MFR | Melt Flow Rate |
| mm | millimeter |
| Mn | Number average molecular weight |
| $M_n(j)$ | Intramolecular bond orientation correlation functions |
| MSD | Mean Square Displacement |
| Mw | Weight average molecular weight |
| $n$ | Avrami exponent |
| nm | nanometer |
| NMR | Nuclear Magnetic Resonance |
| NR | Natural rubber |
| OCAF | Orientation Autocorrelation Function |
| PCF | Pair Correlation Function |
| PDI | Polydispersity index |
| PE | Polyethylene |
| PI | Poly (cis-1,4-isoprene) |
| PI-COOH | End-carboxylated polyisoprene |
| PICOOM | Cation-doped carboxylate polyisoprene |

# LIST OF ABBREVIATIONS (Continued)

| | |
|---|---|
| PME | Fast Particle Mesh Ewald |
| POM | Polarized Optical Microscopy |
| PP | Polypropylene |
| q | Scattering vector |
| RCF | Rotational Correlation Function |
| RDF, g(r) | Radial Distribution Function |
| RIS | Rotational Isomeric State |
| RSF | Radial Structure Function |
| SAXS | Small Angle X-ray Scattering |
| $S_G$ | Global orientation order parameter |
| $S_L$ | Local intermolecular |
| *s*PP | Syndiotactic polypropylene |
| $t_{0.5}$ | Crystallization half-time |
| $T_c$ | Crystallization temperature |
| THF | Tetrahydrofuran |
| $T_i$ | Crystallization onset temperature |
| $T_m$ | Melting temperature |
| $T_p$ | Crystallization peak temperature |
| WAXD | Wide Angle X-ray Diffraction |
| XRD | X-Ray Diffractometer |
| $\Delta H_c$ | Crystallization enthalpy |

# LIST OF ABBREVIATIONS (Continued)

| | |
|---|---|
| λ | Wavelength |
| μ | Absorption coefficient |
| $X(\mathrm{T})$ | Fraction of temperature |
| $\gamma(r)$ | Correlation function |

# CHAPTER I

# INTRODUCTION

A polymer is macromolecule that is composed of many repeating units called monomers. One polymer molecule may comprise $10^2$ to $10^6$ of monomers and the structure can be linear or non-linear such as branched or network. As there are a number of different types of polymers, there are also a lot of different characteristics, which can be found in nature or created through synthesis. Polymers can be classified in several ways. In particular, the classification based on their molecular structure can be done as following:

- **Polymers with only one monomer type**: The structures of these polymers are similar to a long straight chain composed of identical units connected to each other. The repeating units are usually linked together with covalent bonds to form a long molecule.
- **Polymers with two or more monomer types/chemical groups**: The polymer may have branched structure, in which monomers are placed at random position to form a linear molecule or having functional groups linked to the ended unit. In the first case, monomers are linked together to form a long molecule with some branched chains of different composition. Because of these branches, the polymers are less dense packed. For the second case, polymer chain ends are chemically.

modified or functionalized using the reactive group which can interact via intermolecular interaction such as hydrogen bonding.

Structural and dynamic properties of polymers with different types of defect groups are investigated including: (1) molecular simulation of the crystallization of monodisperse and bi-disperse polyethylene mixtures, (2) molecular simulation of isotactic polypropylene with some stereo-irregular defects, (3) experimental studies of the crystallization characteristics of isotactic polypropylene (*i*PP) with 1-butene defect and (4) molecular simulation of end-carboxylated polyisoprene (PI-COOH) and its salt complexes with $K^+$ and $Ca^{2+}$ ions.

## 1.1 Polyethylene (PE): monodispersed and bi-dispersed PE mixtures

PE is a main type of thermoplastic polymers, created by the addition or radical polymerization of ethylene (olefin) monomers. Polymerization of PE was carried out by Ziegler-Natta and metallocene catalysts. Normally, PE is a lightweight, durable plastic with many crystalline structures and it is one of the most widely used plastics. Many different types of polyethylene exist, with the chemical formula $(C_2H_4)_n$ and usually a mixture of similar chains with different values of *n*. For example, high density polyethylene (HDPE) is used for products including garbage bins, detergent bottles and water pipelines. Low density polyethylene (LDPE) is used as rigid containers and plastic film. The effect of molecular parameters, for example, polymer molecular weight, chain stiffness and polydispersity can affect polymer crystallization. In this thesis, crystallization of short PE will be studied in comparison between mono- and bi-dispersed PE (mixture of short and long chain) on the characteristics of structural formation.

## 1.2 Isotactic polypropylene (*i*PP) with stereo-irregular defects

Isotactic polypropylene (*i*PP) is a thermoplastic polymer applied in many daily life applications. It is prepared via chain-growth polymerization from propylene monomer. It was firstly synthesized by Natta et al. *i*PP has been studied for many years owing to its scientific and commercial importance. Due to advanced metallocene catalysts, a new polymer local structure with new material properties can be achieved by controlling the chain tacticity to provide the properties that can range from semi-crystalline to elastic thermoplastic. In this regard, the effect of chain stereo-defects on the structural properties of polypropylene, especially on its crystallization behavior, has received more interest (Dietrich, 1999; Dietrich, 2000; Lehmus, 2000; Rieger, 2002; Hiltner, 2003; Deisenhofer, 2003 and Cobzaru, 2005). *i*PP can form crystal morphology with three different patterns: a-monoclinic, b-hexagonal and c-orthorhombic. The difference in chain arrangement is dependent on different crystallization environment, such as pressure, thermal treatments and chain tacticity. Furthermore, another morphology of *i*PP with an intermediate degree of order (between crystalline and amorphous) can be obtained by rapidly cooling *i*PP from melt. The disordered phase either "*smectic phase,*" "*paracrystalline,*" or "*mesomorphic phase*", as described by Natta *et al*. (Natta, 1960), reflects a combination of parallel helices with more sequences along the chain axes rather than in the side packing. Another interesting case is polypropylene (PP) that has atactic and isotactic blocks within a molecule. The material is termed stereo-block or elastomeric polypropylene (elPP) as the isotactic blocks can crystallize if the chains are length enough, but the atactic blocks prefer to be amorphous even at low temperature. Some polymers exhibit homogeneous solubility in isotacticity that are reported by Collins and coworkers (Gauthier, 1995 and Bravakis, 1998) and by Chien et al. (Chien, 1997). In contrast, the heterogeneous isotacticity, provided by Waymouth's group (Yu, 1998), show the separating samples with the probability of *meso* pentad (Pmmmm) of 0.32 to three fractions with Pmmmm = 0.18, 0.33, and 0.51. These three fractions and the newly created samples have different properties.

## 1.3 Poly(propylene-ran-1-butene) copolymer

Isotactic polypropylene (*i*PP), firstly synthesized by Natta et al. (Natta, 1995 and Corradini, 2003) possesses interesting aspects like high strength, excellent chemical resistance, good process ability and low price (Lu, 2000). However, the PP has limited applications because of its poor impact strength, especially at low temperatures. There are numerous attempts to improve the impact properties of PP resins through physical or chemical methods. Improving the impact strength of PP resins is one of the most effective methods of physical blending with elastomers. Isotactic poly(1-butene) (*i*PB), has some advantages compared to *i*PP, such as excellent resistance to creep, good environmental stress cracking resistance, high impact strength and high temperature resistance. Copolymerization of 1-butene units with *i*PP chains in a random pattern might be a possible method to improve the properties of *i*PP (Shao, 2016).

Random polypropylene/1-butene copolymer from gas-phase and bulk processes were developed by Machado et al. (Machado, 2005; Machado, 2006 and Machado, 2008). It is possible to produce propylene/1-butene random copolymers in semi-batch gas-phase polymerizations using high activity Ziegler–Natta catalysts (Machado, 2005). In addition, 1-butene can be incorporated to polymer chain over the whole range of copolymer compositions during liquid pool polymerizations (Machado, 2006). In both cases, polymer materials have a lower melting temperature when 1-butene is randomly incorporated into polymer chains with a high polymerization rate. Machado et al. (Machado, 2008) also prepared a new set of polypropylene/1-butene blends through *in situ* sequential two-stage polymerizations, using a high-activity $MgCl_2$/Ziegler–Natta catalyst.

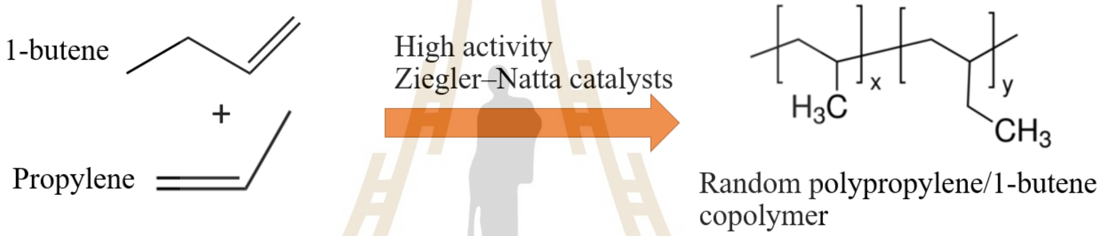

**Figure 1.1** Schematic represents the synthesis of propylene/1-butene random copolymer.

A commercial product of iPP based copolymers, G-resin is a SINOPEC thermoplastic brand of iPP with a certain amount of 1-butene. It has high transparency and a relatively low soluble content for food packages and medical items. The better property of G-resin than iPP is based on lower crystallinity caused by 1-butene comonomers. The comonomers also creates the confinement effect on the crystallization behaviors of statistical polyolefin copolymers (Hu, 2016) In this proposal, we will study and compare the crystallization characteristics of these samples to understand the effect of 1-butene defects on polymer crystallization from the molten state.

## 1.4 PICOOH and PICOO$^-$ doped with cation

Poly (cis-1,4-isoprene) (PI) or natural rubber (NR) is one of the most well-known natural polymers that can be harvested from the sap of the *hevea brasiliensis*. It can also be made by Ziegler-Natta polymerization. It has a monomer that is made from two carbon-carbon double bonds in the backbone chain, known as the diene polymer. In order to develop for new properties, it is interesting to examine chemically modified PI chains designed to have specific intermolecular interaction. Recently, short PI chain having an associative carboxyl group at one end (PI-COOH) was synthesized at Institute for Chemical Research, Kyoto University (Matsumiya, 2016). The aim of this work is to study dynamic properties of mono-functional head-to-head association and dissociation of short PICOOH chain in comparison between theory and experiment. For the experimental part, a high-cis linear PI was synthesized via living anionic polymerization. Then, the anion ends of the PI chains can be obtained by modifying to carboxylic (COOH) groups through reaction with carbon dioxide ($CO_2$). The study of dynamics of the associating/dissociating showed that viscoelastic behavior of those diluted PI-COOH and reference samples correspond to theoretical calculations and the viscoelastically detected association/dissociation is greatly affected by PI-COOH chain characteristics. In addition to the past work of the Kyoto group, we are interested in the situation when the carboxylate ended-group is neutralized by counter cations with an aim to elucidate the atomistic solvation structure of cation using combined experiment and molecular simulation methods.

This work is a part of the collaborative research on associating polymers based on a combination method of experimental, theoretical and simulation methods between the Institute for Chemical Research, Kyoto University and the School of Chemistry, Suranaree University of Technology. Associating polymers is interesting because of their scientific novelty and industrial applications (Leibler, 1991; Rubinstein, 1998; Kumar, 2001; Rubinstein, 2001; Noro, 2008; Noro, 2009; van Ruymbeke, 2010; Lei, 2012; Chen, 2013; Chen, 2015 and Ahmadi, 2015). For polymer chains having functional groups that can be reversibly associating/dissociating, diverse rheological responses arise from the position and amount of those groups and the lifetime in relation to the chain relaxation time. The competition between the association/dissociation and the chain motion determined the dynamics of those polymer chains. Chain relaxation is greatly dampened by the reaction, making the reaction much slower than large-scale intrinsic chain motion. Focusing on the PICOO- doped with cations, the coordination number, disorder of neighboring atoms and distance of neighboring atoms were measured using the extend X-ray absorption fine structure (EXAFS). We hope that this understanding will shed some light on the complicated dynamic properties, which is still an unsolved problem from theoretical treatment.

## 1.5 Crystallization of polymer

Polymer crystallization is a process in which polymer's gain partial alignment of their molecular chains, which is achieved by folding them together and creating ordered regions known as lamellae. The lamellae consist of large spheroidal structures known as *spherulites* (Keller, 1952 and Charles, 2003). Under certain conditions of the melting-cooled polymers, the size and structure of the crystals and the degree of crystallinity depend on the type and structure of the polymer and the growing conditions. Crystallinity can also affected by external factors such as crystallization temperature and cooling rate. The degree of crystallinity depends on tacticity of the polymer and the larger the order in the molecule, the more likely the molecule will crystallize. The case of strain-induced crystallization is affected by the molding process of the polymer film or fiber, the stretch ratio and the strain rate. For example, isotactic polypropylene (*i*PP) usually crystallize better than syndiotactic polypropylene (*s*PP). The atactic polypropylene (*a*PP) is considered uncrystallizable because polymer molecule lacks any regularity.

There are various methods to study polymer crystallization. For the calorimetry technique, the energy is released upon melting a semi-crystalline polymer and can be measured with differential scanning calorimetry (DSC) and compared with the standard sample with a known amount of crystallinity. For the X-ray diffraction method, regular arrangement of motifs create sharp diffraction peaks, where the amorphous regions result in broad halos. X-ray diffractograms of polymers usually contains both diffraction peaks and amorphous regions. Crystallinity can be determined by integrating the relative intensities of the peaks and halos. For the optical microscope technique, we can observe polymer morphology called spherulites, which have the size between 1 and 100 micrometers. These spherulites form the colored patterns called "*maltese cross*", caused by molecular alignment within the individual lamellae of a spherulite when observed using polarized optical microscope.

## 1.6 Monte Carlo simulation

Computer simulation of polymer materials is a quite challenge, because of the broad range of lengths and time scale of phenomena. Coarse-grained lattice models have been considered as an effective simulation for polymers. The vinyl polymer simulation on the second nearest neighbor diamond (2nnd) lattice remains sufficient detail to distinguish the detailed chemical composition of the polymer. It also allows for the equilibration of large polymer systems on reasonable time scales with atomistic simulation. These techniques have been used to study the effect of the stereochemistry of polymer chain on various properties (Mattice, 1999; Akten, 2001 and Clancy, 2001). In an effort to understand the structures, dynamics and crystallization, the method was demonstrated for simulation of structure formation in the case of monodisperse PE, polymer mixture composed of short and long PE chains and stereo-irregular and stereo-defect isotactic PP. We employed the coarse-grained model with specific stereochemical sequence through the use of an on lattice Monte Carlo (MC) simulation to detect how each specific sequence influences the dynamics of each chain of the polymer in the melt state through intra and intermolecular interactions. For crystallization, this MC simulations on coarse-grained models were conducted to consider the role of stereotacticity defects with an isotactic polypropylene chain on the formation of crystalline order within the chain. All systems are equilibrated above the melting temperature and are then cooled stepwise to lower temperatures to ensure each system is equilibrated at every temperature.

## 1.7 Molecular dynamic simulation and X-ray absorption spectroscopy

Typically, structural parameters in chemistry can be determined through theoretical techniques, such as *ab initio* electronic structure calculations or numerical simulations, such as Molecular Dynamics (MD) simulations (Owczarek, 2006 and Owczarek, 2007). The MD simulation technique is an efficient method, the strength that other methods cannot do, is to examine such processes in condensed phase environments and provide a detailed picture of the structure and dynamics for complex systems. The number of studies that combine MD simulations with X-ray absorbent structures (EXAFS) has increased significantly due to advances in modern algorithms and the availability of more accurate ions and solvent potential (D’Angelo, 1994; Filipponi, 1995; D’Angelo, 1996; Di Cicco, 1997; Roccatano, 1998; Hoffmann, 1999; D’Angelo, 2004; Witkowska, 2006; Dang, 2006 and Anspoks, 2011). The accuracy of theoretical models is available for inter-atomic potential in chemical systems have been discussed by comparing EXAFS and MD simulation results directly (D’Angelo, 2004 and Dang, 2006). Extended X-ray Absorption Fine Structure (EXAFS) have been used to examine the atomistic structure of polymer/salt complex. This is different from the XRD method that determines the yield of crystalline materials, while EXAFS can be applied to get structural information of non-crystalline materials (Teo, 1986 and Linford, 1995). EXAFS data can be used to get information about the nearest neighbor atoms around the probed species and the distance from the target element atoms to their neighbors. This approach avoids the need to compare poorly defined entities, such as coordination or solvation numbers by a direct comparison of experimental and simulated measured spectral quantities. The MD-EXAFS spectra results are correspond to the experimental measurements and the ion-oxygen distances for the first hydration shell, in that they agreed with the experiments within 0.05-0.1 Å.

In this work, differential scanning calorimeter (DSC), polarized optical microscopy (POM) and Small- and Wide-Angle X-ray Scattering/Diffraction (SAXS/WAXD) were employed to study polymer crystallization and morphological changes of commercial iPP and poly(propylene-co-1-butene) samples. Moreover, the MC simulation method with three systems of monodisperse PE, bi-disperse PE mixtures and stereo-irregular isotactic PP were performed to study polymer crystallization based on a more realistic polymer model. For the collaborative research with the Institute for Chemical Research, Kyoto University, EXAFS and MD simulation were used to define the atomistic solvation structure of neat PICOOH and cation-doped carboxylate polyisoprene systems (PICOOM). The main results used to characterize the aggregation are (1) the distance between oxygen atoms and hydrogen/cation and (2) the coordination number, which indicates the average amount of oxygen atoms around probed atom ion in the first solvation shell.

## 1.8 Research objectives

- To investigate the structures and dynamics of monodisperse PE, bi-disperse PE mixtures and stereo-irregular isotactic PP based on molecular simulation technique.
- To investigate the effect of short-chain branched (1-butene) on crystallization characteristics and phase morphology of isotactic polypropylene via thermal analysis and X-ray scattering.
- To study the solvation structure at the atomistic level and dynamic properties at the nanosecond time scale of end-carboxylated polyisoprene doped with mono- and bi-valence cation.

## 1.9 Scope and limitation

This research work is divided into 2 main parts:

### 1.9.1 Molecular simulation

The computational techniques in this section are as follows:

1.9.1.1 Monte Carlo (MC) simulation: to investigate the structures, dynamics and crystallization of monodisperse PE, bi-disperse PE mixtures and stereo-irregular isotactic PP of coarse-grained models.

1.9.1.2 Molecular dynamic (MD) simulation: to study the structural and dynamic properties of neat PICOOH and end-carboxylated polyisoprene (PI-COO$^-$) doped with Li$^+$, K$^+$ and Ca$^{2+}$.

### 1.9.2 Sample characterization

The chain structure, crystallization characteristics and phase morphology of *i*PP and *i*PP with 1-butene defects were investigated using various experimental techniques as follows:

1.9.2.1 Gel permeation chromatography (GPC): to verify number-, weight-averaged molecular weight (Mn, Mw) and polydispersity index (PDI) of all three PP samples.

1.9.2.2 Nuclear magnetic resonance (NMR) spectroscopy: to estimate the number of defect (stereo-irregular and 1-butene) in *i*PP with defects samples.

1.9.2.3 Differential scanning calorimeter (DSC): to determine the transition temperatures, degree of crystallinity and crystallization characteristics of PP samples.

1.9.2.4 Polarized optical microscopy (POM): to study the crystal morphology and crystallization characteristics in PP samples.

1.9.2.5 Small- and wide- angle X-ray scattering/diffraction (SAXS/WAXD): to investigate the polymer crystallization, phase morphology change, degree of crystallinity and crystallization kinetics of PP samples.

1.9.2.6 Extended X-ray absorption fine structure (EXAFS): to study the atomistic solvation structure including the coordination numbers and the distance of neighboring atoms from the probed cations in end-carboxylated polyisoprene (PI-$COO^-$) doped with $K^+$ and $Ca^{2+}$.

# CHAPTER II

# LITERATURE REVIEW

## 2.1 Homopolymer and copolymer of polypropylene

Isotactic polypropylene (*i*PP) was firstly developed by Natta *et al*. In addition to its mechanical performance, lightness, chemical resistance and transparency advantages, iPP has become a popular product in the global thermoplastic market. It has a wide range of applications such as containers, wrappers, medical and laboratory equipment (Utracki, 1998). The outstanding performance is strongly related to its semicrystalline structures controlled by its crystallization kinetics. To improve the properties of *i*PP, placing some comonomer units at random positions within the chain is one of the possible methods to modify material properties. This approach leads to decreased ranges of crystallization and melting temperatures, as well as crystallinity reduction (Flory, 1953; Balbontin, 1992 and Hauser, 1998). Many previous works have been performed to investigate the crystallization behavior of random copolymer based on poly(propylene) containing a small fraction of comonomers (Auriemma, 2002; Hosoda, 2002; Hosier, 2003; Gou, 2007; Rosa, 2007 and Jeon, 2009). One interesting success case is the commercial product from SINOPEC thermoplastic called the G-resin, which is *i*PP containing a few amounts of 1-butene. Up to now, there are few studies for direct comparison of the crystallization kinetics between G-resin and *i*PP. Such knowledge does not only help to better understand the chemical confinement on polymer crystallization but also it is helpful to design the processing of G-resins for better performances. Isothermal crystallization is one of the most common methods to study the effect of chain structures (*e.g.* tacticity and chain length) on the crystal structure formation. This method also can be used to gain the information of the crystallization kinetics.

Previously, Tang *et al.* (Tang, 2012) studied polypropylene random copolymers with few 1-butene (iPPBu) and ethylene (iPPEt) content. They reported differential scanning calorimetry (DSC) and *in-situ* small angle X-ray scattering (SAXS) studies of microstructure evolution of these random copolymers during the heating process. The signal of melting enthalpy of iPPBu disappears slightly faster than that of iPPEt, which retains steady decay of the scattering intensity during the end of melting process. For their SAXS data, Figure 2.1 shows the evolution of long spacing of iPPEt and iPPBu as a function of temperature. The long spacing ($d_{ac}$) for both samples increases slowly below 135°C and enhance rapidly due to the selective melting of thin crystalline lamellae, which may occur along with a thickening process of residual crystals. In addition, the crystalline thickness ($d_c$) was studied and their results are shown in Figure 2.2. The crystalline thickness increases as a function of temperature, similar trend to the long spacing. The crystalline layer of iPPBu is thicker than that of iPPEt at the temperature over 135°C. Thus, the crystals of iPPBu are more stable than that of iPPEt. These results suggest that the melting behaviors of such copolymers rely not only on the lamellar thickness but also on the crystal stability.

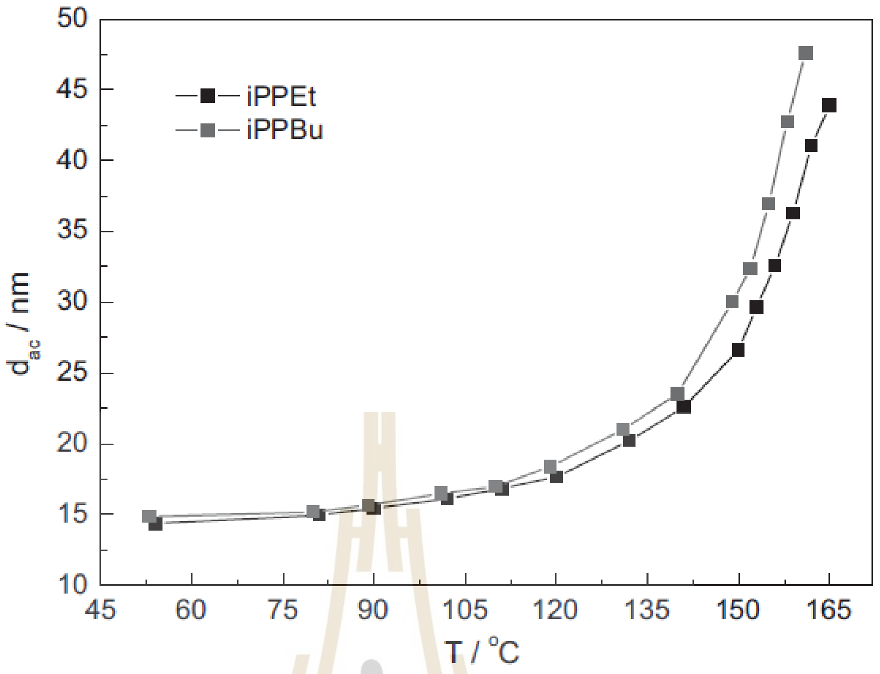

**Figure 2.1** Long period ($d_{ac}$) of iPPEt and iPPBu as a function of temperature (Tang, 2012).

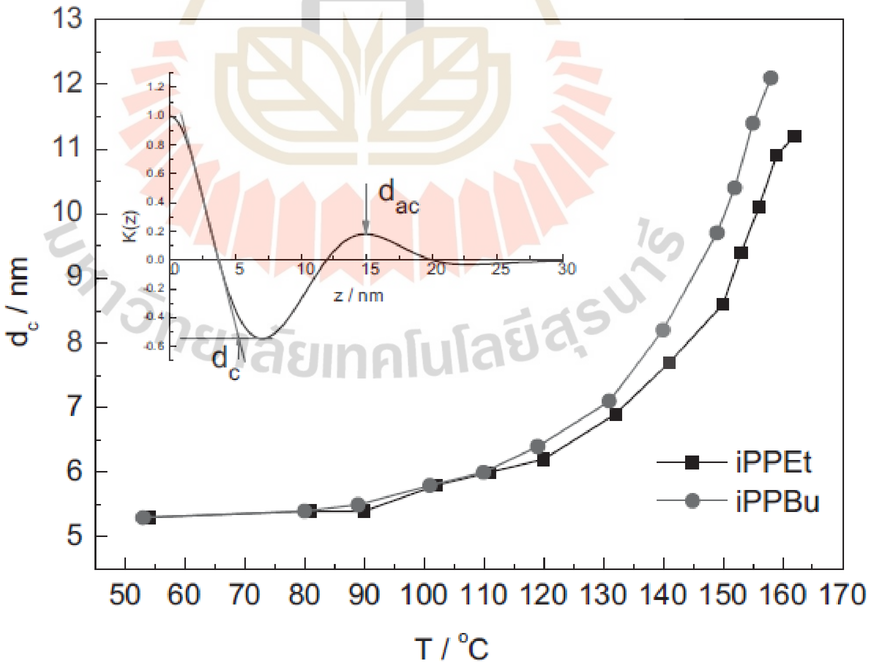

**Figure 2.2** Crystalline layers ($d_c$) for iPPEt and iPPBu during the heating process (Tang, 2012).

Recently, Kalapat *et al.* (Kalapat, 2017) applied the fast-scan chip-calorimeter Flash DSC to study and compare both non-isothermal and isothermal crystallization kinetics for two G-resin samples with few 1-butene defects *i.e.* MT12-s and MT18-s (the numbers stand for the melt flow rate (MFR) = 12 and 18 g/10 min at 230°C, respectively) and homopolymer isotactic polypropylene (V30G with MFR = 15-20 g/10 min). The temperature-dependent difference of the crystallization rate is related to the chemical confinement effect of comonomers. The half crystallization times for these three samples are presented in Figure 2.3. The samples with 1-butene defects crystallize slower than *i*PP. In comparison between these two G-resins, MT18-s crystallizes slightly faster than MT12-s at low temperatures possibly due to different molecular weights. MT18-s has lower molecular weight thus promoting faster molecular mobility at low-temperature.

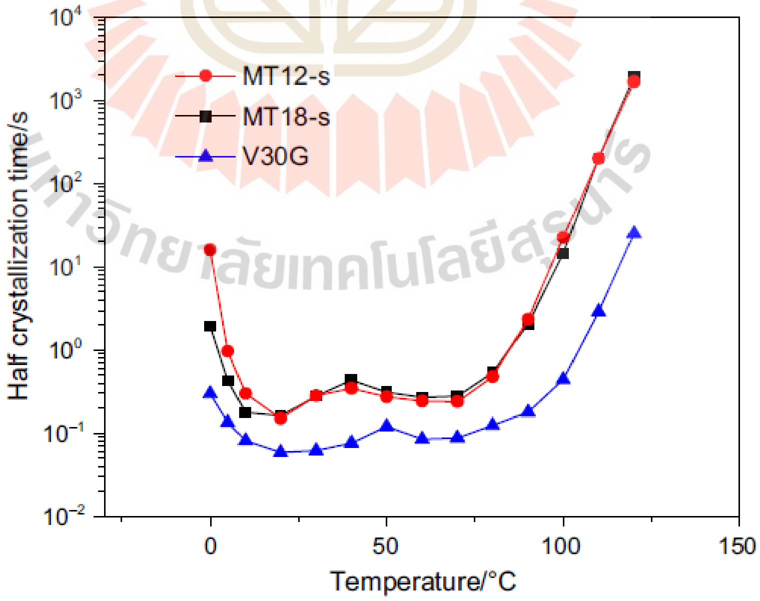

**Figure 2.3** Half crystallization times of MT12-s, MT18-s (G-resin) and V30G (pure iPP) as a function of the isothermal crystallization temperature (Kalapat, 2017).

## 2.2 Monte Carlo (MC) simulation

Crystallization of long chain molecules is an interesting and challenging topic in polymer science. There are many factors that can affect crystallization such as type and structure of polymer, crystallization temperature, cooling rate and polydispersity. In this thesis, we are interested in the effect of polydispersity, which is used to describe the degree of non-uniformity of a distribution of the polymer, on the degree of crystallinity. There have been many experimental results and theoretical developments in the concept of chain folding proposed in polymer science several decades ago (Keller, 1957 and Wunderich, 1976). In particular, those studies are based on static light scattering, microscopy, and differential scanning calorimetry use to characterize the crystal morphology obtained during the crystallization of polyethylene (PE) which is largely dependent on molecular weight and polydispersity (Mandelkern, 1968; Maxfield, 1977 and Voigt-Martin, 1980). Although many experimental studies have been proceeded on polymer crystallization and nucleus formation, as highlighted by recent reviews (Schick, 2017; Cui, 2018 and Yue, 2018), it remains challenging for experiments to achieve the nanoscale temporal and spatial resolutions necessary to track the molecular-level evolution of nuclei. Hence, the detailed mechanism of structure formation on the molecular level is not fully understood. In order to expose the formation of structures at the molecular level, especially in the early stages, some works on molecular simulation were needed to perform for polymer crystallization.

Local structures at an early and relatively late stages can be derived from molecular dynamic (MD) simulations and it was found that the global order parameter only increased after the chains were stretched to some extent (Sadler, 1986; Takeuchi, 1998 and Fujiwara, 1999). The folding of the long PE chain from solution was also studied through MD (Martonák, 1996 and Yamamoto, 1997) and MC simulation (Chen, 1998). However, less work has investigated the construction of molecular structures from a dense polymer system. Hu (Hu, 2000) simulated the structure and melting point of the polymer chain on a simple cubic lattice through collinear energy and parallel energy between two Kuhn sections. To investigate polymer crystallization based on more realistic polymer model and to reduce computational time compared with fully atomistic MD, MC simulation was performed for coarse-grained PE chains on a high coordination lattice (Xu, 2001). This approach avoided introducing artificial energies, such as collinear energy and parallel energy, which were involved inevitably in other coarse-grained lattice MC simulations. The method was demonstrated for simulation of structure formation in the case of monodisperse PE. In this thesis, the same simulation method will be extended to investigate the crystallization of polymer mixture composed of short and long PE chains.

## 2.3 PICOOH and PICOO$^-$ doped with cations

Polyisoprene (PI) chains with high cis unit content have the so-called type-A dipole parallel along the chain backbone for their global motion results in slow dielectric relaxation. (Boese, 1990; Adachi, 1993; Watanabe, 2001 and Watanabe, 2009). In general, the dielectric relaxation reflects an orientational memory of the end-to-end vector $\boldsymbol{R}$ at times $t$ and $0$, $\langle \mathbf{R}(t)\cdot\mathbf{R}(0)\rangle_{eq}$, which directly related to the cross-correlation between different sub-molecules (Watanabe, 2001 and Watanabe, 2009). On the other hand, the viscoelastic relaxation reflects the orientational anisotropy of the sub-molecules that are not directly detecting the cross-correlation. As an experiment for monodisperse PI with various topological structures, differences in normalized dielectric and viscoelastic relaxation were observed in linear response regimes, $\Phi(t)$ and $\mu(t)$, which results from this difference (Watanabe, 2001; Watanabe, 2002; Watanabe, 2004; Watanabe, 2008; Watanabe, 2009, Watanabe, 2011 and Watanabe, 2012).

Interesting polymer dynamics have been studied for the case of viscoelastic relaxation of polyisoprene undergoing monofunctional head-to-head association and dissociation. When the reaction rate is much slower than the movement of large-scale intrinsic chain, the dynamics of those polymer chains are limited by competition between the association/dissociation reaction kinetics and internal chain movement (motion in the absence of reaction), resulting in the terminal relaxation of the chain is greatly reduced. On this occasion, the fast relaxation of the chain is an internal movement between the associated sites, while the slow terminal relaxation appears through the large-scale movement triggered by the dissociation reaction. On the other hand, the situation becomes more complex with the reaction faster than the intrinsic chain movement, as the reaction strongly matches the movement of associated and dissociated chains. Previously, Watanabe *et al.* (Watanabe, 2015) has simulated the simplest model system without the effect of entanglement and Rouse chains undergoing the monofunctional association and dissociation at the chain ends for theoretical analysis of viscoelastic relaxation. They used the normalized relaxation moduli of unimer and dimer, $g_1(t)$ and $g_2(t)$ to show that limits in fast reaction both $g_1(t)$ and $g_2(t)$ correspond to the relaxation function within Rouse relaxation function of the unimer, $g_{1,R}(t)$. From this above studies, it could be considered that the dynamics of the unimer is not affected by the fast reaction, and that all the dimmer are converted to unimers through rapid dissociation. For other fast reactions, such as the unimer (and dimer) of Intrinsic Rouse mode and the new relaxation modes not inferred from the intrinsic Rouse dynamics, it is separated from the motional coupling. The possibility of retrieving information for chemical reactions from the viscoelastic data of the nonentangled unimer/dimer system was discovered by combining all these effects and leading to the coincidence of $g_1(t)$ and $g_2(t)$ with $g_{1,R}(t)$ in the fast reaction limit.

Recently, Matsumiya *et al.* (Matsumiya, 2016) performed an experimental test this theoretical calculation and observe the feature of the chemical reaction. At first, they synthesized two reference samples, the same molecular weight of neat PI without the carboxyl group and $PI_2$ dimer undergoing no dissociation. Then they synthesized polyisoprene (PI) sample having an associative carboxyl group at one end (PI-COOH). All samples were eliminated the entanglement effect through dilution in oligomeric butadiene. The diluted PI-COOH and the reference samples were used to compare the viscoelastic behavior. The results found that the dynamics of associating/dissociating PI-COOH were based on theoretical calculations and the polymeric character of the PI-COOH chain greatly affects viscoelastically detected association/dissociation.

# CHAPTER III

# RESHEARCH METHODOLOGY

## 3.1 Experimental part

### 3.1.1 Apparatus and materials

- Liquid nitrogen
- Cover slip
- Circular round microscope slide
- Netzsch Aluminum sample pans
- Netzsch 214 Polyma Differential Scanning Calorimetry (DSC)
- Nikon Eclipse Ci-POL Polarizing Microscopes
- Linkam THMS600 hot stage
- Compression molding presses
- Synchrotron Small- and Wide Angle X-ray Scattering/Diffraction (SAXS/WAXD)
- Synchrotron Extended X-ray Absorption Fine Structure (EXAFS)
- Bruker AV600 Nuclear Magnetic Resonance Spectrometer (NMR)
- *Isotactic* Polypropylene, Beijing Research Institute of Chemistry
- G-resins Polypropylene, Beijing Research Institute of Chemistry
- Hydrochloric acid (HCl)
- Tetrahydrofuran ($(CH_2)_3CH_2O$)
- Calcium dihydroxide ($Ca(OH)_2$)

- Potassium hydroxide (KOH)
- 1,2-dichlorobenzene-d4 ($C_6D_4Cl_2$)
- 1,2,4-trichlorobenzene ($C_6H_3Cl_3$)
- Methanol ($CH_3OH$)

### 3.1.2 Polypropylene and poly(propylene-co-1-butene)

Polymer samples are from the Beijing Research Institute of Chemistry and Industry, SINOPEC, China. Two G-resin samples are MT12-s and MT18-s mainly different in the melt flow index. One homopolymer of isotactic PP (V30G) is used for comparative purpose. The melt flow rates (MFR) measured at 230°C/2.16 kg) are 13.28 g/10 min, 19.68 g/10 and 23.30 g/10 min for MT12-s, MT18-s and V30G, respectively. Molecular weight and 1-butene content are determined by gel permeation chromatography (GPC) and nuclear magnetic resonance (NMR) spectroscopy, respectively.

### 3.1.3 Cation-doped end-carboxylate salt polyisoprene (PICOO$^-$)

For starting materials, $PI_{30}COOLi$ and PICOOH are prepared using anionic polymerization by Matsumiya et al. (Matsumiya, 2016), with the following steps. High-cis linear polyisoprene (PI) with the carboxylated ion at the chain end is synthesized using anionic polymerization and functionalized the head group by $CO_2$. The initiator and solvent are sec-Butyllithium and benzene (Bz). To convert isoprenyl anion into a less reactive DPE anion in an initial state, PI-anionic polymer was reacted with diphenylethylene (DPE) in the tetrahydrofuran (THF)/benzene mixture. After that, PI-DPE-anion is reacted with $CO_2$ to convert the head group to COOLi. The product obtained in the form of PI-DPE-COOLi. This sample is dissolved in THF and reacted with HCl to transform the COOLi group to COOH. In this work, $PI_{30}COOH$ is converted to $PI_{30}COOM$ by reacting with equimolar $Ca(OH)_2$ or KOH in THF for $(PI_{30}COO)_2Ca$ and $PI_{30}COOK$, respectively. Then, samples are placed under vacuum to remove THF and $H_2O$ from the samples. These samples are characterized by X-ray absorption fine structure (EXAFS) spectroscopy to determine the solvation structures at atomistic level *i.e.* surrounding atoms, the coordination number and the distance neighboring atoms.

### 3.1.4 Sample characterization

#### 3.1.4.1 Gel permeation chromatography (GPC)

GPC was employed to determine molecular weight and molecular weight distribution of all polymers by Polymer Char GPC-IR5. First, the polymer sample of 4.00 mg was dissolved in 1,2,4-trichlorobenzene at 160°C. The column was calibrated using fractions of the known molecular weight standard (usually polystyrene sample with narrow molecular weight distributions) (Darsey, 1981).

#### 3.1.4.2 Nuclear magnetic resonance (NMR) spectroscopy

The content of 1-butene defect was determined using $^{13}C$-NMR. The sample solution was prepared by dissolving the samples (~10 wt%) in 1,2-dichlorobenzene-$d_4$/1,2,4-trichlorobenzene (2:3 v/v). The measurements were conducted at Kyoto Institute of Technology using AV600 NMR spectrometer (Bruker, Germany) at 120°C with the number of scans set to 2048.

#### 3.1.4.3 Polarized optical microscopy (POM)

The crystal morphology of polymer samples was investigated using Nikon Eclipse Ci-POL Polarizing Microscopes with Linkam THM600 hot state (Linkam Scientific, UK). The sample was cut into a small piece and sandwiched between two cover slips. Next, samples were heat from the room temperature to 200°C, isothermally maintained at 200°C for 5 min, and then quickly cooled with a cooling rate 150°C/min to isothermal crystallization temperature at 135°C and kept isothermally until the completion of crystallization process. All images were taken under cross polarizers with a 530 nm optical retardation plate.

#### 3.1.4.4 Differential scanning calorimeter (DSC)

DSC was used to determine the melting temperature ($T_m$), crystallization temperature ($T_c$), percent of crystallinity and the crystallization kinetics of polymer samples. About 6-8 mg of sample was sealed with aluminum pan. Both isothermal and non-isothermal crystallization kinetics of PP samples were investigated. DSC measurements for non-isothermal crystallization were performed using NETZSCH DSC204 F1 Phoenix for V30G and MT18-s at IRPC company and Perkin Elmer PYRIS Diamond DSC for MT12-s at Suranaree University of Technology. Both DSCs were calibrated with indium standard. First, the samples were heated from 50°C to 200°C, hold at 200°C for 5 min to erase thermal history and then cooled to 50°C at various cooling rates 5, 10, 15, 20, 25 and 30 °C/min.

DSC measurements for isothermal crystallization were performed at Kyoto Institute of Technology using DSC214, *polyma* (NETZSCH, Germany) with a liquid nitrogen cooling system. The instrument calibration is calibrated with an Indium standard for temperature and heat flow. First, the sample was melted at 200°C for 5 min to completely erase the previous thermal history of the material and cooled rapidly with a cooling rate of 300°C/min to given isothermal crystallization temperature (125.0, 127.5, 130.0, 132.5 and 135°C). DSC measurements were continued until the crystallization was complete and the sample was heated again to 200°C with a heating rate of 10°C / min to measure the melting temperature of the crystalline polymer formed in the sample. All the experiments were done under nitrogen atmosphere.

### 3.1.4.5 Small- and wide- angle X-ray scattering/diffraction (SAXS/WAXD)

Synchrotron X-ray source was used to measure the time-resolved SAXS/WAXD. The measurements were performed by beamline BL15-A2 at the KEK (High-Energy Accelerator Research Organization) in Tsukuba, Japan. The measurements were done for the sample during isothermal crystallization (130°C) with an exposure time of 5 seconds using vacuum-compatible PILATUS3 2M for SAXS and PILATUS3 300KW for WAXD as a two-dimensional detector. The wavelength of the incident X-ray beam was 0.1204 nm. The samples were loaded into an aluminum cell with a diameter of 4 mm and a thickness of 1 mm and sandwiched with a couple of pieces of polyimide (Kapton) film, which is a brand of DuPont-Toray Co., Ltd., Tokyo, Japan. First, the samples were melted at 200°C for 5 mins, and then the sample cell was rapidly transferred to the other heater block, which maintained at 130°C and then time-resolved measurements of SAXS/WAXD were performed. The 1D SAXS and WAXD profiles were obtained after subtracted the background scattering and taking the circular average of the 2D-SAXS pattern and the sector average of the 2D-WAXD pattern, respectively.

The scattering profile will be corrected for beam intensity, sample transmission, background scattering and converted to Lorentz corrected SAXS profile by multiplying by $q^2$ (Vonk, 1967). The scattering vectors is defined as (Glatter, 1982):

$$q = (4\pi/\lambda)\sin\theta \tag{3.1}$$

where λ is the wavelength of the X-ray source and 2θ is the scattering angle. The scattering angle is given by:

$$2\theta = \tan^{-1}(D/L) \tag{3.2}$$

where $D$ is the distance from the origin to the point on the detector plane which is determined by the pixel size and $L$ is the sample-to-detector distance. Differences in electron density of the crystalline and amorphous domain affect the total scattering intensity proportion. The change in this scattering intensity is the volumetric fraction of the crystalline phase in a semi-crystalline polymer, in which the crystalline change is observed (Koberstein, 1983; Verma, 1996; Ivanov, 1999; Luo, 2001; Ivanov, 2001 and Lee, 2004). The morphological parameters such as the long period ($L_p$) and the average lamellar thickness ($L_c$) of all samples will be determined using the paracrystalline method. In addition, the long period can also be estimated from the first maximum at the lowest scattering angle by applying Bragg's law in the SAXS profiles. The Bragg's law is given by:

$$L_B = \frac{2\pi}{q_{max}} \tag{3.3}$$

where $q_{max}$ is the scattering vector at maximum intensity. The method to determine the long period ($L_p$) and the average lamellar thickness ($L_c$), and other structural parameters of the stacked lamellae is to estimate from the 1D-electron density correlation function, $K_{(z)}$. Under the assumption of the two-phase model consisting of the alternatively stacked crystalline and amorphous layers. The $K_{(z)}$ can be expressed by (Strobl, 1980):

$$K_{(z)} = \left< \left[\eta_{(z')} - \left< \eta \right>\right] \left[\eta_{(z+z')} - \left< \eta \right>\right] \right> = 2\int_0^\infty \pi^{-1}\, q^2 I_{(q)} \cos(qz)\, dq \quad (3.4)$$

where < > is designated as the ensemble average, $\eta(z)$ and $< \eta >$ are the electron densities along the lamella normal and the averaged electron density, respectively (Rungswang, 2015 and Rungswang, 2017).

For WAXS profiles, the time evolution of the degree of crystallinity will be calculated using the following equation (Pandey, 2019):

$$\emptyset_{\mathrm{WAXS}} = \frac{\sum \mathrm{A_c}}{\sum \mathrm{A_C} + \mathrm{A_a}} \quad (3.5)$$

where $\sum \mathrm{A_c}$ and $\mathrm{A_a}$ are the summation of the peak area of the crystalline peaks and the amorphous halo, respectively.

#### 3.1.4.6 Extended X-ray absorption fine structure (EXAFS)

EXAFS is a measurement which corresponds to the oscillating part in the absorption coefficient (μ), starting at energies 50 eV and extending to 1000 eV above an absorption edge. When the energy is sufficient to induce the photoelectric ejection, in this case, we are interested in the ejection of the electrons from the K-edge, which is related by the 1s electron causing the absorption edge. Since the outgoing photoelectron is scattered through nearby atoms, it causes oscillation to occur and also leads to interferes between the outgoing and backscattered waves. Qualitatively, the shape and moment of oscillation are a function of the absorbing atom, as well as the distance, type, and the number of atoms around themselves. In general, the distance between the probed atom and the backscattering atoms should be around 5 Å for significant interference.

Stern, Sayers and Lytle, 1975 were originally developed the simplest correct theoretical explanation that call single-electron single-scattering theory. This theory presumes that multiple-scattering is not important. In addition, both thermal and static disorders are small. It assuming a completely isotropic sample which and following this equation.

$$\chi(k) = \frac{\mu(E)-\mu_0(E)}{\mu_0(E)} = \sum_j N_j S_0^2(k) \frac{F_j(k)}{kR_j^2} e^{-2\sigma_j^2 k^2} e^{-2R_j/\lambda_j} \sin[2kR_j + \phi_{ij}(k)] \quad (3.6)$$

where $\mu(E)$ and $\mu_0(E)$ are the measured and average absorption coefficients, respectively, at the energy $E$, $N_j$ is the number of atoms in the $j$th shell, $S_0^2(k)$ is the amplitude of the reduction factor caused by the electron excitation beyond K-edge, $F_j(k)$ is the backscattering amplitude from the $N_j$ atom, $R_j$ is the root mean square distance between the probed and the $j$th atom, $\sigma_j$ is the Debye-Waller factor, $\lambda_j$ is the electron mean free path, and $\phi_{ij}$ is photoelectron phase shift. In Eq. (3.6) it is assumed that $R_j$ and the type of all atoms are identical in the $j$th shell. If the sample or polarization of the electric field is isotropic, a sum greater than l can be achieved to get $N_j$. k is the wave vector. With an energy balance can show that

$$k = [\frac{2m_e}{h^2}(E - E_0)]^{\frac{1}{2}} \quad (3.7)$$

where $E_0$ is the absorption edge energy, $m_e$ is the electro mass, and $h$ is Planck's constant divided by 2π. Eq. (3.6) provides the equation for EXAFS oscillation as a function of the wave vector. The Fourier transform is generally performed to obtain the radial structure function (RSF), which has unit in angstroms. RSF is associated with the radial distribution function at its peak in the RSF corresponds to distinct coordination shells, but the peaks are shifted from the interatomic distances as shown in the above equation.

The solvation structure at atomistic scale of the carboxylated poly(cis-1,4-isoprene), $PICOO^-$, neutralized with $K^+$ and $Ca^{2+}$ can be studied by X-ray absorption spectroscopy. The experimental potassium and calcium K-edge EXAFS spectra were evaluated at BL-8 beamline, Synchrotron Light Research Institute (Nakhon Ratchasima, Thailand). The Siam Photon Source storage ring was operated at 1.2 GeV with an electron beam current of 80-150 mA. The EXAFS spectra of standard (HCOOK and $(CH_3COO)_2Ca$) and samples were collected in transmission and fluorescent yield mode (13-elements Ge detector) using Si(111) and Ge(220) double crystal monochromator for $K^+$ and $Ca^{2+}$ K-edge, respectively. For all samples, 10 eV steps were used in the pre-edge area, whereas 0.5 eV steps were performed from 20 eV below the edge to 30 eV above the edge, and 0.05k eV steps were used in the EXAFS area. Standard KI and $CaCO_3$ powders were used for energy calibration. A total of 13-14 scans were averaged after $E_0$ determination to improve the signal-to-noise ratio and to reduce the random error from the measurement. The data processing can be done using ATHENA and FEFF7.0 software solutions to calculate the phase shift and backscattering amplitudes. The EXAFS data can be further converted using Fourier transformed over the ranges $2.0 < k < 8.2$ with $k^2$ weighting. The experimental data were fit compared with $(CH_3COO)_2Ca$ and HCOOK for $(PI_{30}COO)_2Ca$ and $PI_{30}COOK$, respectively, and then fitted using the selected atomic coordinates generated from molecular dynamic simulation. In this work, the proposed method for simulated EXAFS spectra is different from the typical technique from other experimentalists who generally employ the initial guess structure based on the atomic coordinates from the known crystal with similar structure.

## 3.2 Computational Part

### 3.2.1 Monte Carlo (MC) simulation

MC method is a randomized technique to equilibrate the system that bases on the principle of probability, which technique collects samples in a random way and use random numbers to make a decision during the course of changing the states. In this method, the coarse-grained model is used by reduce the fully atomistic model and the united atom model, as shown in Figure 3.1. The C-C-C bond angle is approximately tetrahedral and the three rotational isomeric state are separated by torsion angles (*trans* and *gauche*) of 120°. Hence, the most natural lattice for polymer simulation should be the diamond lattice. Due to this coarse-grained nature, the new lattice take only every second cite called “the second nearest neighbor diamond” (*2nnd*) lattice (Rapold, 1995). Monte Carlo (MC) simulations of structural formation during the initial stage of crystallization process of monodisperse and bimodal mixture of short polyethylene (PE) (C40 + C20) chains at low temperature were carried out by coarse-grained model mapped on *2nnd* lattice.

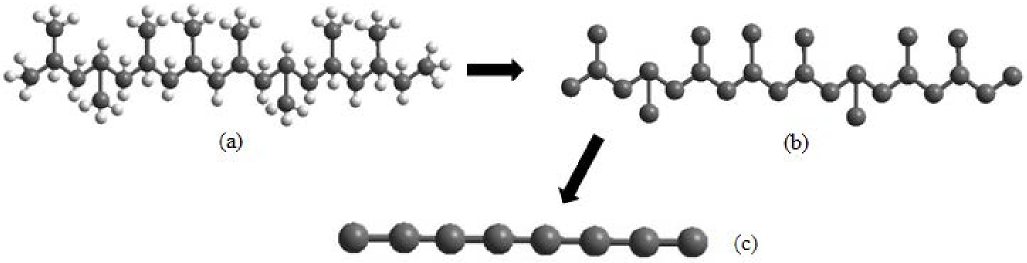

**Figure 3.1** Schematic models of polymer chains. (a) fully atomistic, (b) united atom and (c) coarse-grained model.

Every PE repeating unit was represented with one bead in the lattice and two real C-C bonds were shown through one *2nnd* bond This *2nnd* lattice can be produced by removing all other lattice sites from diamond lattice and creating a highly coordinated lattice with 10i2 + 2 site for the ith shell. There are four possible values for the distance between i and i + 2 beads, which are formed by *tt*, *tg* , $g^+g^+$ and $g^+g^-$ states, which two C–C bonds connected to bead i+1. The relation between the chain conformation and the distance of every other bead in the lattice is shown in Figure 3.2 and Table 3.1. Two parts of interaction are introduced in the simulation. One is the short-range interactions derived from the local intramolecular contribution of chain conformation based on the Rotational Isomeric State (RIS) model (Rapold, 1996). The other is long-range interactions based on the Lennard-Jones (LJ) potential (Cho, 1997) consisting the intermolecular and long-range intramolecular interaction. The RIS model for PE is represented by the statistical weight parameter (Abe, 1966) as $E_\sigma = 2.1$ and $E_\omega = 8.4$ kJ/mol, respectively. Here, $\sigma = \exp(-E_\sigma/RT)$ and $\omega = \exp(-E_\omega/RT)$. The long-range interaction is gained by modification the second virial coefficient of a non-ideal ethane gas using the Mayer *f* function with the LJ parameters of $\varepsilon/k = 205$ K and $\sigma = 4.4$ Å (Hirschfelder, 1954).

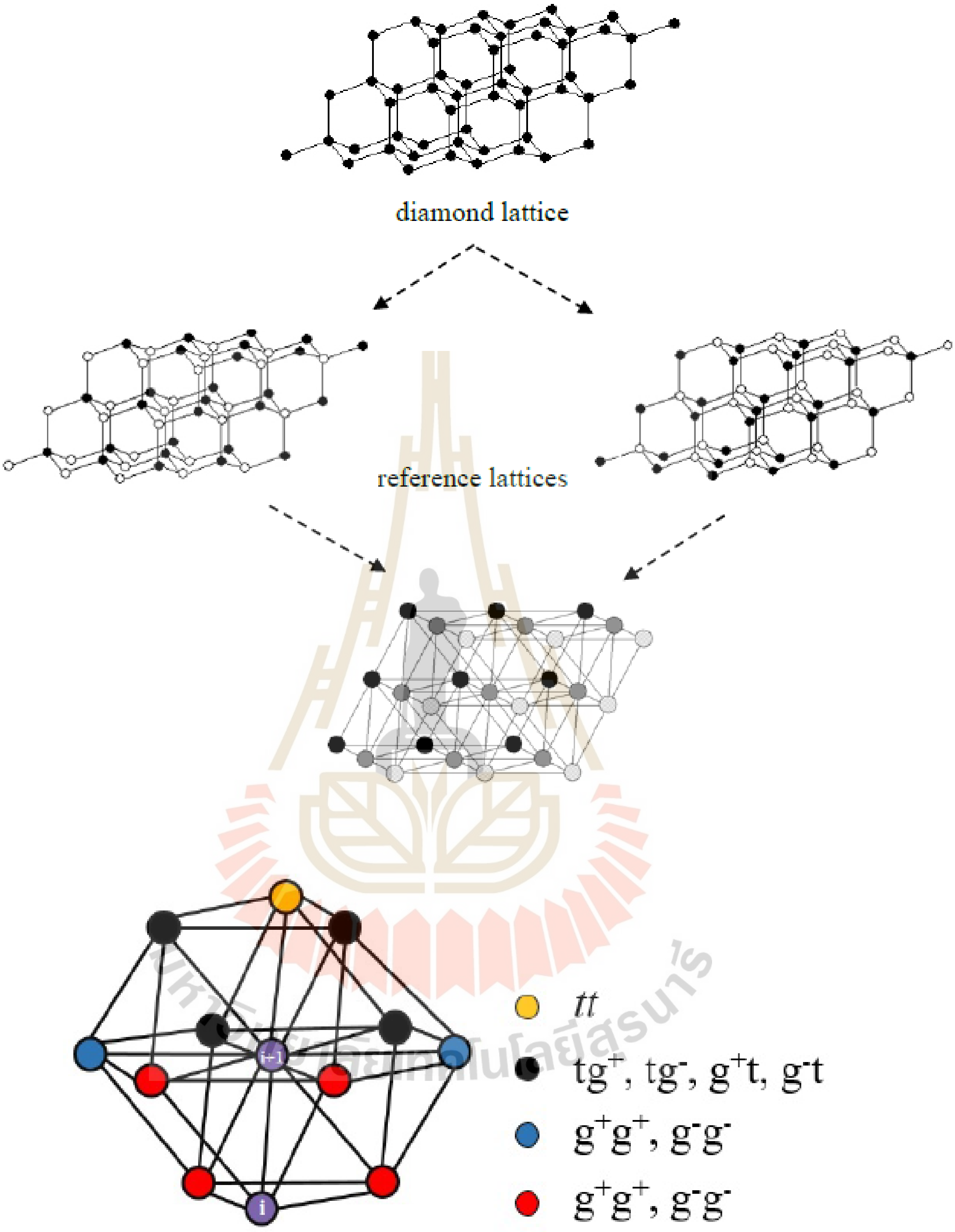

**Figure 3.2** Twelve nearest neighbors and chain conformation.

**Table 3.1** Relation of real sub chain conformations and the distances between every other bead on 2nnd lattice.

| Type | Length (nm) | Conformation |
|---|---|---|
| A | 0.500 | tt |
| B | 0.433 | $tg^+$, $tg^-$, $g^+t$, $g^-t$ |
| C | 0.353 | $g^+g^+$, $g^-g^-$ |
| D | 0.250 | $g^+g^-$, $g^-g^+$ |

The first three shells of this interaction are $E_{1st}$ = 8.165, $E_{2nd}$ = -0.348, $E_{3nd}$ = -0.608 kJ $mol^{-1}$ at 298 K, respectively. The first shell has a strong repulsive interaction whereas the second and third shell energies are attractive at low temperatures. All other shells have slightly attractive energy that have small effect in the present simulation.

Therefore, the following simulations only use the first three long-range interactions. In order to increase the speed of the simulation, both single and pivot moves are applied during the simulation (Clancy, 2000 and Xu, 2000). In a pivot move, the creation of a new structure for bond vector for short chain segments are generated from the reverse of the old conformation. At each Monte Carlo step (MCS), single bead and multiple bead pivot moves are tried randomly. The Metropolis rule (Metropolis, 1953) is applied to define the movement that cause double occupation and collapses (Doruker, 1997) and applied accept the move.

$$P = \begin{cases} \exp\left(-\frac{\Delta E}{RT}\right), & \Delta E>0 \\ 1 & \Delta E\leq 0 \end{cases} \tag{3.8}$$

where $\Delta E$ is the energy difference between the new and old conformation. R and T are the gas constant and absolute temperature. The move will be accepted when $\Delta E \leq 0$ or else generate random numbers to determine the move is successful or not.

In this thesis, the simulations were performed with three systems in comparison *i.e.* monodisperse PE, bi-disperse PE mixtures and isotactic PP with stereo-irregular defects. The box dimension has 16 steps (equivalent to 16 x 2.5 = 40 Å) and the periodic boundary conditions are applied. The monodisperse polyethylene (PE) system contains 46 chains (C) of 20 bead (B) ($C_{40}H_{82}$). Bead occupancy is 0.2246 which is equivalent to a density of 0.95 g/cm$^3$. In the simulation of PE mixtures, the set of C46B10 + C23B20 (LS50) and C10B10 + C41B20 (LS10) are represented by the weight fractions of the short chains of 0.50 and 0.11 in the mixtures, respectively. All polymer chains are placed into a periodic box with the density closed to that of the semi-crystalline PE. After equilibration of the melt at 473 K, the equilibrated structure was then step-wise cooling from 473 K to 298 K. The system is relaxed for 5 million MCSs at high temperature, 473 K. Then the system is cooled down to 400 K, followed by 350 K, with 5 million MCSs and the simulation ends at 298 K. For simulation of PE and PP crystallization, 5 and 20 million MCS were used in simulation at 298K, respectively.

### 3.2.2 Molecular dynamics (MD) simulation

In general, the atomic motion in a chemical system can be described by solving the Newtonian equation of motion used for MD simulation.

$$\vec{F_i} = m_i \vec{a_i} \tag{3.9}$$

For each atom $i$, $m_i$ is the respective atomic mass, $a_i = d^2r_i/dr^2$ is the acceleration and $F_i$ is the force acting upon the atom $i$. The forces can be determined from the gradient of potential energy $E$:

$$\frac{-dE}{d\vec{r_i}} = \vec{F_i} = m_i \frac{d^2\vec{r_i}}{dt^2} \tag{3.10}$$

The calculations of sequentially the locations and velocities in all particle systems were solved with Newton's equations. This creates a sequence of snapshots into a movie that consists of a simulated system and the atomic scale.

In order to solve Eq. (3.10), methods of numerical integration such as Gear, Verlet, leapfrog, and velocity Verlet have been developed (Sequeira, 2010). For the Verlet algorithm, it depends on the particle position at time $t$, $r(t)$, the acceleration at time $t$, $a(t)$, and the position from previous time $r(t-\Delta t)$. The new position of a particle after time $\Delta t$ is given by

$$r(t+\Delta t) = 2r(t) - r(t-\Delta t) + \Delta t^2 a(t) \tag{3.11}$$

The velocity at time $t$ can be calculated by

$$v(t) = \frac{r(t+\Delta t) - r(t-\Delta t)}{2\Delta t} \tag{3.12}$$

Verlet's algorithm does not use apparent velocities. The advantages of this algorithm are straightforward and the memory storage is simple, while the disadvantage is that the algorithms are moderately accurate. Another example is the leapfrog algorithm that the velocities leap over the positions, then the positions leap over the velocities. The leapfrog algorithm works in stepwise manner by first the acceleration at time *t* is calculated according to Eq. (3.16). Then, the velocity at a time is updated using:

$$v\left(t+\frac{\Delta t}{2}\right)=v\left(t-\frac{\Delta t}{2}\right)+a(t)\Delta t \tag{3.13}$$

After that, the atom position in the snapshot can be determined using

$$r(t+\Delta t)=r(t)+v(t+\Delta t/2)\Delta t \tag{3.14}$$

The advantage of this algorithm is that the velocities are explicitly calculated, but the main disadvantage is that the velocities cannot be calculated along with the position at the same time. To resolve this problem, the Verlet velocity algorithm was developed to provide positions, velocities and accelerations at the same time. This algorithm can be summarized as:

$$r(t+\Delta t)=r(t)+\Delta t v(t)+\frac{\Delta t^2 a(t)}{2} \tag{3.15}$$

$$a(t+\Delta t)=\frac{f(t+\Delta t)}{m} \tag{3.16}$$

$$v(t+\Delta t)=v(t)+\frac{1}{2}\Delta t[a(t)+a(t+\Delta t)] \tag{3.17}$$

Hence, MD simulation is the force field-based calculation technique to find the path of atomic/molecular motion based on the Newtonian equation of motion. The energy functions and parameter sets can be either obtained from quantum chemical calculations or parameterized with experimental data. For calculation of bond stretching and bending modes, it takes very long computational time because of large force constants. In general, these two terms are fixed. Therefore, the forces field to describe the potential energy depend on the remaining energetic terms which can be expressed as the bonded energy and non-bonded energy as:

$$E = E_{covalent} + E_{non-bond} \tag{3.18}$$

where

$$E_{covalent} = E_{bond} + E_{angle} + E_{torsion}$$

$$E_{non-bond} = E_{electrostatic} + E_{van\ der\ waals}$$

In this thesis, MD simulation of PICOO$^-$ neutralized with Ca$^{2+}$ and K$^+$ were performed using Gromacs 2018.1 with OPLS-AA (All-Atom Optimized Potential for Liquid Simulations) force field. The optimized structure and force field of end-carboxylated (COOH) and carboxylate salt (COO$^-$) *cis*-1,4-polyisoprene, PI were generated using LigParGen (Jorgensen, 2005; Dodda, 2017 and Dodda, 2017) and PolyParGen (Yabe, 2019) web server. PI with 10 repeating units were used. For cation-doped end-carboxylate PI, the minus charge was neutralized by adding the counter cation ion. Simulation model for each system can be created by placing a single relaxed molecule in the center of a cubic box, initially about 8 nm per side, and then 49 relaxed molecules were filled into the remaining spaces randomly in the box. Then, 25 Ca$^{2+}$ or 50 K$^+$ were added to neutralize each system. The polymer/salt mixtures were first done for energy minimization (EM) using the steepest descent algorithm in order to remove the undesired overlapping between neighboring atoms. After that, the systems were compressed at 298 K at artificially high pressure at 50 bar by NPT-MD run for 10 ns to eliminate any voids in the structures. Next, the NPT-MD equilibration run was carried out at 1 bar and 298 K. The systems were then equilibrated until potential energy and density became constant. After this step, long NVT-MD production run for 100 ns was performed at 1 bar and 298 K for subsequent data analysis.

The equations of motion in MD simulation were governed by the leap-frog algorithm (Freund, 2004) with a time step of 2 fs. The temperature was fixed at 298 K using Nose´-Hoover thermostat (Hockney, 1974 and Nosé, 2002) with a relaxation time of 2 ps. To maintain a constant pressure, the Berendsen Barostat with semi-isotropic coupling were used with the time and compressibility of 1 ps and $4.5 \times 10^{-5}$ bar$^{-1}$, respectively. The electrostatic interactions were calculate based on the Fast Particle Mesh Ewald (PME) method (Essmann, 1995) and fourth-order (cubic) interpolation was used with a real-space cutoff of 1.2 nm. For all simulations, periodic boundary conditions were applied and neighbor lists were updated every 10 time steps using a list cutoff radius of 1.0 nm. Linear Constraint Solver (LINCS) algorithm (Hess, 1997) with a lincs-order of 4 (number of matrices in the matrix inversion) were solved for the bond constraint. After the simulation was finished, various structural and dynamic properties were analyzed including radial distribution functions (RDF), mean square displacement (MSD) and rotational correlation functions (RCF). In summary, the flow chart of a typical GROMACS MD run of a molecule in a periodic box can be presented as following:

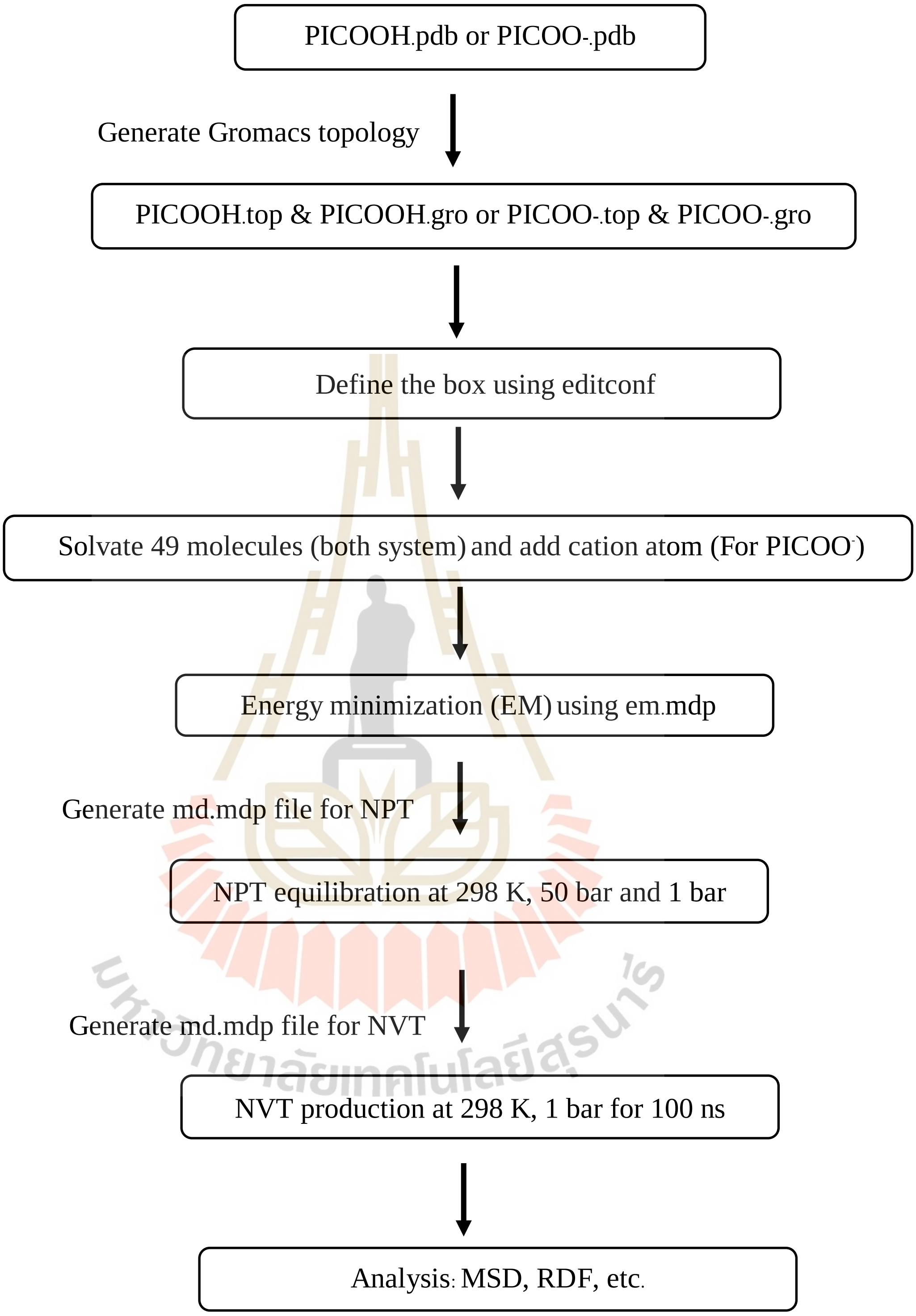
PICOOH.pdb or PICOO-.pdb
Generate Gromacs topology
PICOOH.top & PICOOH.gro or PICOO-.top & PICOO-.gro
Define the box using editconf
Solvate 49 molecules (both system) and add cation atom (For PICOO-)
Energy minimization (EM) using em.mdp
Generate md.mdp file for NPT
NPT equilibration at 298 K, 50 bar and 1 bar
Generate md.mdp file for NVT
NVT production at 298 K, 1 bar for 100 ns
Analysis: MSD, RDF, etc.

### 3.2.3 Properties from MD simulation

#### 3.2.3.1 Radial distribution function (RDF)

The radial distribution function (RDF) is an estimate of the probability of finding a particle at a distance of *r* away from a given reference particle defined as:

$$g_{AB}(r) = \frac{<\rho_B(r)>}{<\rho_B>_{local}} \tag{3.19}$$

$$g_{AB}(r) = \frac{1}{<\rho_B>_{local}} \frac{1}{N_A} \sum_{i\epsilon A}^{N_A} \sum_{j\epsilon B}^{N_B} \frac{\delta(r_{ij}-r)}{4\pi r^2} \tag{3.20}$$

where $< \rho_B(r) >$ is the density of particle B at a distance $r$ around particles A and $< \rho_B >_{local}$ is the average particle density of type B over all spheres around particles A with radius $r_{max}$ as shown in Figure 3.3. For analysis in Gromacs, the program gmx rdf divides the system into spherical parts from $r$ to $r + dr$ and make a histogram.

#### 3.2.3.2 Mean square displacement (MSD)

The MSD is a measure of the deviation of the position of particle with respect to a reference position over time defined by:

$$MSD(t) =< r^2(t) > = < |r_i(t) - r_i(0)|^2 > \tag{3.21}$$

where $r_i(t)$ is the position of the atom $i$ at the time $t$, and < > denote an ensemble average. The MSD also contains information on the self-diffusion coefficient. It is possible to investigate the behavior of the system by looking at the slope of the MSD. The self-diffusion coefficient, D can be defined by:

$$D = \lim_{t\to\infty} \frac{1}{6t} < r^2(t) > \tag{3.22}$$

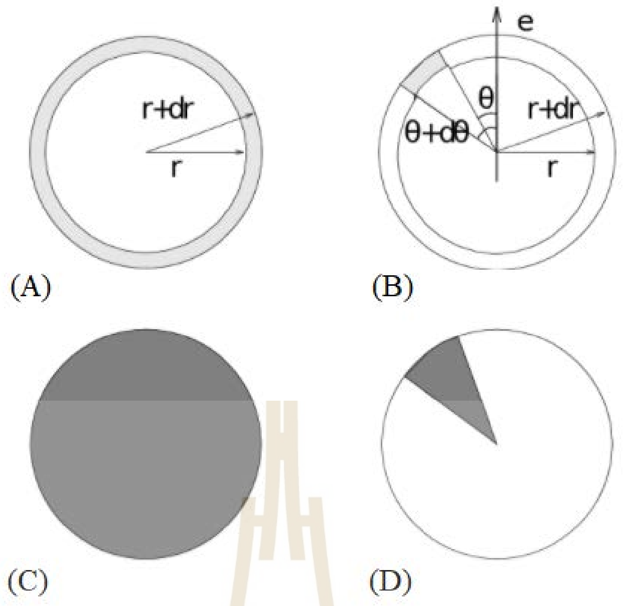

**Figure 3.3** Definition of slices in Gromacs gmx rdf: (A) $g_{AB}(r)$ and (B) $g_{AB}(r,\theta)$. The slices are colored gray (normalization volumes): (C) normalization $<\rho_B>_{local}$ and (D) normalization $<\rho_B>_{local,\theta}$.

### 3.2.3.3 Autocorrelation function (ACF)

To analyze additional dynamic properties, GROMACS has implemented various types of correlation function. For the one used in this work, the autocorrelation function $C_f(t)$ for a property $f(t)$ can be defined as:

$$C_f(t) = < f(\xi) f(\xi + t) >_{\xi} \tag{3.23}$$

where $<>_{\xi}$ is the averaging over $\xi$ such as over time origins. The integral of the correlation function over time is the correlation time, $\tau_f$:

$$\tau_f = \int_0^{\infty} C_f(t) dt \tag{3.24}$$

The correlation functions are analyzed followed by data points with discrete time intervals, $\Delta t$, so that the autocorrelation function is:

$$C_f(j\Delta t) = \frac{1}{N-j}\sum_{i=0}^{N-1-j} f(i\Delta t)f((i+j)\Delta t) \tag{3.25}$$

where $N$ is the number of available time frames for the calculation.

### 3.2.4 MD-EXAFS

Atomic coordinates from MD trajectories were used to compute the radial distribution functions (RDF) and the coordination number (CN). For each selected snapshot, a cluster of atoms was obtained by extracting all species within 6 Å from the probed ion ($Ca^{2+}$ and $K^+$). Then, the cluster was used as an input for FEFF program to calculate the EXAFS spectrum, μ(E), of the probed ion as a function of energy (E), based on a multiple scattering approach. In MD-EXAFS procedure (Merat, 2013 and Chaodamrongsakul, 2013), the average EXAFS spectrum can be obtained from:

$$\bar{\chi}(E) = \frac{\bar{\mu}(E) - \mu_0(E)}{\Delta\mu_0(E_0)} \tag{3.26}$$

where $\bar{\chi}(E)$ is the average EXAFS spectrum, $\bar{\mu}(E)$ is the averaged absorption coefficient, $\mu_0(E)$ is the background absorption coefficient and $\Delta\mu_0(E_0)$ is the jump in the absorption background at the absorption edge $(E_0)$. The EXAFS oscillations, $\chi(k)$ were determined by

$$\frac{h^2k^2}{2m} = E - E_0 \tag{3.27}$$

where $E_0$ is the absorption threshold energy and $k$ is the photoelectron wave vector. The $\chi(k)$ is expressed by:

$$\chi(k) = \sum_i \frac{N_i}{kR_i^2} F_i(k) e^{-2\sigma_i^2 k^2} e^{-2R_i/\lambda} \sin[2kR_i + \phi_i(k)] \tag{3.28}$$

where $N_i$ is the number of atoms in the i$^{\text{th}}$ shell at distance $(R_i)$ from the absorbing atom. $F_i(k)$ is the back scattering amplitude and mean-squared displacement of the neighboring atoms. $\sigma_i$ is Debye Waller factor. $\phi_i$ is the phase shift of the photoelectron. The Fourier transform of $\chi(k)$ is calculated (Newville, 1995) and Eq. (3.28) is transformed to:

$$\chi(R) = \frac{1}{\sqrt{2\pi}} \int_0^\infty k^2 \bar{\chi}(k) W(k) e^{i2kR} dk \tag{3.29}$$

where $W(k)$ is a handing window. Selected configurations from MD trajectory were used to create EXAFS spectrum and the average spectrum was compared with experimental data.

# CHAPTER IV

# RESULTS AND DISCUSSION

## 4.1 Crystallization of linear and short-branched polypropylene

### 4.1.1 Polymer samples

Two types of samples were kindly provided as gifts from Beijing Research Institute of Chemistry and Industry, SINOPEC, China. Two G-resin samples are denoted by MT12-s and MT18-s which are *i*PP containing some 1-butene defects. The other sample is the linear *i*PP homopolymer (denoted as V30G) and is used for comparison. The specimens were prepared by compression molding at 180-190 °C to obtain thin films with 1 mm thickness.  The number and weight averaged molecular weight ($M_n$ and $M_w$) and polydispersity index (*PDI*) were determined by gel permeation chromatography (GPC), Polymer Char GPC-IR5, using 1,2,4-Trichlorobenzene as the solvent. The content of 1-butene was determined by nuclear magnetic resonance ($^{13}$C-NMR) spectroscopy. The solutions for the measurement were prepared by dissolving the samples (~10 wt%) in 1,2-dichlorobenzene-$d_4$/1,2,4-trichlorobenzene solvent (2:3 v/v). The measurements were conducted on a AV600 spectrometer (Bruker, Germany) at 120°C with the number of scans set to 2048. The details information for all samples are listed in Table 4.1.

**Table 4.1** Sample characterization.

| Sample | $M_w$ (g/mol) | $M_n$ (g/mol) | Dispersity ($M_w/M_n$) | MFR (melt flow rate)* | 1-butene (wt%) |
|---|---|---|---|---|---|
| V30G | 233,421 | 30,407 | 7.68 | 23.30 | - |
| MT12-s | 282,578 | 38,567 | 7.33 | 13.28 | 6.43 |
| MT18-s | 236,499 | 34,753 | 6.81 | 19.68 | 5.20 |

*MFR in unit g/10 min at the load of 2.16 kg/230°C

### 4.1.2 Nuclear magnetic resonance (NMR) spectroscopy

NMR measurement was conducted to determine the content of 1-butene defect. NMR spectra of all PP samples were shown in Figure 3.1.1 and Table 4.2 presents the chemical shift, signal assignment and the relative peak area from the spectra. For PP chain, every αα-$CH_2$, CH and $CH_3$ counts as 100% propylene fragment. The amount of propylene signal can be obtained as 1/3 of these three peak area in summation multiplied by 42.08 (molecular weight of propylene) as (Lee, 1996)

$$P = \frac{1}{3}[I_{\alpha\alpha-CH_2} + I_{CH} + I_{CH_3}] \times 42.08 \tag{4.1}$$

where I is the area at each specified NMR peak. Similarly, the amount of 1-butene signal can be determined as 1/4 of the peak area summation of αα-$CH_2$, CH, 2-$CH_2$ and $CH_3$ of 1-butene unit multiplied by 56.11 (molecular weight of 1-butene) as following

$$B = \frac{1}{4} \times [I_{\alpha\alpha-CH_2 \, of \, B} + I_{CH \, of \, B} + I_{2-CH_2 \, of \, B} + I_{CH_3 \, of \, B}] \times 56.11 \tag{4.2}$$

For MT12-s, the peak areas of propylene signal are $I_{\alpha\alpha-CH_2}$ (46.10 ppm) = 15.40, $I_{CH}$ (28.50 ppm) = 18.01 and $I_{CH_3}$(21.40 ppm) = 18.56 while for 1-butene signal are $I_{\alpha\alpha-CH_2 \text{of B}}$ (46.39 ppm) = 1.21, $I_{CH \text{ of B}}$ (34.92 ppm) = 0.69, $I_{2-CH_2 \text{of B}}$ (27.90 ppm) = 0.67 and $I_{CH_3 \text{of B}}$ (10.66 ppm) = 1.00. By substitute these values into Eq. (1) - (2), P = 728.97 and B = 50.08 are obtained.

Similarly, in the case of MT18-s, the peak areas of propylene signal are $I_{\alpha\alpha-CH_2}$( 46.10 ppm) = 23.86, $I_{CH}$ (28.51 ppm) = 28.46 and $I_{CH_3}$(21.41 ppm) = 30.16 whereas for 1-butene signal are $I_{\alpha\alpha-CH_2 \text{of B}}$ (46.39 ppm) = 1.95, $I_{CH \text{ of B}}$ (34.93 ppm) = 0.88, $I_{2-CH_2 \text{of B}}$ ( 27.90 ppm) = 0.69 and $I_{CH_3 \text{of B}}$ (10.65 ppm) = 1.00. Based on these parameters and Eq. (1)-(2), P = 1156.92 and B = 63.40 are determined.

Once the amount of propylene and 1-butene signal are known, the 1-butene content in PP chain can be evaluated using

$$B(\text{wt\%}) = [\frac{B}{B+P}] \times 100 \tag{4.3}$$

Based on the calculation using Eq. (4.3), the amount of 1-butene content in MT12-s and MT18-s samples are 6.43 and 5.20 wt%, respectively.

**Table 4.2** The chemical shift, signal assignment and peak area for $^{13}C$ NMR spectrum of V30G, MT12-s and MT18-s samples.

| Sample | Chemical shift (ppm) | Assignment | Peak area |
|---|---|---|---|
| V30G | 46.11 | αα-$CH_2$ of PPPP | 0.96 |
| | 28.51 | CH of PPPP | 0.92 |
| | 21.42 | $CH_3$ of PPPP | 1.00 |
| MT12-s | 46.39 | αα-$CH_2$ of PPPB | 1.21 |
| | 46.10 | αα-$CH_2$ of PPPP | 15.40 |
| | 42.98 | αα-$CH_2$ of PPBP + BPBB | 1.19 |
| | 34.92 | CH of B | 0.69 |
| | 28.50 | CH of PPP | 18.01 |
| | 27.90 | 2-$CH_2$ of PBP | 0.67 |
| | 21.40 | $CH_3$ of PPPPP | 18.56 |
| | 10.66 | $CH_3$ of PBP | 1.00 |
| MT18-s | 46.39 | αα-$CH_2$ of PPPB | 1.95 |
| | 46.10 | αα-$CH_2$ of PPPP | 23.86 |
| | 42.98 | αα-$CH_2$ of PPBP + BPBB | 2.27 |
| | 34.93 | CH of B | 0.88 |
| | 28.51 | CH of PPP | 28.46 |
| | 27.90 | 2-$CH_2$ of PBP | 0.69 |
| | 21.41 | $CH_3$ of PPPPP | 30.16 |
| | 10.65 | $CH_3$ of PBP | 1.00 |

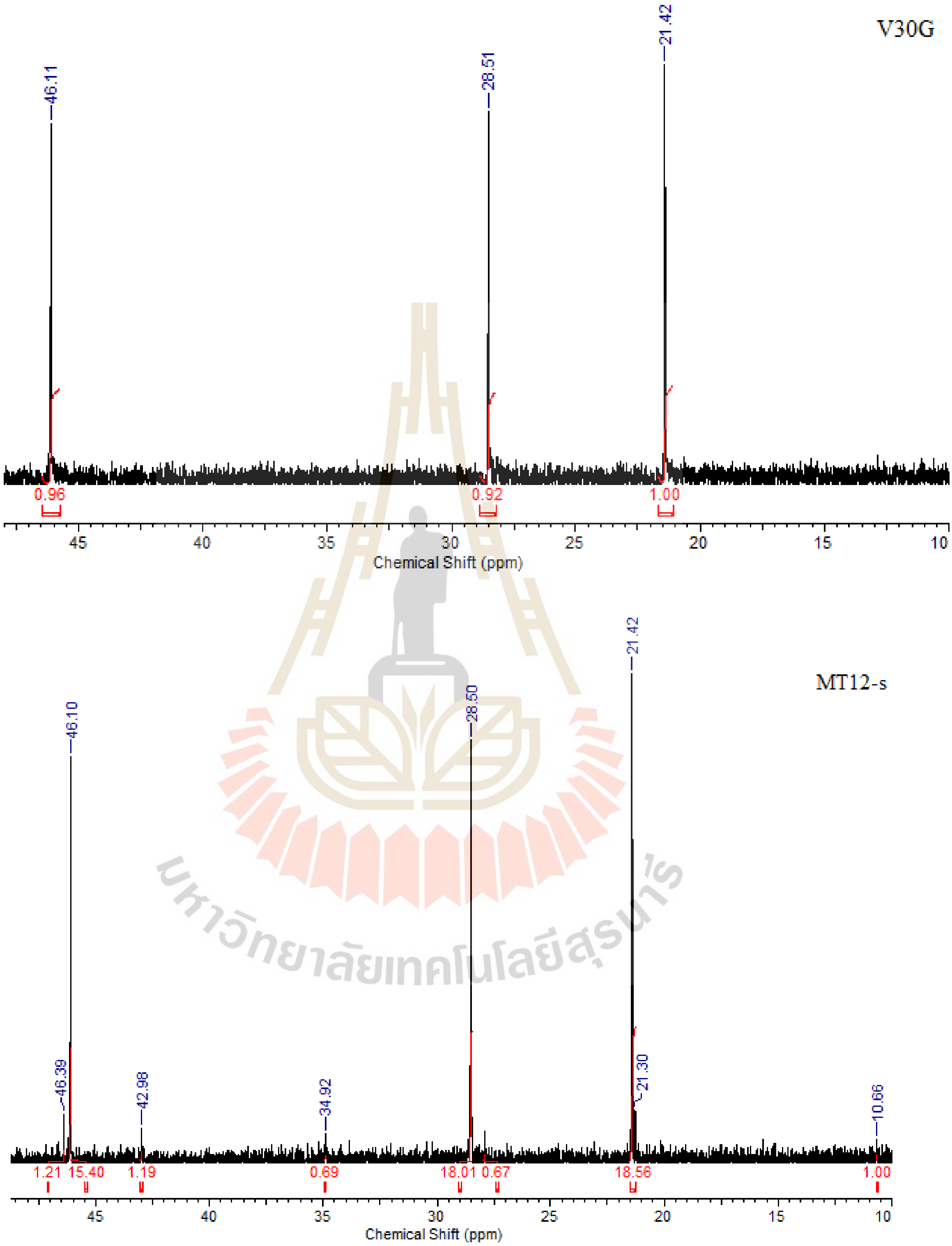

**Figure 4.1** $^{13}C$ NMR spectra of V30G, MT12-s and MT18-s dissolved in 1,2-dichlorobenzene-$d_4$/1,2,4-trichlorobenzene (2:3 v/v) and measured at 120°C.

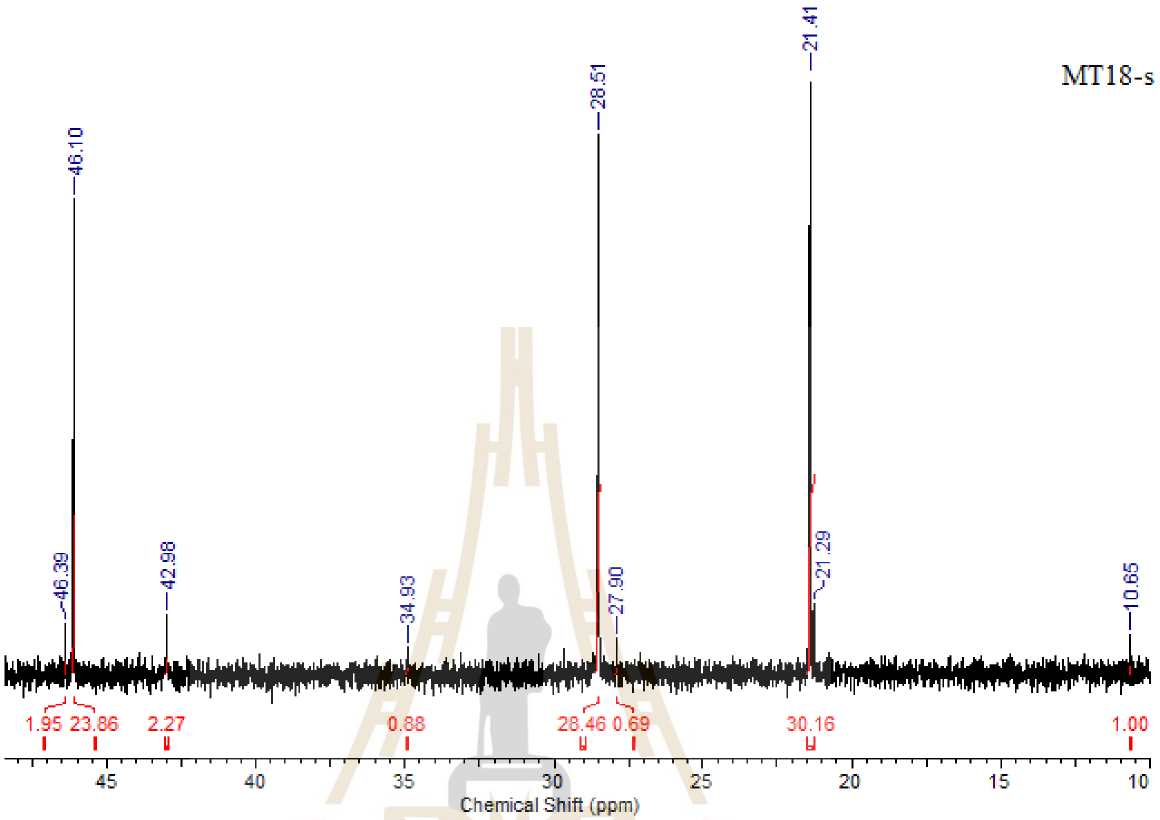

**Figure 4.1** (Continued) $^{13}$C NMR spectra of V30G, MT12-s and MT18-s dissolved in 1,2-dichlorobenzene-$d_4$/1,2,4-trichlorobenzene (2:3 v/v) and measured at 120°C.

### 4.1.3 Polarized optical microscopy (POM)

POM was employed to study the sample morphologies and to evaluate the spherulite growth rate as a function of time for the crystallization temperature at 135°C. Figure 4.2 depicts the evolution of the spherulite growth processes for V30G. On the other hand, the crystal sizes for MT12-s and MT18-s samples were too small to study their growth rate by POM. Figure 4.3 can show only the observed morphologies of MT12-s and MT18-s samples. From Figure 4.3, it can be seen that PP spherulites grow from the center point, *i.e.* the nuclei, gradually outward with time. The negative spherulites are observed for V30G but cannot be identified for MT12-s and MT18-s. These results suggest that 1-butene defects should have some impact on the formation of negative spherulites and cause smaller spherulites size. For MT12-s and MT18-s, the crystallization process starts quickly but with very small crystal size (impossible to determine the crystal size in this work). Therefore, it is unlikely to compare the crystal size for all PP samples.

The growth of the spherulite size for V30G at each crystallization temperature is linearly proportional to the crystallization time. The spherulite radius is varied with crystallization time, indicating a nucleation dominated crystal growth process. The linear crystalline growth rates of V30G vs. crystallization temperature is presented in Figure 4.4 and the slope of spherulites radius (Figure 4.4) at each crystallization temperature is presented in Figure 4.5. It can be seen that the growth rate become slower with increasing crystallization temperature.

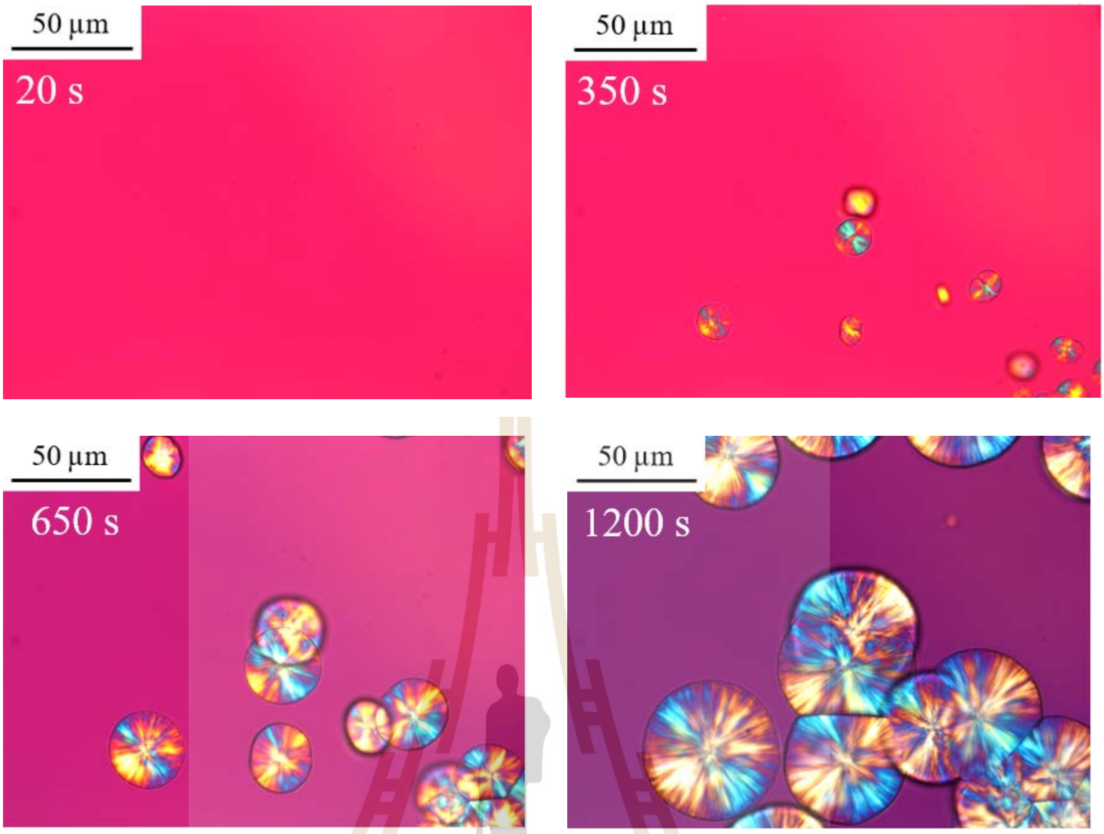

**Figure 4.2** Polarized optical micrographs as a function of time of V30G sample taken during the isothermal crystallization at 135°C.

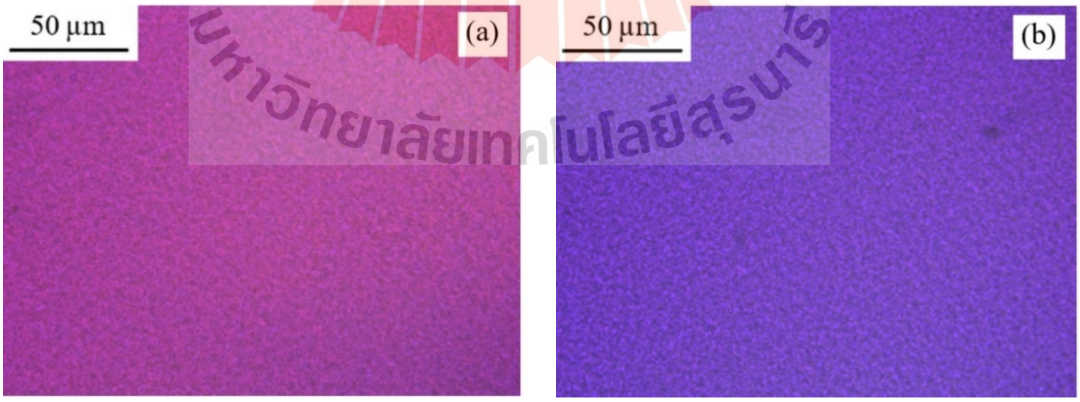

**Figure 4.3** Polarized optical micrographs of (a) MT12-s and (b) MT18-s samples taken during the isothermal crystallization at 135°C.

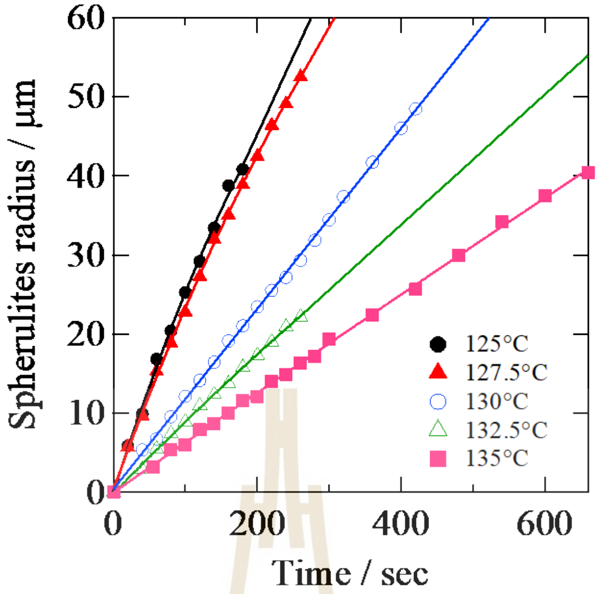

**Figure 4.4** The linear relationship between the spherulite radius and the crystallization time for V30G sample determined from POM at different isothermal crystallization temperature.

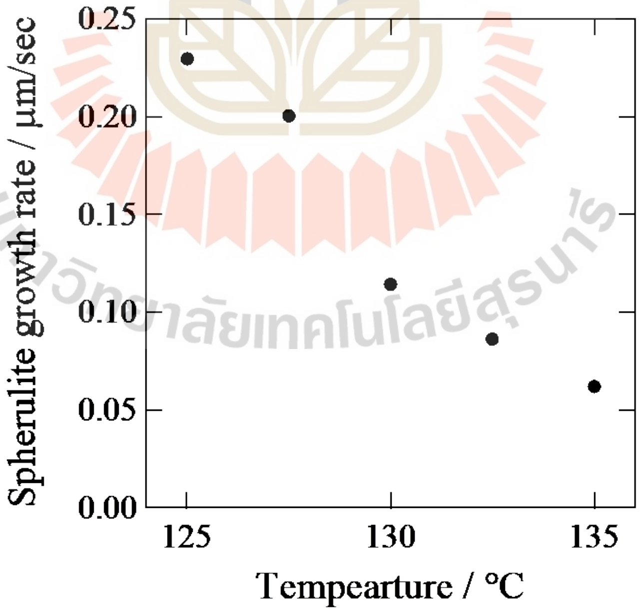

**Figure 4.5** The spherulite growth rate as a function of different crystallization temperatures.

### 4.1.4 Differential scanning calorimeter (DSC)

#### 4.1.4.1 Isothermal crystallization

The isothermal crystallization kinetics of all PP samples in the temperature range of 125-135°C was investigated and compared. Figure 4.6 depicts the DSC thermograms of isothermal crystallization of PP samples at different crystallization temperatures. Each plot shows the complete thermogram with crystallization peak. As observed in Figure 4.6, the height of crystallization peaks decrease as the crystallization temperatures increases. The time to complete crystallization also increases with an increase in the crystallization temperatures. For comparison with the same crystallization temperature, Figure 4.7 presents DSC thermograms of isothermal crystallization at 130°C for all samples. It can be inferred that the crystallization isotherm were shifted to shorter times for *i*PP samples with 1-butene defects, indicating that the short branch (1-butene) defects can accelerate the crystallization process of *i*PP.

The degree of crystallinity ($\emptyset_{DSC}$) can be calculated from the exothermic peak area at time *t* by

$$\emptyset_{DSC}(t) = \frac{\int_0^t H(t)dt}{\Delta H_m^0} \tag{4.4}$$

where $H(t)$ is the enthalpy of crystallization released during an infinitesimal time interval $dt$ and $\Delta H_m^0$ is the enthalpy of fusion for the perfect (100%) *i*PP crystal, $\Delta H_m^0$ = 207 J/g[16]. From Figure 4.7(b), it can be seen that both induction period and the final degree of crystallinity are decreased for PP samples with 1-butene defects. The induction period and the inverse of the crystallization half-time as a function of crystallization temperature are plotted in Figure 4.8. From Figure 4.8(a), the induction time as a function of crystallization temperature exhibits a parabolic curve thereby producing a minimum induction period. The induction period is reduced when PP samples contain 1-butene defects at all crystallization temperatures. The crystallization half-time ($t_{0.5}$), defined as the time when the crystallinity reaches a half of the final crystallinity, are shown in Figure 4.8(b). These results suggest that the crystallization is significantly faster for PP with 1-butene defect. It should be noted that the induction time is decreased and the crystallization is accelerated for branched PP. In general, isothermal crystallization kinetics of polymer can be analyzed using Avrami theory[17-19] which can be used to relate the degree of crystallinity as a function of time as following

$$\frac{\emptyset(t)}{\emptyset\infty} = 1 - \exp[-k(t - t_0)^n] \tag{4.5}$$

$$\log\left[-\ln\left(1 - \frac{\emptyset(t)}{\emptyset\infty}\right)\right] = n\log(k) + n\log(t - t_0) \tag{4.6}$$

where $\emptyset^{\infty}$ is the degree of crystallinity after the complete crystallization, $t_0$ is the induction period for the crystallization and *k* and *n* are the crystallization rate constant (contributions from the nucleation and growth of crystal) and the Avrami exponent (the dimensionality of growing crystallites), respectively.

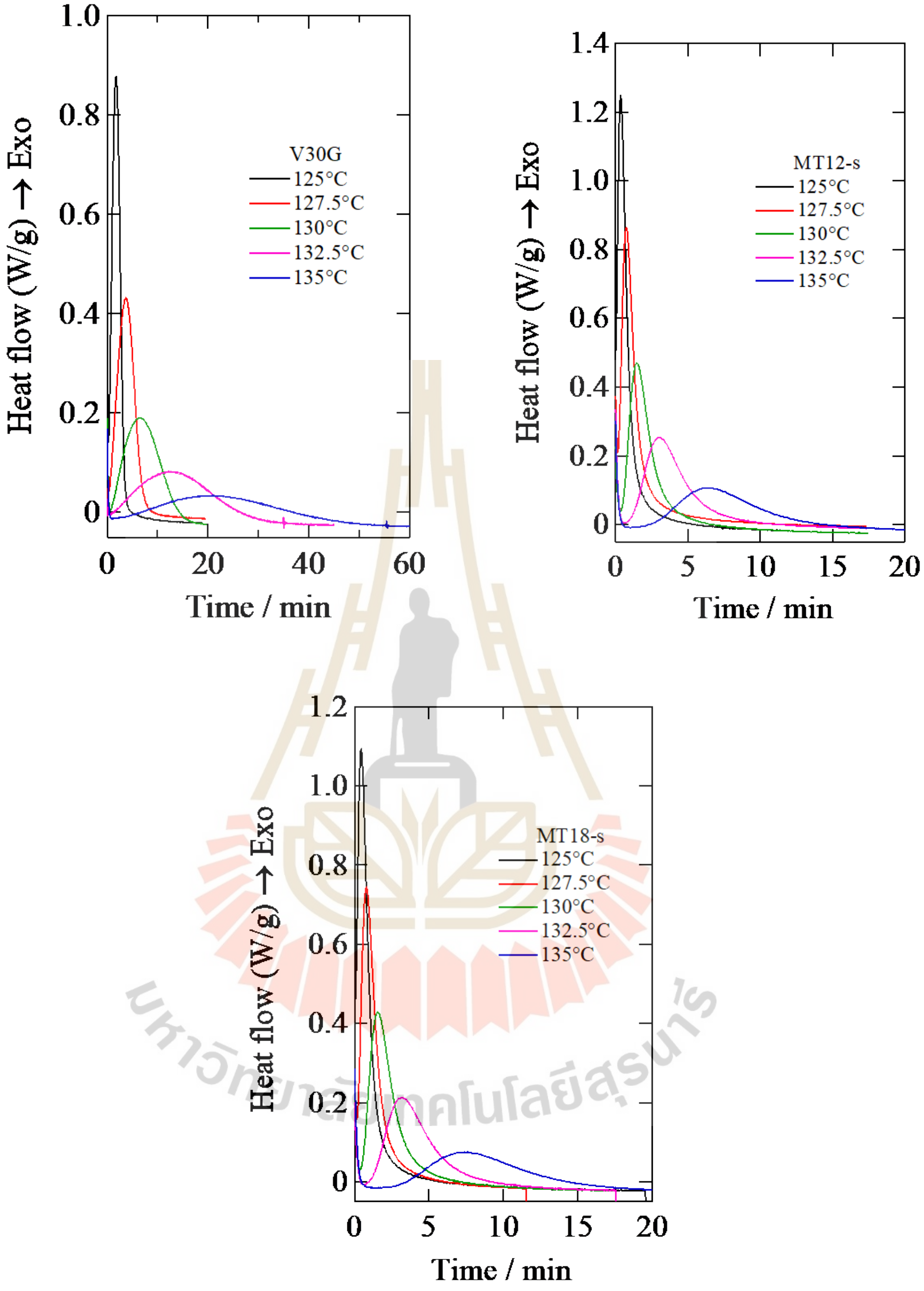

**Figure 4.6** Heat flow as a function of time during isothermal crystallization at different crystallization temperatures.

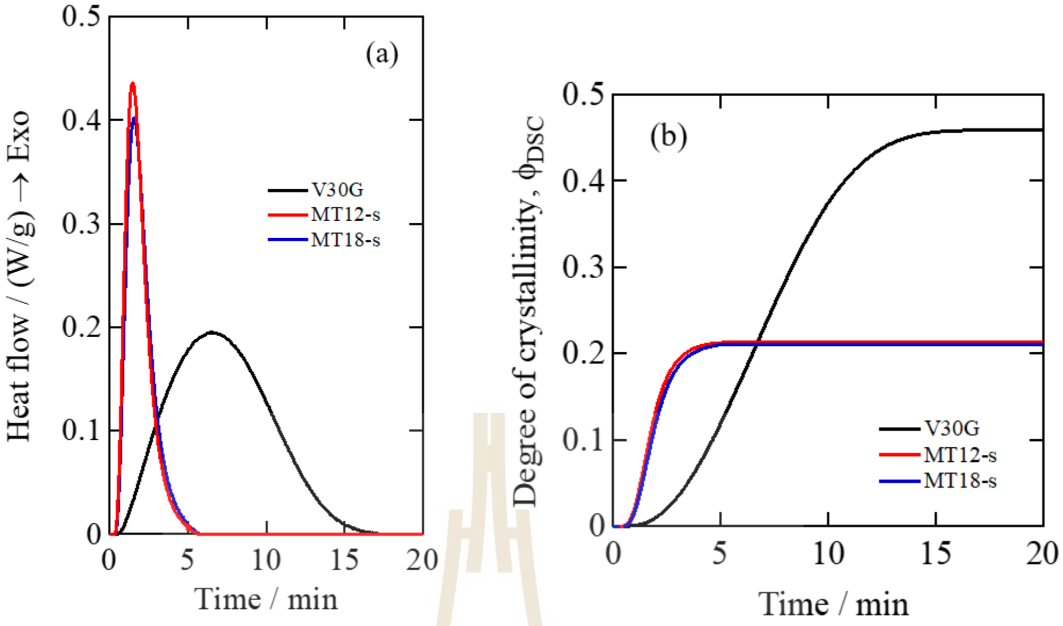

**Figure 4.7** (a) Heat flow as a function of time during isothermal crystallization at 130°C and (b) degree of crystallinity ($\emptyset_{DSC}$) as a function of time.

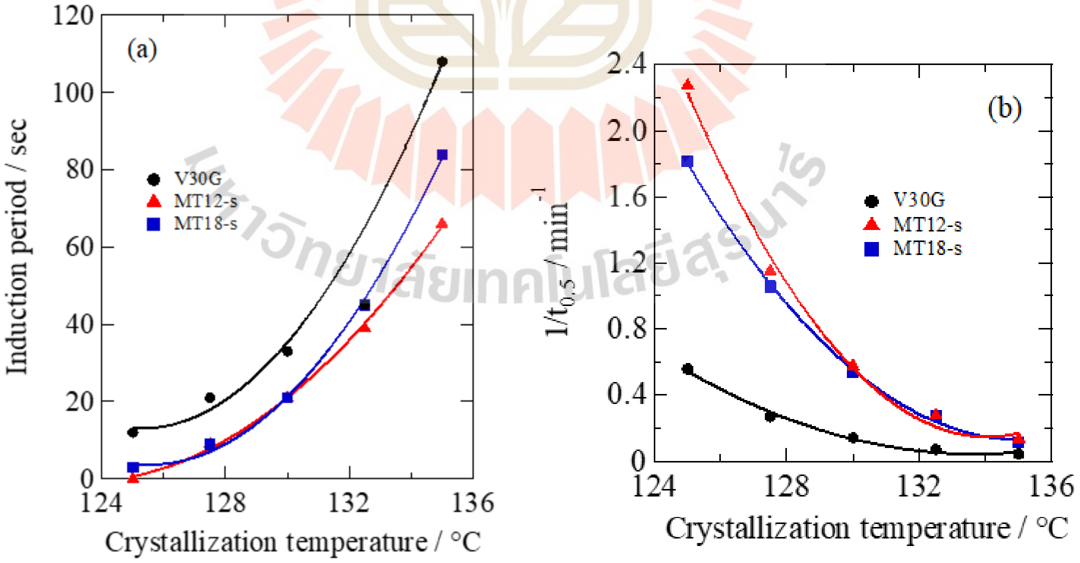

**Figure 4.8** (a) Induction period and (b) inverse of the crystallization half-time ($t_{0.5}$) as a function of crystallization temperature of PP samples.

The Avrami plots at 130°C for V30G, MT12-s and MT18-s are shown in Figure 4.9. In the early stage of the crystallization, the Avrami exponents ($n$) for all samples are in the range of 2-3 which suggests that the crystal growth has two or three dimension by assuming the inhomogeneous nucleation. In the case of V30G, there is no crossover behavior because $n$ in the later stages does not change. On the other hand, $n$ is decreased to 1.74 (MT12-s) and 1.88 (MT18-s) related to the change in mode of crystallization. For $n$ and $k$ at other temperatures, as shown in Figure 4.10, the trend of $n$ can be generally ordered as: V30G < MT12-s < MT18-s. The $k$ values are decreased with increasing crystallization temperature which is related to slower crystallization of all samples at higher crystallization temperature. Similarly, both MT12-s and MT18-s have faster crystallization tendency than that of V30G.

The equilibrium melting temperature ($\mathrm{T_m^0}$ ) is an important thermodynamic parameter defined as the melting temperature of lamella crystal at infinite thickness. In practice, $\mathrm{T_m^0}$ can be evaluated by the Hoffman–Weeks method (Hoffman, 1962). For this technique, the measured melting points of each polymer samples crystallized at different temperatures are plotted versus the crystallization temperature. The extrapolation of the linear fit to the $\mathrm{T_c} = \mathrm{T_m}$ line are shown in Figure 4.11. In this work, we utilize the model described by the following relation

$$\mathrm{T_m} = \mathrm{T_m^0}\left(1 - \frac{1}{\beta}\right) + \frac{\mathrm{T_c}}{\beta} \tag{4.7}$$

where $T_m$ is the observed melting temperature of a crystal formed at a temperature $\mathrm{T_c}$ and β is the thickening parameter equal to $L_c/L_c^*$. In this work, our DSC data give $\mathrm{T_m^0}$ = 189.2°C, 163.8°C and 161.4°C for V30G, MT12-s and MT18-s, respectively.

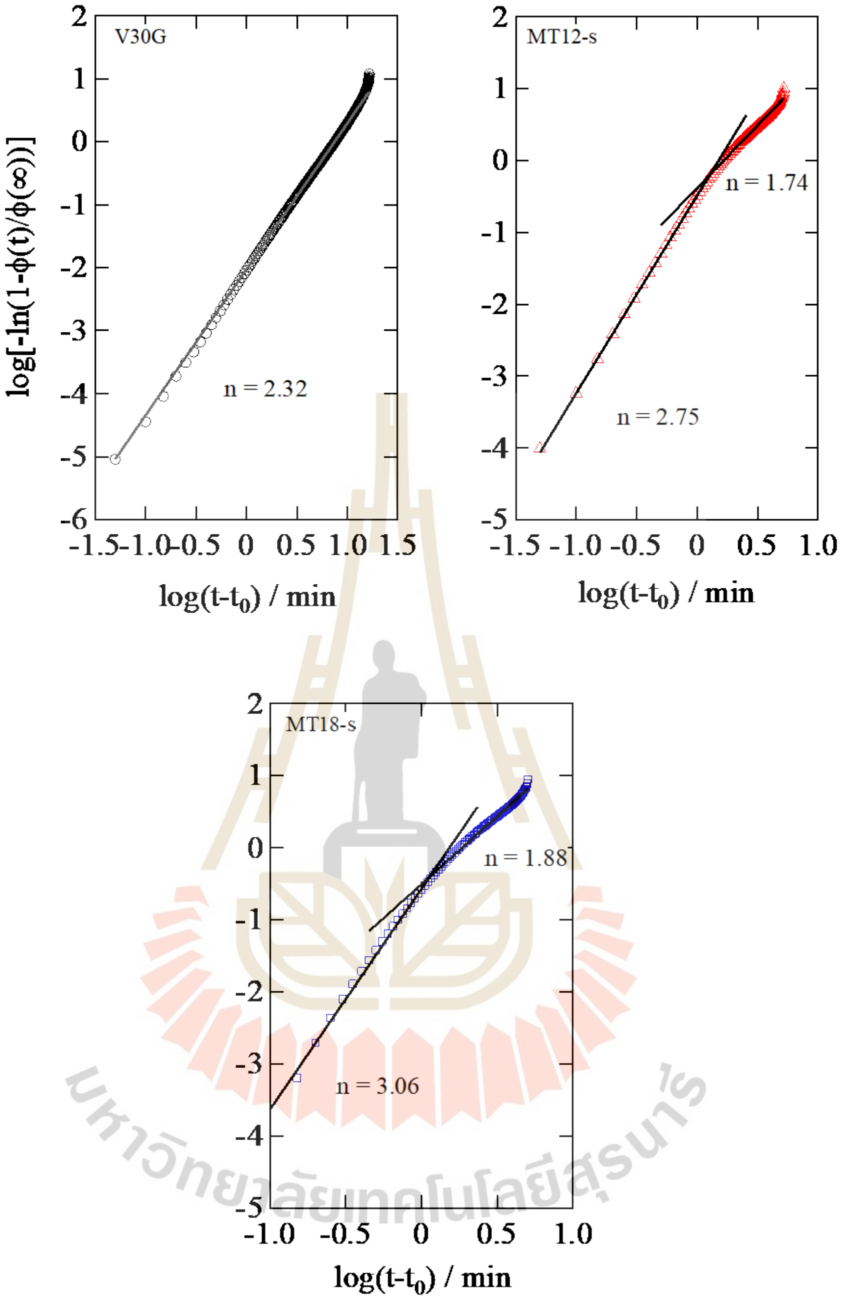

**Figure 4.9** Avrami plots at 130°C based on DSC results for all samples.

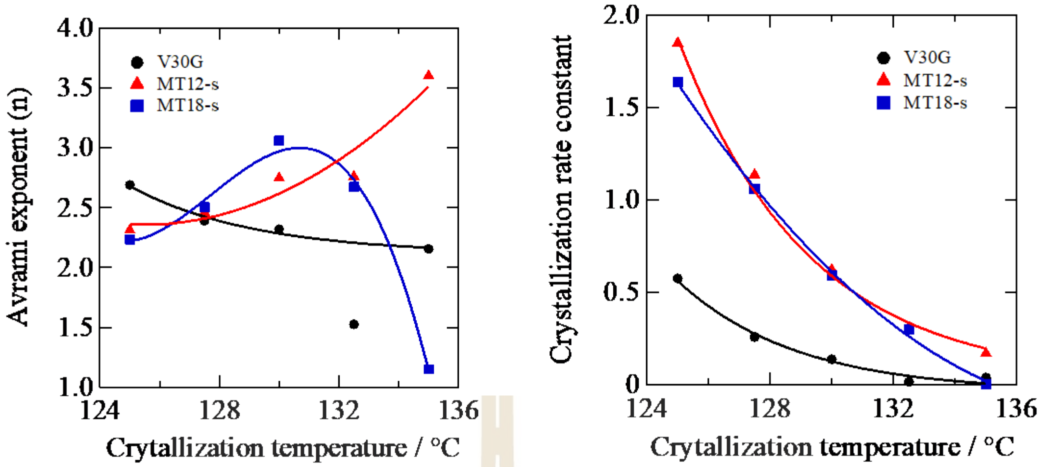

**Figure 4.10** (left) Avrami exponent and (right) the crystallization rate constant as a function of crystallization temperature.

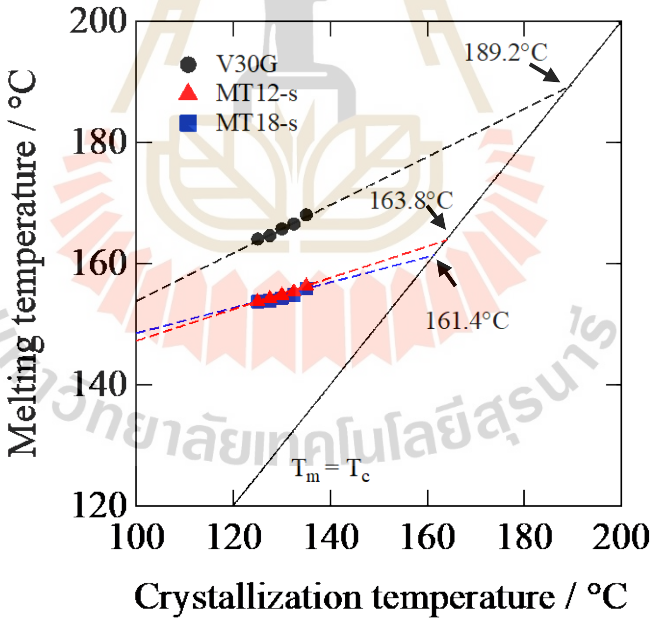

**Figure 4.11** Hoffman–Weeks plots for determination of the equilibrium melting temperature.

### 4.1.4.2 Non-isothermal crystallization

As most of industrial processes generally proceed under non-isothermal conditions, the crystallization in a continuously changing temperature is of practical interest. During non-isothermal crystallization process, the kinetics of crystallization can be evaluated from the heat flow versus temperature. Figure 4.12 depicts non-isothermal DSC thermograms of V30G, MT12-s and MT18-s at different cooling rates ranging from 5 to 30°C/min. The characteristic data including the crystallization onset temperature ($T_i$), the crystallization peak temperature ($T_p$), and the crystallization enthalpy ($\Delta H_c$) are summarized in Table 4.3. Both crystallization onset and peak temperatures tend to decrease with faster cooling rate and the crystallization tend to initiate earlier at slower cooling rate. The relative crystallinity, as a function of temperature, $X(\mathrm{T})$ can be obtained according to (Zeng, 2008):

$$X(\mathrm{T}) = \frac{\int_{T_i}^{T}(dH/dT)\mathrm{dT}}{\int_{T_i}^{T\infty}(dH/dT)\mathrm{dT}} \qquad (4.8)$$

where $dH$ is the enthalpy of crystallization during an infinitesimal time interval $dT$, $T_i$ is the onset crystallization temperature and $\mathrm{T}_\infty$ is the end crystallization temperature. The relative degree crystallinity at different cooling rates as a function of temperature, can be also calculated according to the Eq. (4.8). Figure 4.13 presents the relationship between $X(\mathrm{T})$ as a function of temperature. Obviously, the changes in the percent of crystallinity for all PP samples are dependent on the cooling rate. The temperature of polymer samples gradually decreases as the crystallization rate is increased. These results indicate the existence of slow nucleation stage and fast primary crystallization stage in different temperature ranges.

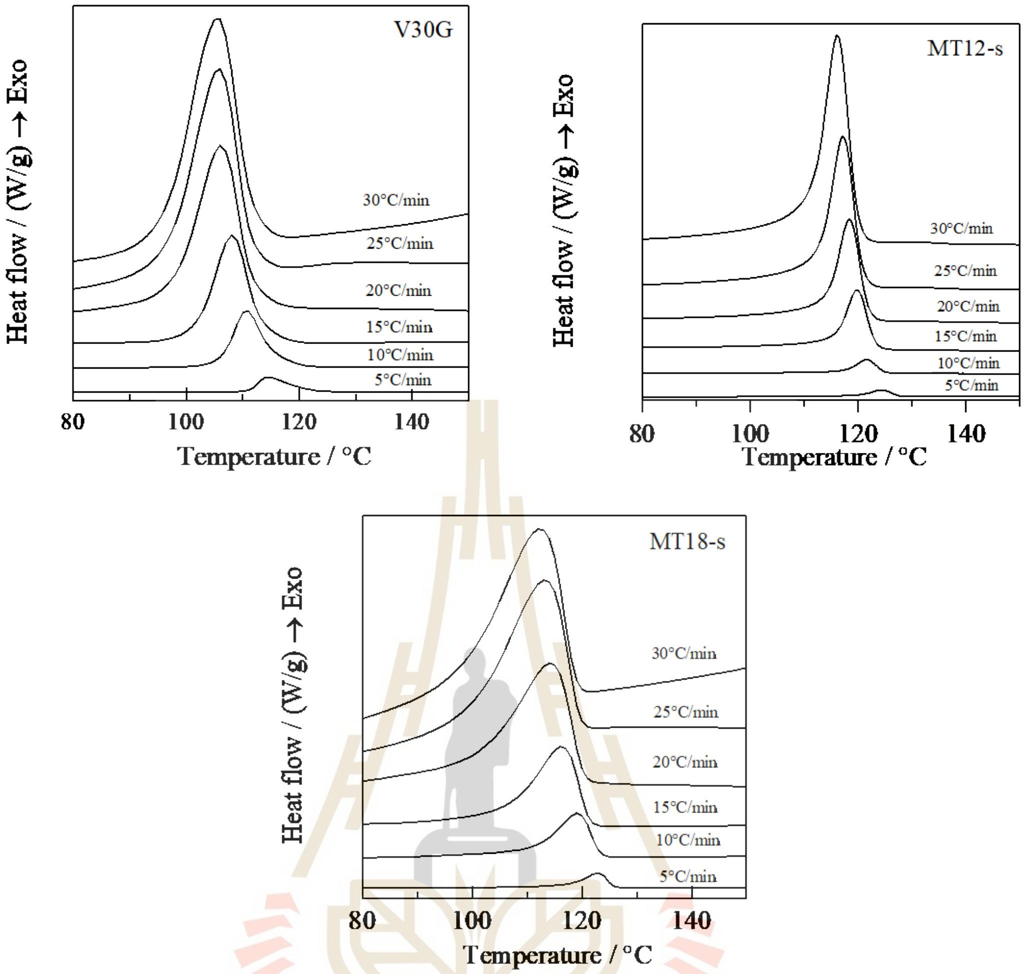

**Figure 4.12** DSC thermograms for non-isothermal melt-crystallization of three PP samples at different cooling rates.

**Table 4.3** Non-isothermal crystallization parameters for V30G, MT12-s and MT18-s.

| Sample | Cooling rate (°C/min) | Ti (°C) | Tp (°C) | *ΔHc* (J/g) |
|---|---|---|---|---|
| V30G | 5 | 111.8 | 114.6 | -99.13 |
| | 10 | 106.8 | 111.0 | -97.92 |
| | 15 | 102.9 | 108.8 | -95.07 |
| | 20 | 99.5 | 106.9 | -93.72 |
| | 25 | 97.6 | 106.0 | -98.28 |
| | 30 | 97.5 | 106.1 | -92.44 |
| MT12-s | 5 | 116.8 | 124.4 | -74.36 |
| | 10 | 115.3 | 121.5 | -93.33 |
| | 15 | 113.4 | 119.7 | -73.07 |
| | 20 | 112.3 | 118.3 | -71.34 |
| | 25 | 110.3 | 117.1 | -71.03 |
| | 30 | 109.4 | 116.0 | -70.20 |
| MT18-s | 5 | 118.6 | 123.1 | -69.90 |
| | 10 | 112.4 | 119.6 | -75.62 |
| | 15 | 108.2 | 117.0 | -74.50 |
| | 20 | 102.3 | 114.4 | -80.89 |
| | 25 | 100.5 | 112.8 | -78.17 |
| | 30 | 99.4 | 112.6 | -77.10 |

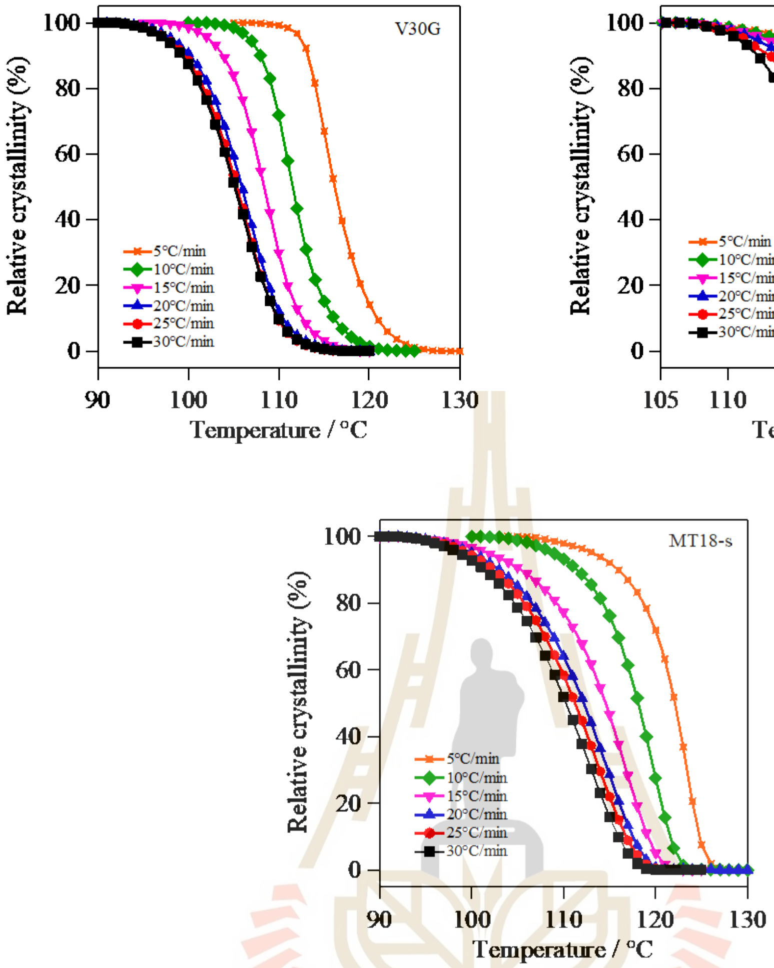

**Figure 4.13** Relative crystallinity versus temperature for three PP samples at different cooling rates.

### 4.1.5 Small Angle X-ray Scattering (SAXS)

To study polymer crystallization and morphology change, the scattering profile is corrected for beam intensity, sample transmission, background scattering and converted to Lorentz corrected SAXS profile by multiplying by $q^2$ (Vonk, 1967). The scattering vectors is defined as (Glatter, 1982):

$$q = (4\pi/\lambda)\sin\theta \tag{4.9}$$

Here, $q$ denotes the magnitude of the scattering vector, $\lambda$ is wavelength of X-ray and $\theta$ is the scattering angle. Raw SAXS profiles ($I(q)$ vs. $q$) for all PP samples are depicted in Figure 4.14 and the Lorentz-corrected SAXS profiles ($q^2I(q)$ vs. $q$) are presented in Figure 4.15. At time about 35-40 s, all specimens have clear scattering peaks indicating the development of lamellar stacking sandwiching the amorphous layer. The maximum peak intensities are at $q$ = 0.32, 0.23, and 0.19 $\text{nm}^{-1}$ for V30G, MT12-s and MT18-s, respectively. The location of SAXS peak moves toward higher $q$ as the crystallization proceeds. From the position of the first-peak ($q^*$), the long period ($D$) of the lamellar stacks can be evaluated as $D = 2\pi/q^*$. It is clearly observed that $D$ is decreased as a function of time after 100 *s* and then reached a constant value ($D^{\infty}$).

To evaluate the crystalline lamellar thickness ($L$) to get more details about isothermal crystallization behavior, the correlation function $\gamma(r)$ was employed to analyze the 1d-SAXS profile through the inverse Fourier transform method (Strobl, 1966).

$$\gamma(r) = \frac{\int_0^{\infty} I(q)q^2 \cos(qr)dq}{\int_0^{\infty} I(q)q^2 dq} \tag{4.10}$$

where $\gamma(r)$ is the correlation function and $r$ is the distance in the real space.

The calculated $L$, $D$ and $L/D$ ratio as a function of time during isothermal crystallization with the temperature jump from 200°C to 130°C are shown in Figure 4.16. The $D^{\infty}$ values of MT12-s and MT18-s samples are larger than that of V30G as shown in Figure 4.16(a). Comparison between these two branched samples, there is no significant difference for their D values. As shown in Figure 4.16(b), the average lamellar thickness increases with time, suggesting that the lamellae growth can be confirmed for all PP samples.

Less dense crystallites may be formed in the early stages. In the ongoing crystallization process, $L$ is increased, but the densification of the less dense crystallites may be formed and occurred in the intermediate stage. This process results in a decrease in $L$. Due to quick crystallization of PP with defects, the overshooting of $L$ is more pronounced. The long period ($D$) decreases mainly due to the decrease in the volume upon crystallization (lamella crystal’s density is higher than amorphous’s density, $\rho_c > \rho_a$), with some part of the amorphous layer is rearranged in a higher-order structure and contributes to the development of thicker lamellae. Hence, it is more important to check the ratio of the lamellar thickness and the long period which seems to be the crystallinity in the stacks of the lamella. The $L/D$ ratio are presented in Figure 4.16(c) and V30G exhibit the highest ratio which is obviously much higher than those for MT12-s and MT18-s. Hence, 1-butene defects affected the crystallization of PP and decreased the crystallinity, as shown in Figure 4.7(b).

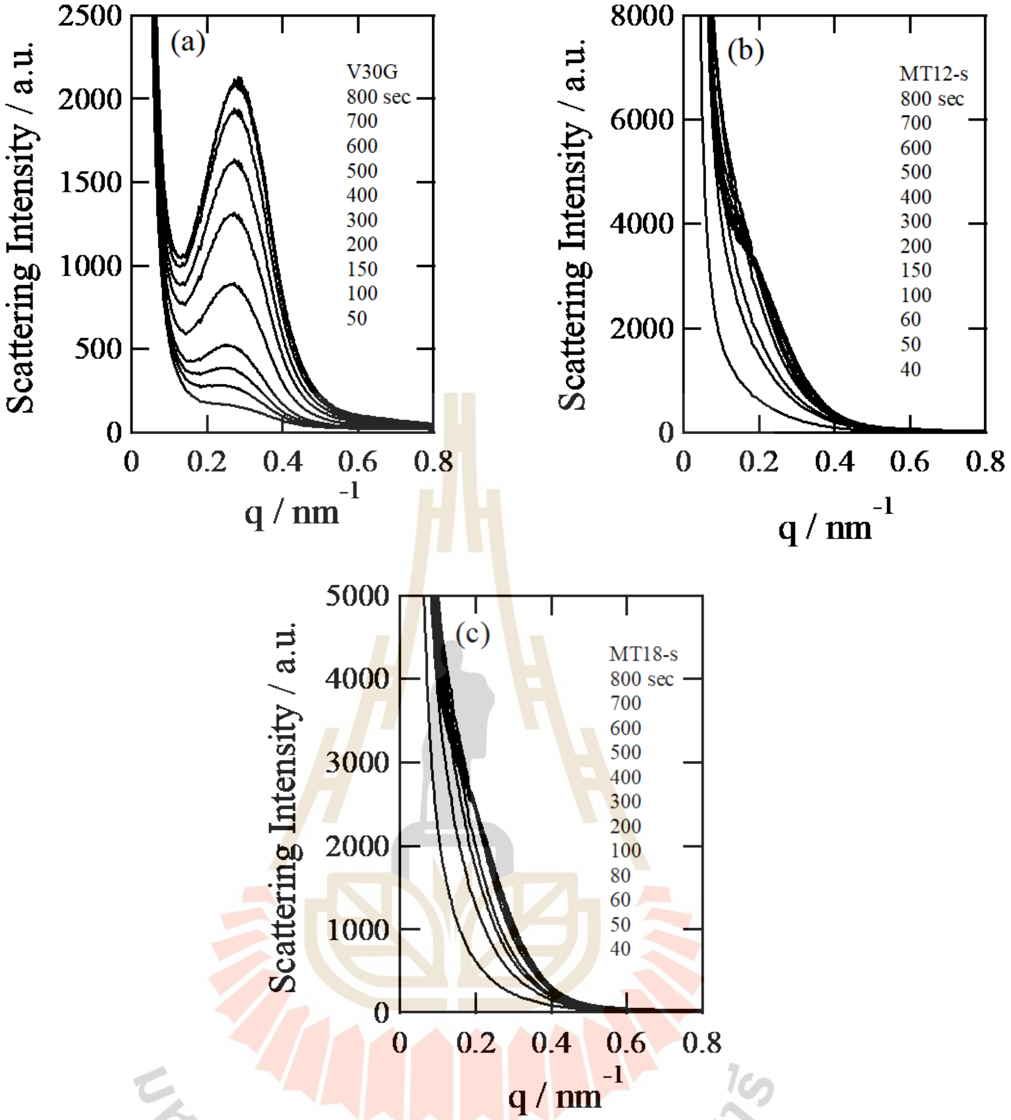

**Figure 4.14** The 1d-SAXS profiles for (a) V30G, (b) MT12-s, and (c) MT18-s during isothermal crystallization at 130°C.

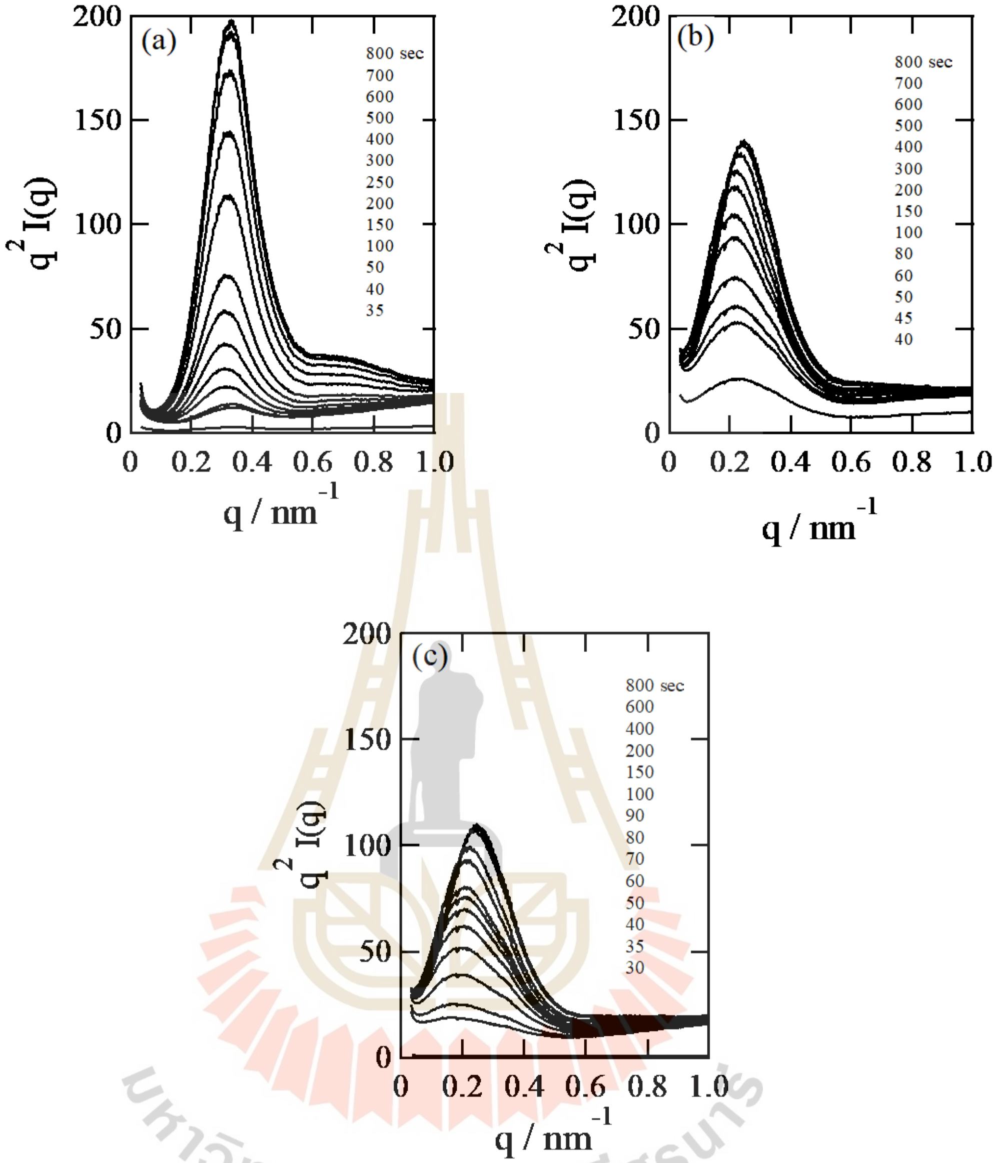

**Figure 4.15** Lorentz-corrected SAXS profiles as a function of time for (a) V30G, (b) MT12-s, and (c) MT18-s during isothermal crystallization at 130°C.

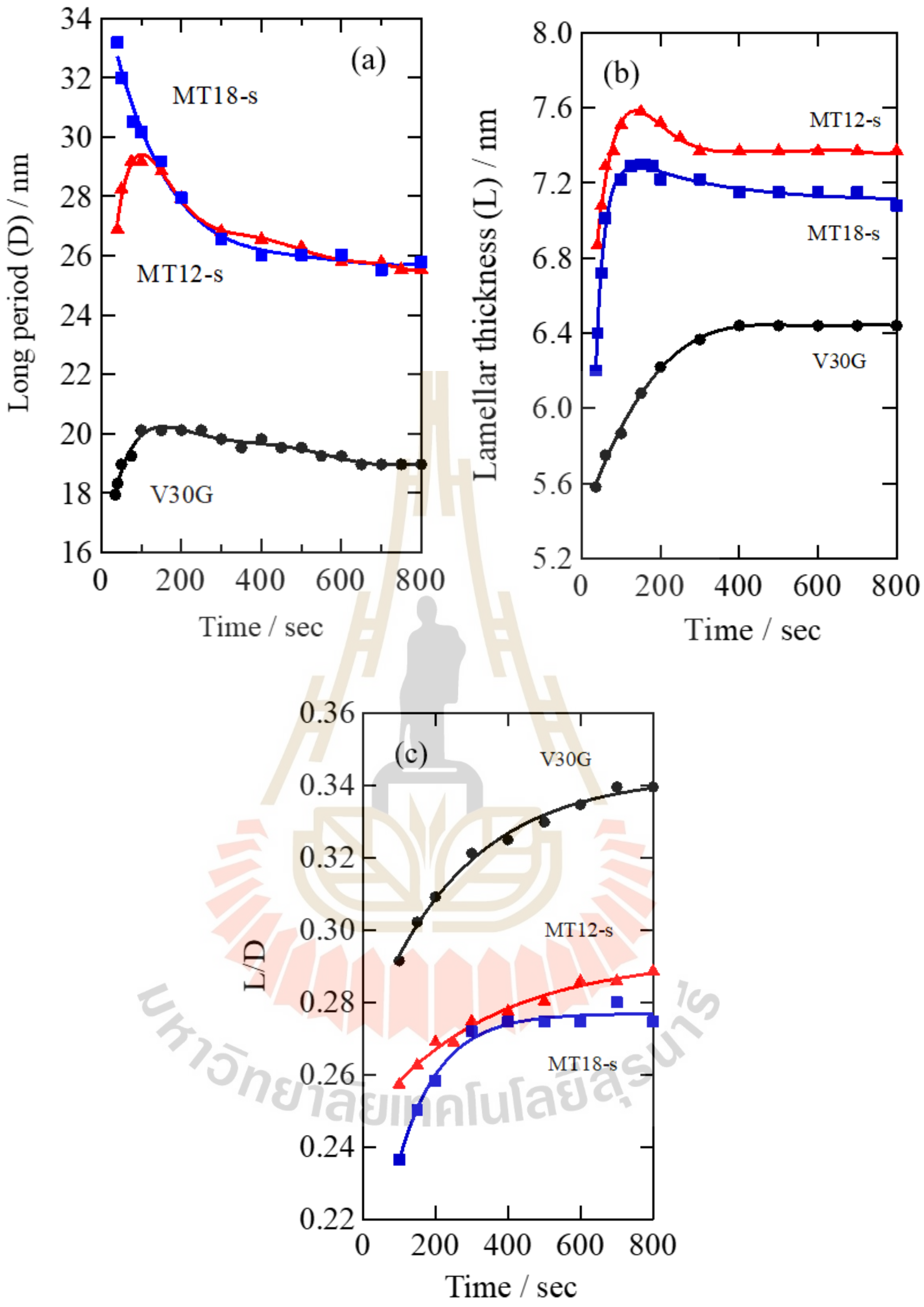

**Figure 4.16** (a) Long period (D), (b) average lamellar thickness (L), and (c) L/D ratio as a function of time during isothermal crystallization at 130°C.

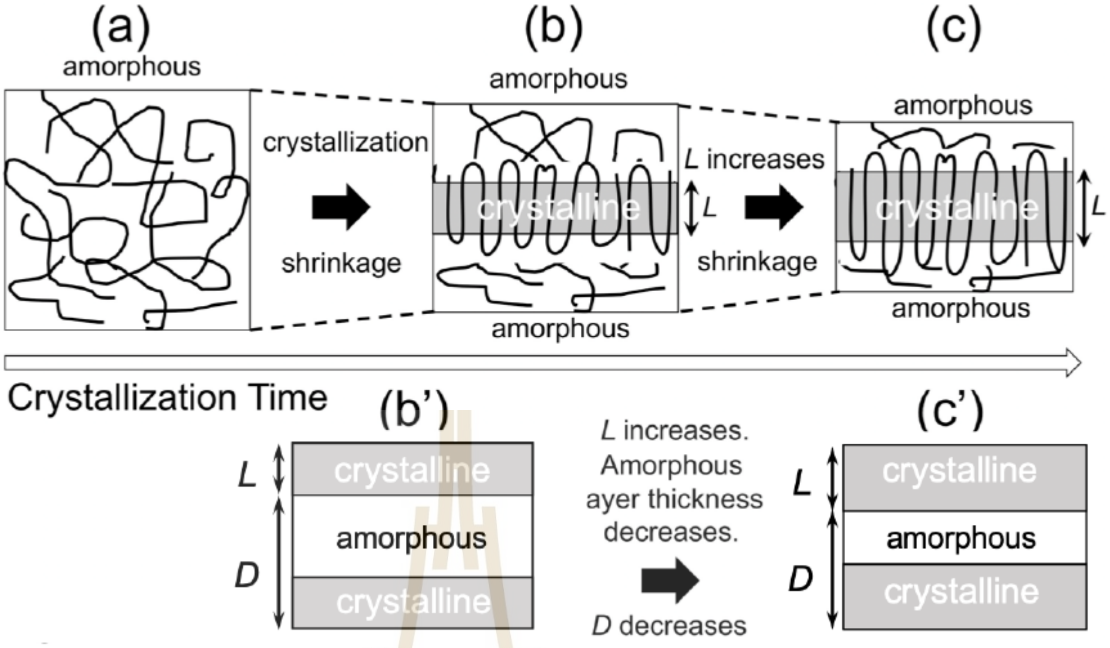

**Figure 4.17** Schematic diagram of the morphological transformation upon crystallization (a) the amorphous state before melt crystallization, (b) the early stage of crystallization and (c) lamellar thickening in the subsequent stage of the crystallization. (Pandey, 2019).

### 4.1.6 Wide angle X-ray diffraction (WAXD)

The temporal changes in the one-dimensional WAXD (1d-WAXD) profiles were measured in the isothermal crystallization process at 130°C after quenching from the melt at 200°C. Figure 4.18 shows WAXD profiles for V30G, MT12-s and MT18-s samples as a function of time. In the early stage up to 40 s, the 1d-WAXD profiles show only small crystalline peaks. As time proceeded, the intensity of amorphous halo is decreased and the crystalline peaks appeared clearer. Generally, there are three polymorphic forms for *i*PP: α (monoclinic), β (pseudo hexagonal) and γ (orthorhombic), with α-form being the most stable structure. Monoclinic α crystals are the unique polymorph in homopolymer. The peak of monoclinic α forms were detected in all PP samples whereas the orthorhombic γ forms were seen only for MT12-s and MT18-s. The strong diffraction peaks located at $q$ of 9.2, 10.8, and 12.0 nm$^{-1}$ correspond to α1 (110), α2 (040), α3 (130) and α4 (111), (131) planes, respectively, while the diffraction peak located at $q$ = 12.9 nm$^{-1}$ belongs to the γ (117) plane. In addition, it is also apparent that the crystal formation for PP with 1-butene defects is also faster than the linear PP. The relative content of the γ form, $K_\gamma$ can be calculated according to the Turner-Jones and Cobbold equation (Wang, 2005):

$$K_\gamma = \frac{h_\gamma}{h_\gamma+(h_{\alpha1}+h_{\alpha2}+h_{\alpha3})} \tag{4.11}$$

where $h_{\alpha1}, h_{\alpha2}$ and $h_{\alpha3}$ are the intensities or peak area of the α-form and $h_\gamma$ is the intensity of the γ-form. Correspondingly, the relative intensity of the three α peaks can be calculated as:

$$K_{\alpha n} = \frac{h_{\alpha n}}{h_\gamma+(h_{\alpha1}+h_{\alpha2}+h_{\alpha3})} \text{ (n = 1,2,3)} \tag{4.12}$$

The results are listed in Table 4.4. The value of $K_\gamma$ for MT12-s and MT18-s are 0.03 and 0.05, respectively, indicating that the presence of 1-butene monomer significantly favors the formation of γ crystallites (Hosier, 2003). Moreover, the relative intensities of the α2 and γ peak are also influenced by 1-butene defects. With increasing the content of 1-butene, the relative intensity of γ (117) planes increased whereas the α2 (040) planes decreased. The orientation of the plane corresponding to the increase that is normal toward the compression axis, in which the planes themselves tend to align parallel to the direction of flow. The reduction of peak intensity indicates that the corresponding plane rotated so that they aligned parallel to the compressive axis (Xu, 2005). Hence, with increasing the content of 1-butene, the (117) planes oriented preferentially parallel to the sample surface, while the (040) planes rotated with a tendency to be perpendicular to the sample surface. For WAXD profiles, it is indicated that the unit cell of PP may be changed for the reason that 1-butene units may be incorporated into poly(propylene) unit cell. It is noted that the polybutene crystal has similar unit cell as polypropylene.

For further investigation, an accurate determination requires the knowledge of the corresponding amorphous component at a particular composition. The degree of crystallinity can be calculated by taking different amorphous areas subtracted from the real profile at the specific content in the comonomers. The decomposition in the characteristic reflection allows quantification of each polymorph.

The time evolution of the degree of crystallinity can be evaluated using the percentage of the ratio between peak areas derived from the crystalline and the amorphous portion from Eq. (3.5). The peak decomposition was directed and the degree of crystallinity ($\phi_{WAXD}$) was evaluated and plotted as a function of time in Figure 4.19. Generally, the crystallinity based on the WAXD results is not identical to that based on DSC results. The WAXD results can be less accurate because WAXD profile only covers limited *q* range. The overall shapes of apparent crystallinity are similar to those shown in Figure 4.19(b), but they have some different characteristics in details. The degree of crystallinity for all PP samples is slightly higher than that of DSC results. The effect of 1-butene is very clear for the acceleration of crystallization, but decreased degree of crystallinity.

**Table 4.4** The Intensity (peak area) and relative intensity of α and γ diffraction peaks of all PP samples.

| Samples | Intensity (peak area) | | | | Relative intensity | | | |
|---|---|---|---|---|---|---|---|---|
| | γ | α1 | α2 | α3 | $K_{\gamma}(117)$ | $K_{\alpha 1}(110)$ | $K_{\alpha 2}(040)$ | $K_{\alpha 3}(130)$ |
| V30G | 0.00 | 40.46 | 30.74 | 14.94 | 0.00 | 0.47 | 0.36 | 0.17 |
| MT12-s | 1.47 | 21.05 | 14.70 | 6.88 | 0.03 | 0.48 | 0.33 | 0.16 |
| MT18-s | 1.90 | 16.60 | 11.18 | 5.82 | 0.05 | 0.48 | 0.31 | 0.16 |

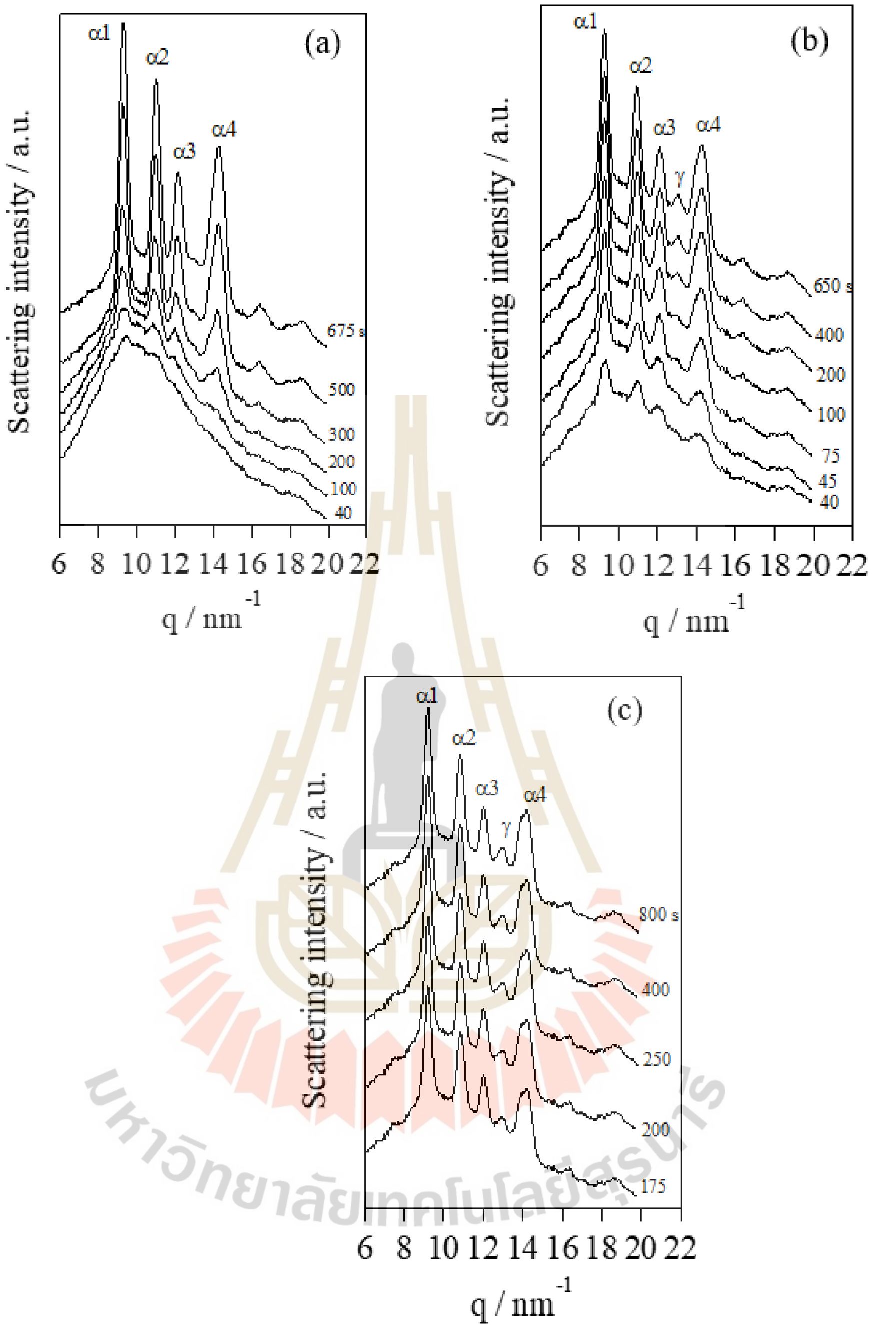

**Figure 4.18** Time-resolved wide-angle X-ray diffraction (WAXD) profiles during isothermal crystallization at 130°C of (a) V30G, (b) MT12-s and (c) MT18-s. The reflection peaks are indexed as α1 (110), α2 (040), α3 (130), α4 (111), (131) and γ (117).

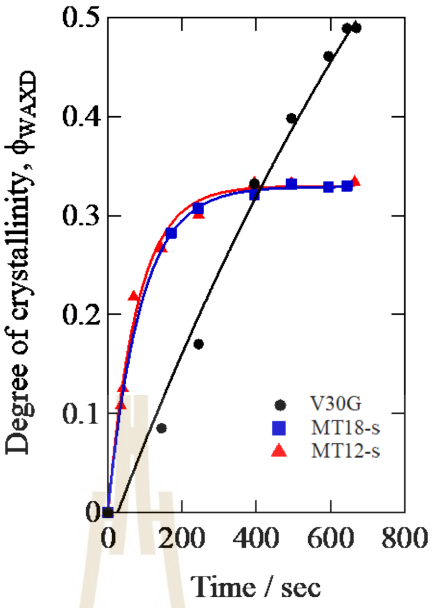

**Figure 4.19** Degree of crystallinity from WAXD as a function of time for the isothermal crystallization at 130°C.

## 4.2 Monte Carlo (MC) simulation of polymer crystallization

### 4.2.1 Monodisperse polyethylene (PE)

#### 4.2.1.1 Chain relaxation

Equilibration can be evaluated by two kinds of dynamic properties. One is the mean square displacement (MSD) of the chain center of the mass, $g_{cm}$ as

$$g_{cm}(t) =< [r_{cm}(t) - r_{cm}(0)]^2 > \tag{4.13}$$

Here, $r_{cm}(t)$ and $r_{cm}(0)$ are the coordinates of the chain center of the mass at time $t$ and $0$, respectively. The angle bracket means ensemble average. The other quantity is the orientation autocorrelation function (OACF) formulated from the end-to-end vector, $<\mathbf{R}(t).\mathbf{R}(0)>/(\mathbf{R}^2)$ and bond vector, $<\mathbf{m}(t).\mathbf{m}(0)>/<\mathbf{m}^2>$. The simulation results are presented in Figure 4.20. The equilibration as judged by MSD greater than the mean square radius of gyration, $< R_g^2 >$, is seen at the late stage (> 2.7 million MCS). In addition, the reorientation of the end-to-end vector and the bond vector fall below 1/e (the horizontal dash line) at 0.08 and 0.7 million MCS, respectively. The end-to-end vector relaxation is slower than the bond vector in the early state, but these two curves get closer to each other and are almost parallel at simulation time over 13 million MCS. In this respect, simulation up to 20 million MCS was enough for data analysis for other properties. The systems were completely equilibrated as judged by the behavior of the MSD and OCAF for bond vector which is good enough to monitor the crystallization process.

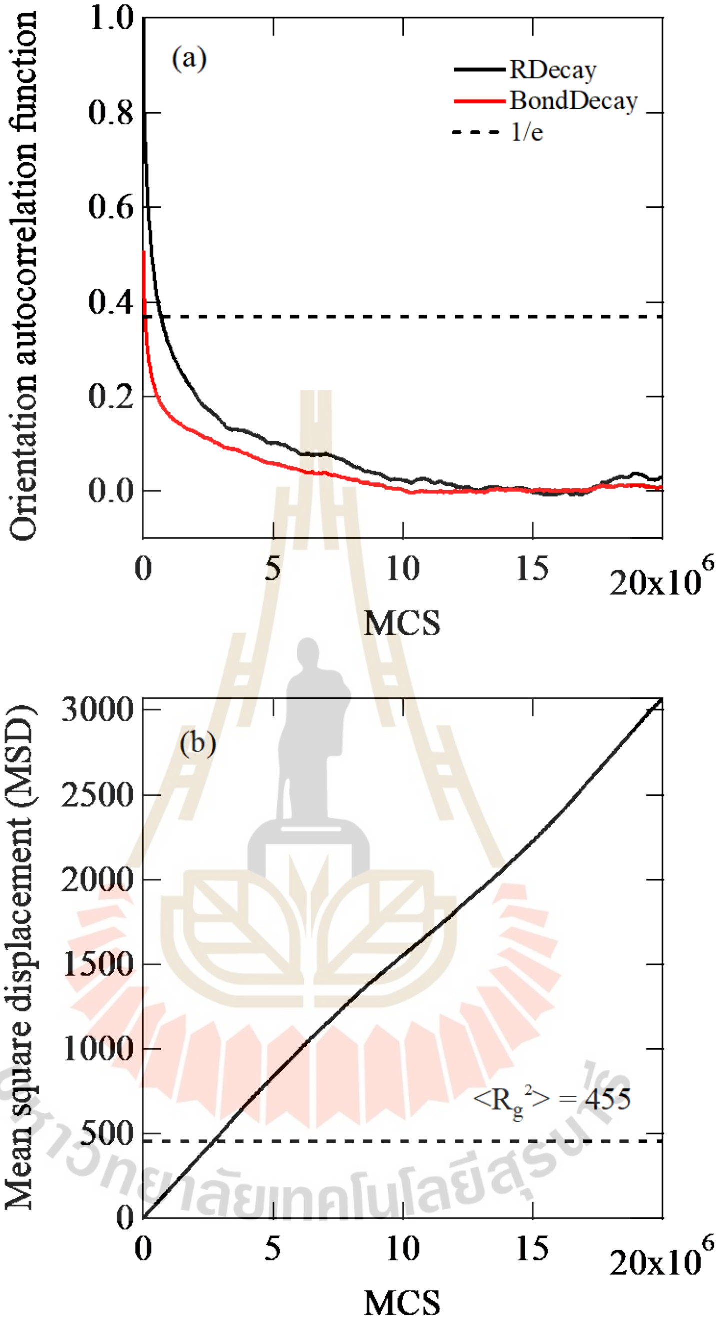

**Figure 4.20** (a) OCAF as function of MCS and (b) the MSD of homopolymer PE. Horizontal dashed line in MSD shows the mean square radius of gyration at late stage.

### 4.2.1.2 Overall chain conformation

The overall chain conformation constituted the mean square radius of gyration, $< \mathrm{R}_\mathrm{g}^2 >$ (represent the overall expansion and distortion of chains) and $< R^2 > / < R_g^2 >$ (represent the stretching of chains), as shown in Figure 4.21, increase with temperatures and simulation time. The $< \mathrm{R}_\mathrm{g}^2 >$ is increased in the temperature at 350 K, indicating the crystallization occurs at the end of this temperature. This behavior is more evident in $< \mathrm{R}_\mathrm{g}^2 >$ than $< R^2 >/< R_g^2 >$. The strongest increase around 15 to 18 million MCS in temperature at 298 K and the $< R^2 >/< R_g^2 >$ ratio increases from 6 to 7.5.

Then, the components of $< \mathrm{R}_\mathrm{g}^2 >$ in the directions of x, y and z represented by $< \mathrm{R}_\mathrm{gx}^2 >$, $< \mathrm{R}_\mathrm{gy}^2 >$ and $< \mathrm{R}_\mathrm{gz}^2 >$ were investigated in a laboratory-fixed coordinate system as shown in Figure 4.22. In order to expose that the directions of the expansion of these independent parent chains are random or correlate, it can be determined after reverse mapping using Eq. (4.14).

$$\begin{bmatrix} x \\ y \\ z \end{bmatrix} = \begin{bmatrix} 1 & cos60° & cos30°\sqrt{3} \\ 0 & sin60° & sin30°\sqrt{3} \\ 0 & 0 & \sqrt{2}/\sqrt{3} \end{bmatrix} \begin{bmatrix} \bar{x} \\ \bar{y} \\ \bar{z} \end{bmatrix} \tag{4.14}$$

From Figure 4.22, polymer chains seem isotropic, with $< \mathrm{R}_\mathrm{gx}^2 > = < \mathrm{R}_\mathrm{gy}^2 > = < \mathrm{R}_\mathrm{gz}^2 >$ at the initial stage. After that there is a massive expansion of the chains on one of the axes of the laboratory-fixed coordinate system. The slightly expansion of the chains occur around 12 million MCS at 350K and these size components clearly expand after 15 million MCS at 298K. This result displays not only that the expansion of

$< R_g^2 >$ follows according to one direction, but also that all the parent chains correlate with the direction in which they are expanded.

### 4.2.1.3 Local chain conformation

The structure formation process at the local scale can be examined by the looking at the conformational change. In Figure 4.23, the time dependence of the fraction of *trans* state at all temperature at 473, 400, 350 and 298 K is presented. This figure illustrates that the *trans* fractions are increased at the beginning of the simulation. This *trans* fraction is relatively small at the beginning compared to the intermediate step where it increases dramatically. In general, the fraction of *trans* should reach 1.0 for complete crystallization *i.e.* all polymer chains are completely elongated. For our results, the fraction of *trans* reach the constant value about 0.8 indicating that polymer chains still have some *gauche* states. Interestingly, the fraction of *trans* is increased even in the duration when the global orientational order does not exist (see Figure 4.25(b)). These results imply that polymer chains have to stretched first and the orientation can take place afterward in the crystallization process.

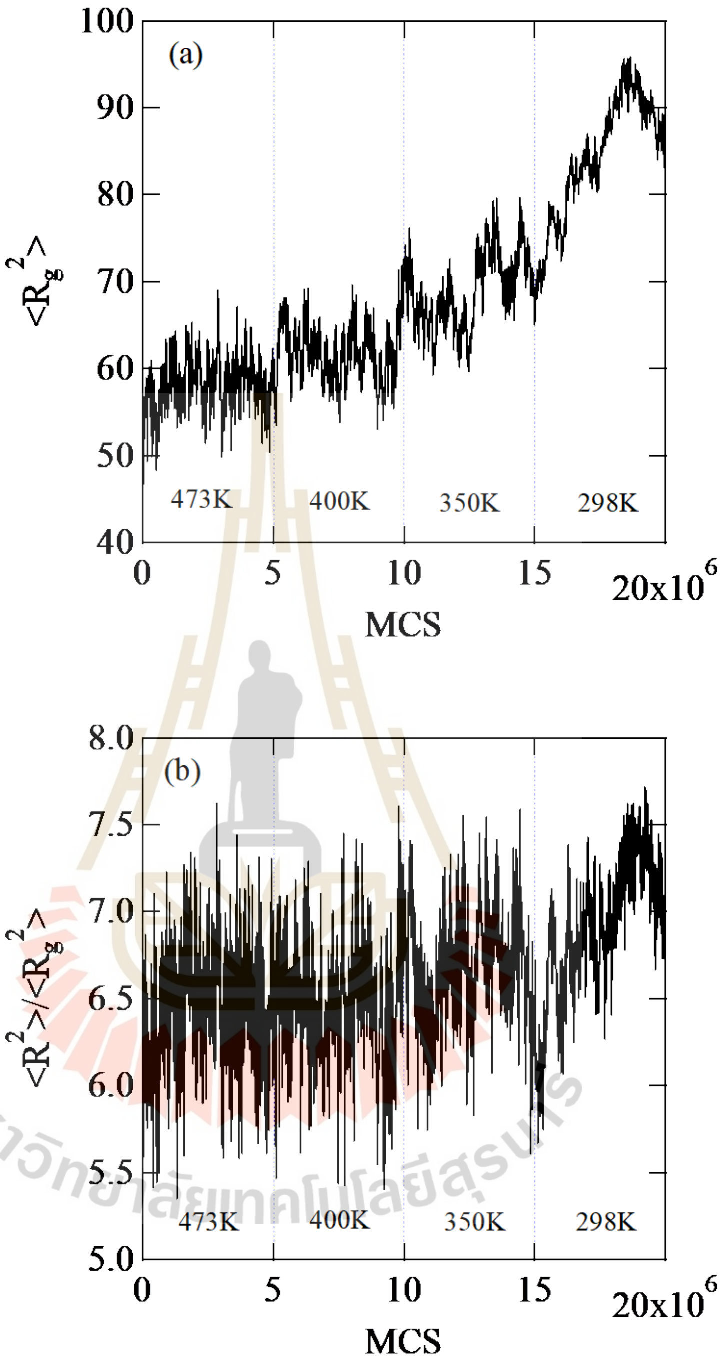

**Figure 4.21** (a) Mean square radius of gyration $< R_g^2 >$ and (b) $< R^2 >/< R_g^2 >$ as a function of MCS of homopolymer PE.

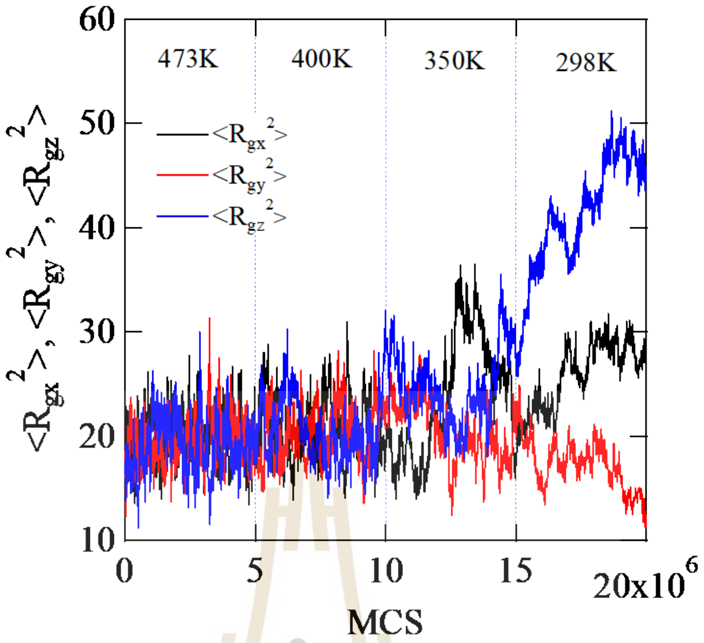

**Figure 4.22** The components of $< R_g^2 >$ on the three axes of a laboratory-fixed coordinate system.

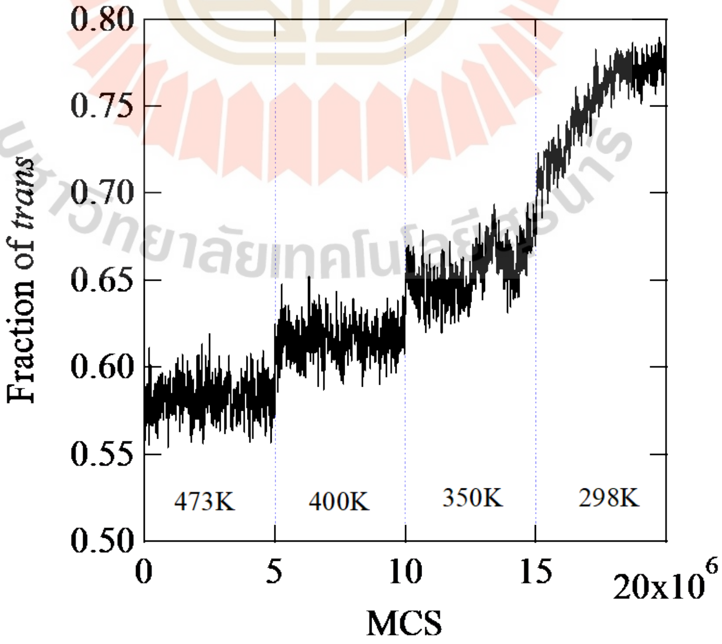

**Figure 4.23** Evolution of *trans* fraction as a function of MCS.

### 4.2.1.4 Chain ordering

Upon crystallization, PE chain has zigzag *trans* conformation and the bonds should have long distance correlation in the perfect crystalline domain. To describe the degree of chain ordering, the intramolecular, $M_1(j)$ and $M_2(j)$, and the intermolecular orientation correlation functions, $S_L$ and $S_G$ are used. $M_1(j)$ and $M_2(j)$ are defined by

$$M_1(j) =< m_i . m_{i+j} > = < \cos\theta_{i,i+j} > \quad (4.15)$$

$$M_2(j) = \frac{1}{2}\left[3 < \left(m_i . m_{i+j}\right)^2 > -1\right] = \frac{1}{2}[3 < cos^2\theta_{i,i+j} > -1] \quad (4.16)$$

Here, $\theta_{i,i+j}$ is the angle between the *i*th and the (*i*+*j*)th bond in the same chain. The bond orientation correlation functions, $M_1(j)$ and $M_2(j)$, at different interval and temperature are presented in Figure 4.24. $M_1(j)$ represents the tendency for bond alignment in the same direction which grow gradually *i.e.* from 5 to 10 bonds as the simulation proceeds. The second order, $M_2(j)$, represents the overall alignment of bonds along a common axis. From Figure 5(b), $M_2(j)$ exhibits the systematic change as the simulation proceeds and almost constant at the particular time. The development of a plateau in $M_2(j)$ expands roughly from $j = 3$ to $j = 14$. It is noted that $M_2(j)$ is not sensitive to the difference between parallel and antiparallel orientations, while $M_1(j)$ is more sensitive to this difference.

Other parameter sets are intermolecular orientation correlation functions. The local intermolecular ($S_L$) and global orientation order parameter ($S_G$) are defined as

$$\mathrm{S_L(n)} = \frac{1}{2}[3 < \cos^2\psi(\mathrm{n}) > -1] \quad (4.17)$$

$$\mathrm{S_G} = \frac{1}{2}[3 < \cos^2\psi > -1] \quad (4.18)$$

where, $\psi(n)$ in Eq. (4.17) is angle between two bonds separated in the *n*th shell. $\psi$ in Eq. (4.18) is the angle between the main axes of two chains and $S_G$ is averaged for all the pairs of chains. Figure 6(a) depicts $S_L$ at five different intervals. At the initial stage, the first shell has small values which are related to the high repulsive interaction at the first shell. $S_L$ decays to zero when $n$ increases, indicating that the intermolecular bonds have little orientation correlation. For local orientation, $S_L$ increases and never reaches zero when simulation proceeds. The largest value could be attained at $n = 1$ when all bond pairs (inter- and intramolecular) were included in the calculation of $S_L$. Figure 4.25(b) describes the evolution of $S_G$ as a function of MCS. The system displays an isotropic phase where chains are in disordered state with $S_G \approx 0$ and polymer chains become a nematic phase with $S_G$ increase to 1. At the beginning when the temperature is in the range of 473 - 400 K, $S_G$ takes a value close to zero (no global orientational order) but grow suddenly after certain duration. A sharp increase followed by slightly increase can be seen at the later stage at 350 K (the crystallization process begins). It is the signature of the first-order phase transition *i.e.* between an isotropic and a nematic phase. Compared with Figure 4.23, the chain alignment should start after polymer molecules are stretched to a certain extent.

#### 4.2.1.5 Intermolecular packing

The local intermolecular packing of the chains can be determined from the pair correlation function (PCF) which is the probability of finding a particle A at a specified distance from another particle A. These values can be obtained from Eq. (4.19).

$$g_{AA}(i) = \frac{<n_{AA}(i)>}{(10i^2+2)V_A} \tag{4.19}$$

Here, $n_{AA}$ is a number occupancy of A in the $i$th shell from another A; $V_A$ is a volume fraction of A. We ignore the beads on the same chain that are separated by 1 or 2 bonds. In order to study molecular packing, the PCFs as a function of shell number at four intervals are compared as depicted in Figure 4.26. The PCFs in close shells (2nd to 6th) increase while those in the outer shells (7th and 8th) are slightly reduced to keep the same overall occupancy during the simulation progresses. The maximum PCF appears at the third shell as a consequence of the location of the lowest interaction in Lennard-Jones potentials and the next high point is at the fifth shell. This result shows that polymer chain packed denser in the crystalline phase as expected.

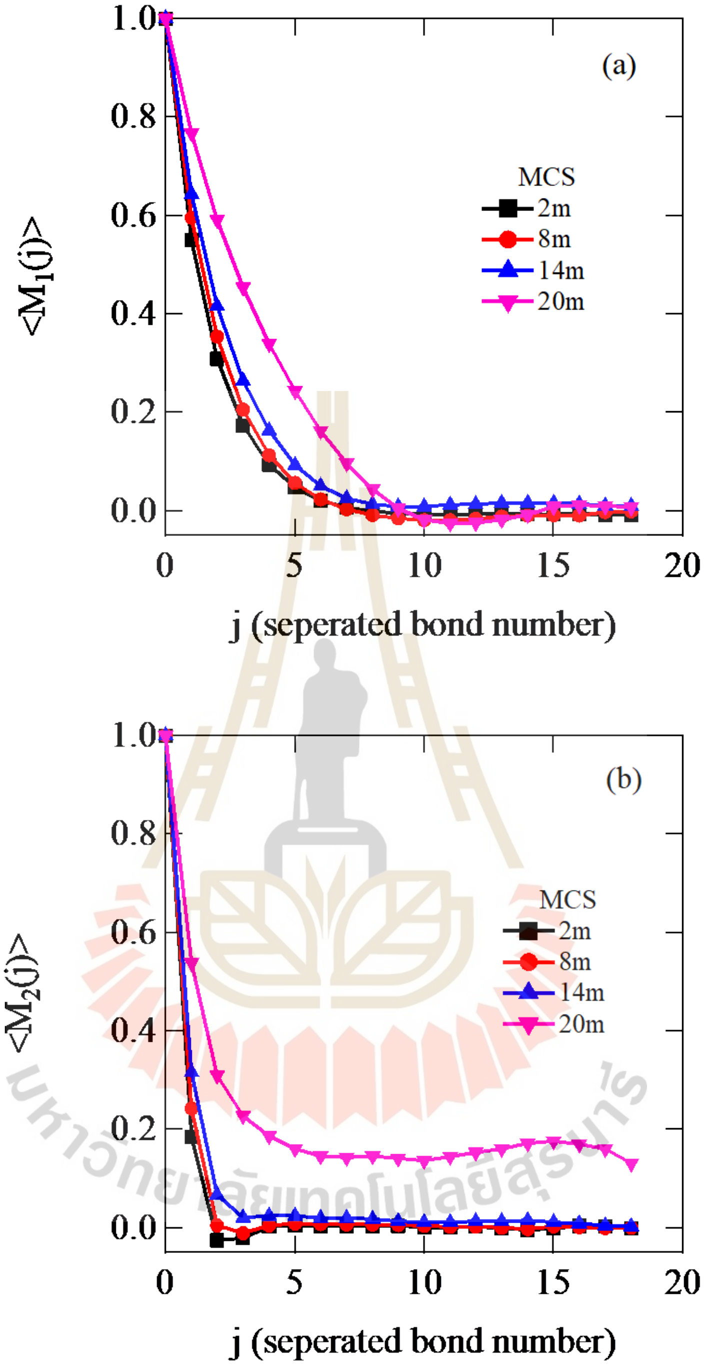

**Figure 4.24** Intramolecular bond orientation correlation functions: (a) $M_1(j)$ and (b) $M_2(j)$, both as a function of *j* of homopolymer PE.

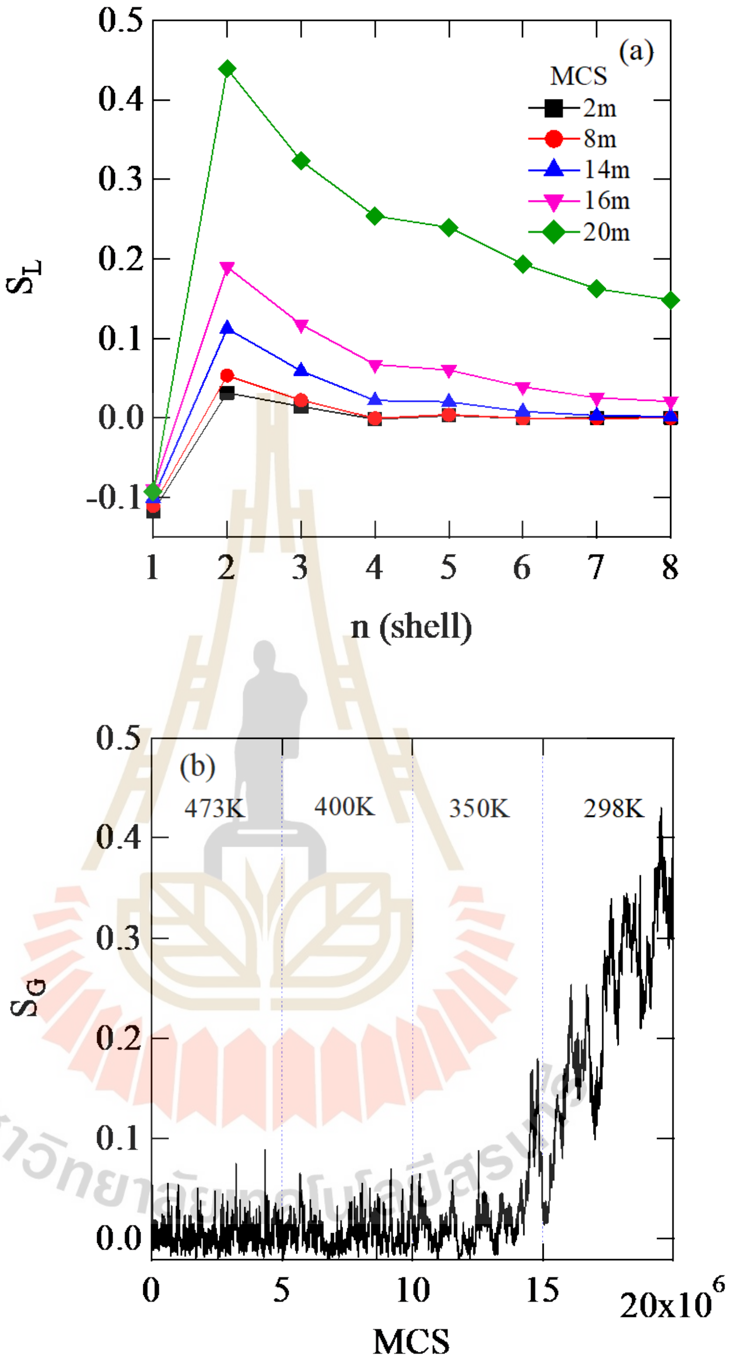

**Figure 4.25** (a) Local intermolecular bond orientation correlation function $S_L$ as a function of shell number and (b) evolution of the global orientation order parameter $S_G$.

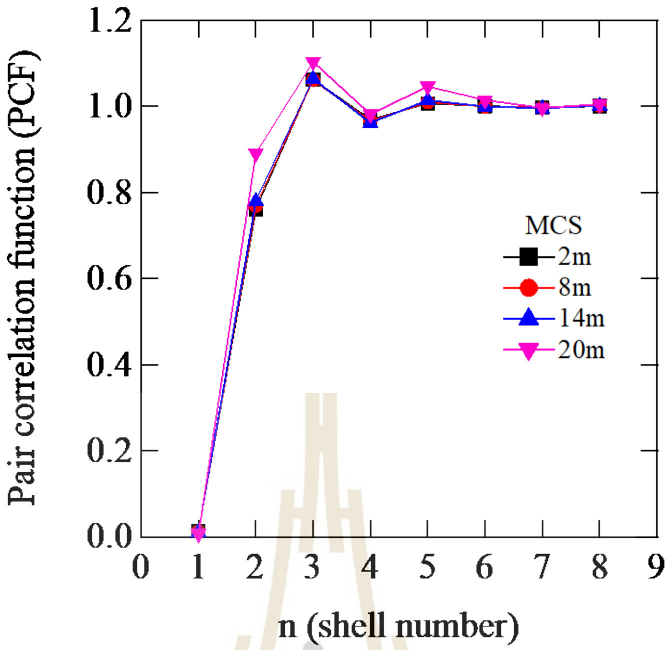

**Figure 4.26** Pair correlation functions as a function of shell number.

### 4.2.2 Bidispersed PE

Simulation of PE with different chain length are compared between 4 systems; the systems of monodisperse cases used as the reference *i.e.* $C_{20}H_{42}$ ("*Short*") and $C_{40}H_{82}$ ("*Long*") and the other two systems for bimodal mixtures ($C_{20}H_{42}$ + $C_{40}H_{82}$) with two different short chain component as 10 mol% (LS10) and 50 mol% (LS50). The bimodal mixtures were investigated separately for their long (L) and short chain (S) component, denoted as LS10-L, LS10-S, LS50-L and LS50-S. In order to investigate the structure formation process, we first investigate how the conformational change takes place. From Figure 4.27, the *trans* fractions are slightly increased at the beginning of the simulation and increases sharply in the intermediate stage at 350 K. When the temperature reach 298K, the fraction of *trans* is relatively constant indicating that the crystallization is more or less completed. Our results suggest that "*Short*" system has the sharpest increase, followed by LS50-S and LS10-S at 350 K while "*Long*" and LS10-L have the least increase for *trans* fraction. The trends are almost the same at 298 K, which the short chains ("*Short*", LS50-S and LS10-S) have the highest fraction of *trans* (around 0.90) compared to *ca.*0.8 for LS50-L, "*Long*" and LS10-L. According to these data, it is possible to say that the short chain component in the mixture can induce higher fraction of *trans* conformation. This is probably because the short chains induce larger free volume thus allowing polymer chains to have more space to rearrange and allow better crystallization at the decreased temperature.

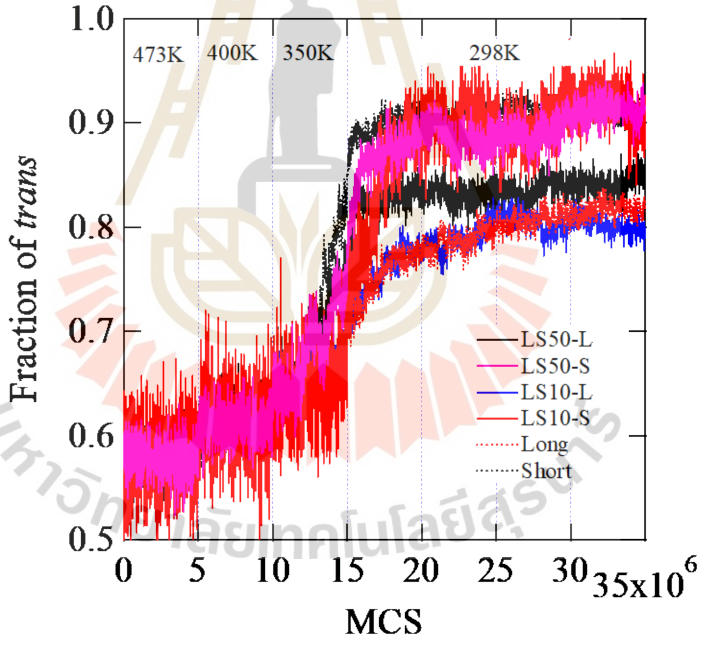

**Figure 4.27** The *trans* fraction as a function of MCS of monodisperse and bimodal PE systems.

The overall chain conformation can be studied using the definition of the mean square radius of gyration, $< R_g^2 >$.of polymer chains as the indicator for the extent of crystallization as shown in Figure 4.28. The components of $< R_g^2 >$ in the *x*, *y* and *z* direction in each PE systems are depicted in Figure 4.29. As seen in Figure 4.28, the increase of $< R_g^2 >$ starts at the temperature about 350 K, indicating that in this range of temperature can presume the crystallization. The $< R_g^2 >$ of *"Short"*, LS10-S and LS50-S systems start to increase at 350 K and then reach the constant values when the temperature drops to 298 K. On the other hand, the $< R_g^2 >$ of *"Long"*, LS10-L and LS50-L systems start to increase apparently at 298 K and reach constant values in the latter period. LS50-L has the largest overall chain expansion at 15 – 23 million MCS and $< R_g^2 >$ is close to *"Long"* at the final state. LS10-L has smaller overall chain expansion compared with long chain systems but still higher than other short chain systems. For the short chain systems, $< R_g^2 >$ in the final state is almost the same with the lowest magnitude. To compare the direction of chain expansion and stretching of the polymer chains, $< R_g^2 >$ in x, y and z directions for each PE systems were compared in Figure 4.29(a) - (f). The LS50-L, LS50-S and *"Long"* systems have the highest $< R_{gz}^2 >$, indicating that chains expand in the *z* axis direction. On the other hand, the chains in LS10-S expands well in the *y* axis while the *"Short"* system better expand in the *x* axis.

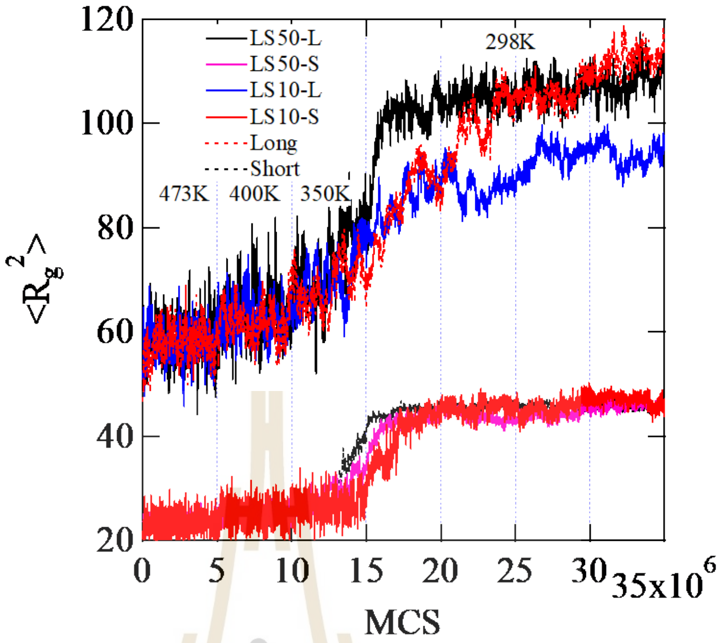

**Figure 4.28** Mean square radius of gyration, $< R_g^2 >$ of MCS of monodisperse and bimodal PE systems.

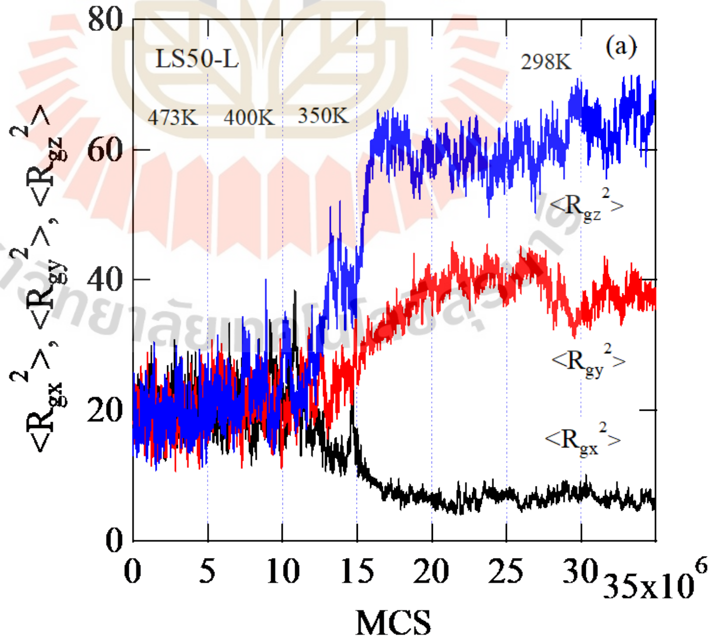

**Figure 4.29** The components of $< R_g^2 >$ along the three axes of a laboratory-fixed Cartesian coordinate system as a function of MCS of PE mixture systems.

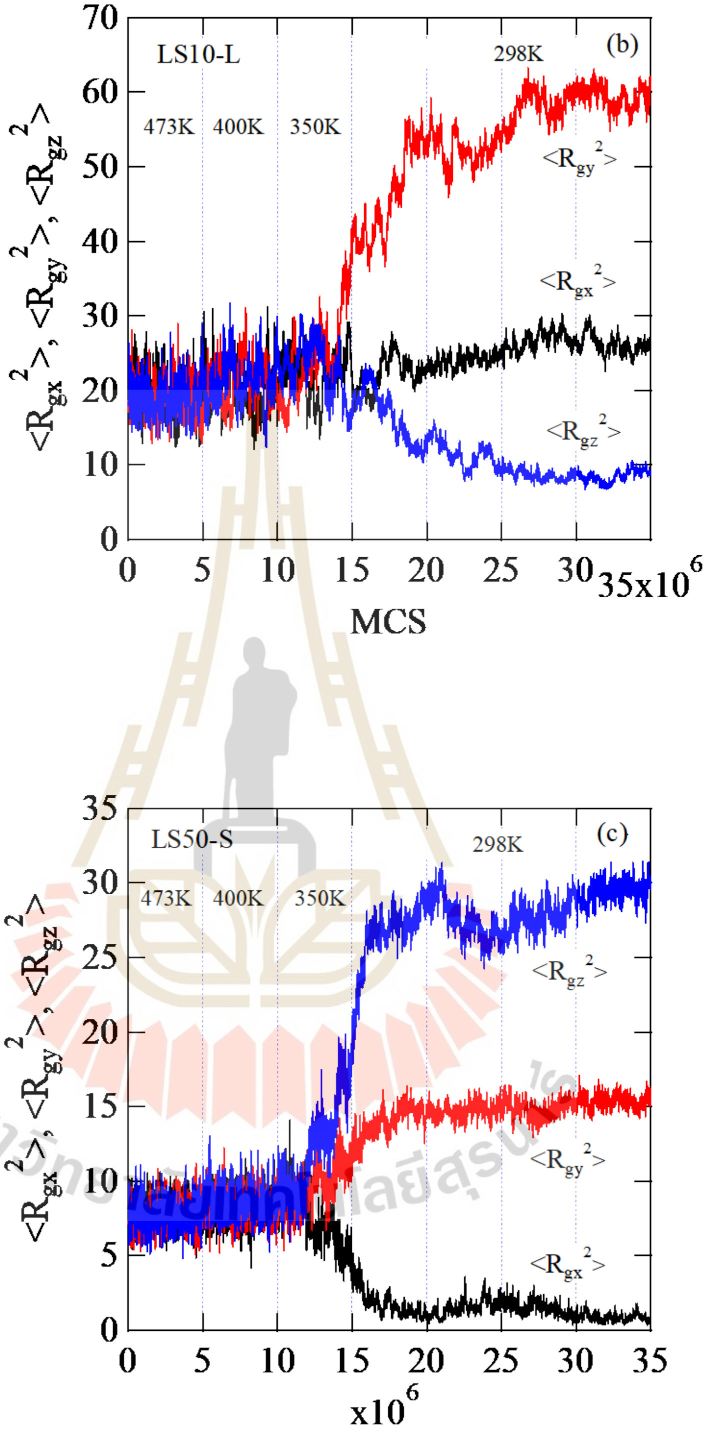

**Figure 4.29** (Continued) The components of $< R_g^2 >$ along the three axes of a laboratory-fixed Cartesian coordinate system as a function of MCS of PE mixture systems.

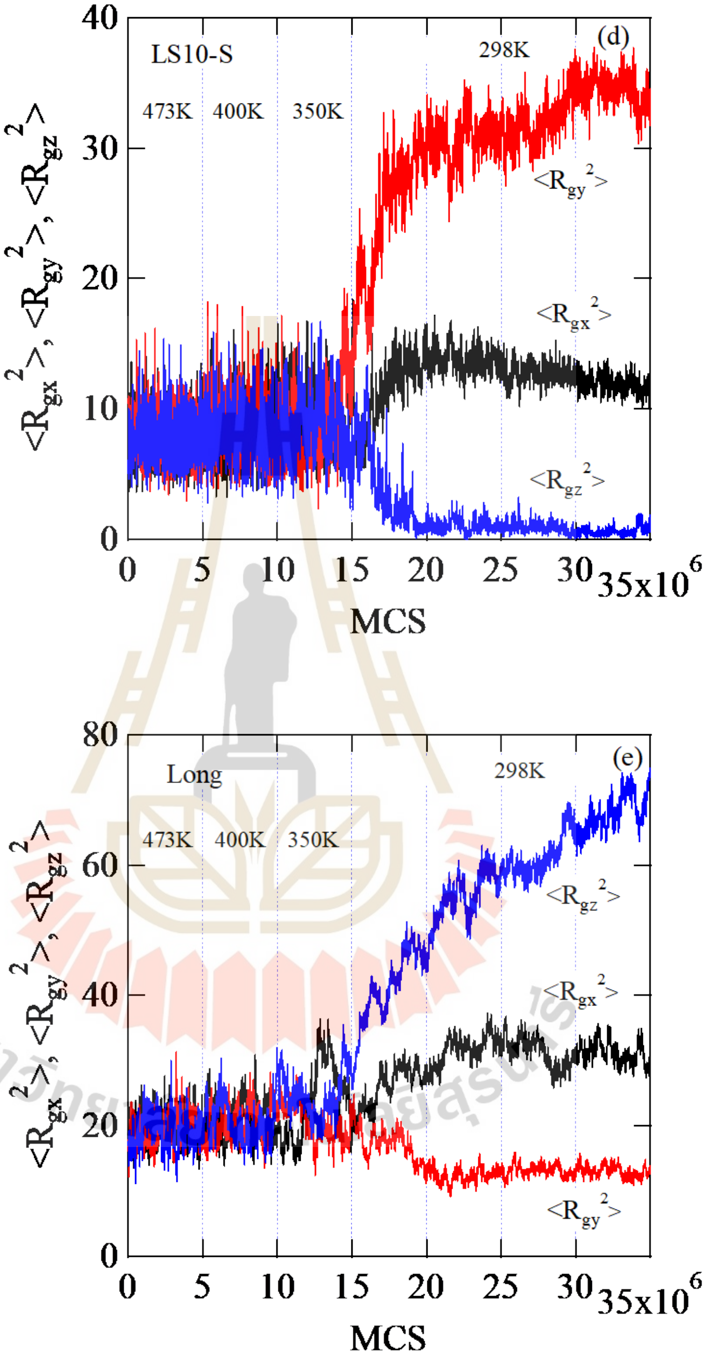

**Figure 4.29** (Continued) The components of $< R_g^2 >$ along the three axes of a laboratory-fixed Cartesian coordinate system as a function of MCS of PE mixture systems.

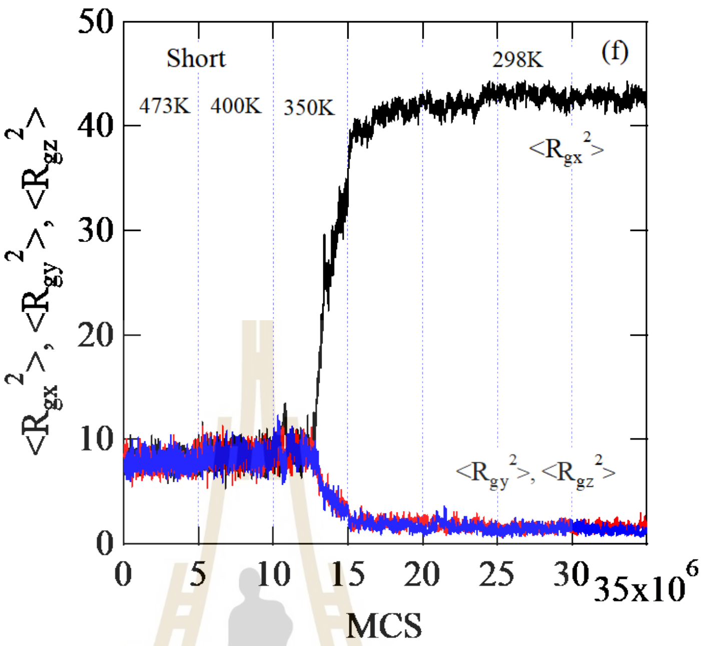

**Figure 4.29** (Continued) The components of $< R_g^2 >$ along the three axes of a laboratory-fixed Cartesian coordinate system as a function of MCS of PE mixture systems.

To describe the degree of chain ordering, the intramolecular bond orientation correlation functions, $M_2(j)$ and global intermolecular orientation correlation functions, $S_G$ were calculated both at the melted state (473 K) and crystallization temperature (298 K) for comparison as shown in Figures 4.30 and 4.31, respectively. From the definition of bond orientation correlation functions, $M_2(j) = 1$ is the case when the angle between $i$ and $i+j$ bonds equal to 0 or these two bonds are parallel. As $j$ increases, $M_2$ is decreased from 1, meaning that bond $i$ and $i+j$ become more disordered orientation when two bonds are far apart.

From Figure 4.30, $M_2(j)$ for all systems in the melted state (473 K) are more or less the same while $M_2(j)$ in each systems are clearly different at crystallization temperature (298 K). The magnitudes of $M_2(j)$ for short chain systems are higher than that of long chain systems, indicating that the short chain components should promote the order orientation. This argument can be confirmed by the results of LS50-S that has more order orientation than LS10-S. Based on these data, the long chain component exhibit different arrangements compared to short chains depending on the molar ratio of short/long chain. In general, PE mixtures with more fraction of short chains express higher anisotropic orientation.

For the ordering at the intermolecular level, as seen from Figure 4.31, $S_G$ increases sharply at the late stage at 350 K for *"Short"*, LS50-L and LS50-S while $S_G$ for the other three systems increase sharply at early state of 298 K. In the final state, $S_G$ of the LS10-S, LS50-S and LS50-L reach 0.98, 0.88 and 0.88, respectively, signifying that these systems have nematic phase with high order of chain arrangement. The *"Short"* system has larger $S_G$ compared to *"Long"* system in the early state of 298 K, but $S_G$ of both systems are almost the same at the end (*ca.* 0.77). These results suggest that both short and long chains have the similar arrangement capacity, but the results differ significantly when the short and long chains are mixed. The isotropic-nematic transition is clearly seen for LS50-L and LS50-S. On the other hand, LS10-S is completely nematic phase and LS10-L exhibits the weakest transition. The reason for these findings is related to the phase separation between short and long chain components.

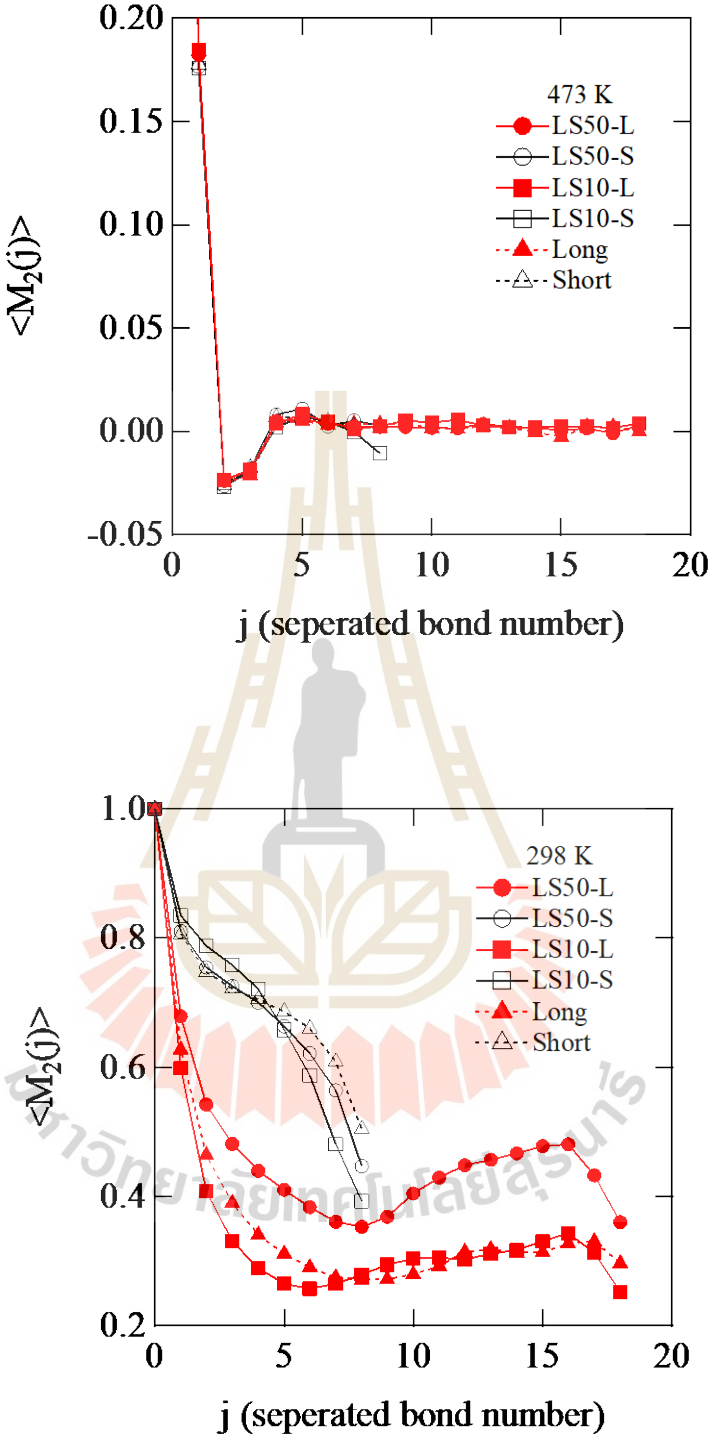

**Figure 4.30** Intramolecular bond orientation correlation functions, *$M_2(j)$* as a function of *$j$* within the same chain of PE mixture systems.

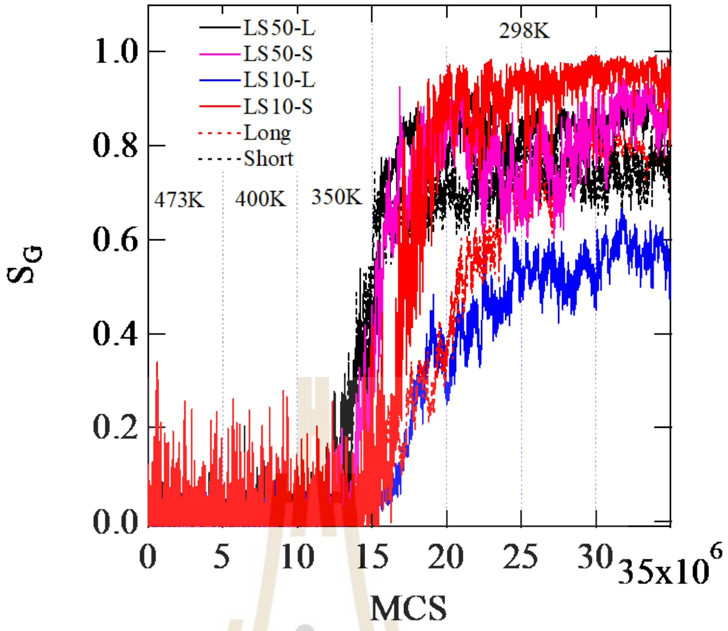

**Figure 4.31** Global orientation order parameter, $S_G$ as a function of MCS of PE mixture systems.

The final property used to monitor crystallization is the intermolecular pair correlation functions (PCF), which is related to intermolecular packing. The PCF as a function of shell number for all systems is presented in Figure 4.32. The LS10-S in the melted (473 K) and crystalline state (298 K) can be differentiated clearly in the third shell. Chains in LS50 pack better than those LS10 in the melted state (473 K). At the crystallization temperature (298 K), the short chain systems pack denser than the long chain systems. LS10-S has the highest PCF and the two systems with short chain component exhibit better intermolecular packing in the second to sixth shell. This is because short chains have more free volume due to larger amount of chain ends and thus can better arrange in an order packing.

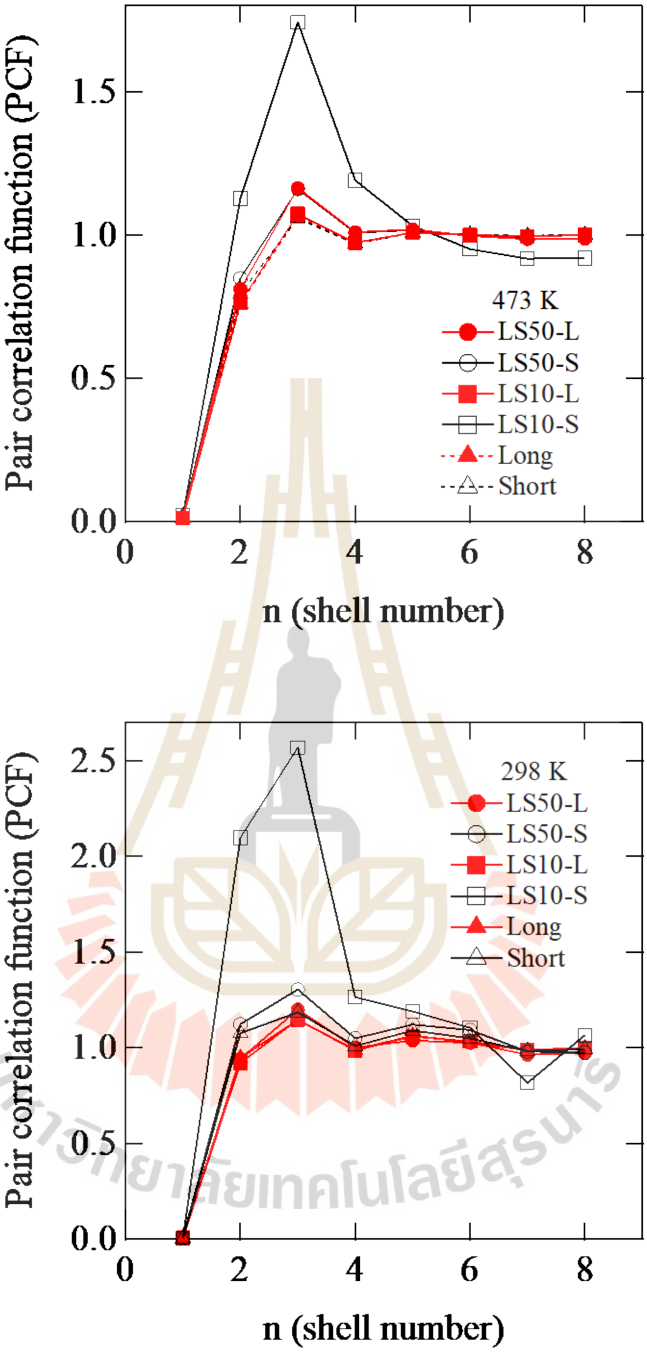

**Figure 4.32** Pair correlation function as a function of shell number of PE mixture systems.

### 4.2.3 Isotactic polypropylene (*i*PP) with few stereo-irregular defects

Simulation of *i*PP with few stereo-irregular (racemic *diads*) defects was performed for the system composed of 8 independent coarse-grained *i*PP chains with 50 monomer beads in the periodic box with the dimension of $15 \times 15 \times 15$ lattice units. The bead occupancy of 11.85% $(100 \times 50 \times 8/15^3)$ produces an equivalent density to 0.7503 g/cm$^3$, comparable with the density of *i*PP at 473 K (Orwoll, 1996). PP chains were simulated with the Metropolis Monte Carlo method with two parts of Hamiltonian. First, the intra-chain interaction is derived from the Rotational Isomeric State (RIS) model for PP. The second part is intermolecular interaction derived from the discrete version of a continuous LJ potential energy function with parameters $\varepsilon/k$ = 237.1 K and $\sigma$ = 5.118 Å, which describes the interaction of propane pair (Reid, 1987). The discretized energies for the first three shells are listed in Table 4.5. In this work, there are four systems of iPP with different number of racemic defects = 0, 1, 4, 6 beads (equivalent to 0%, 2%, 8%, 12% by mol) placed at the specified position, as shown in Figure 4.33.

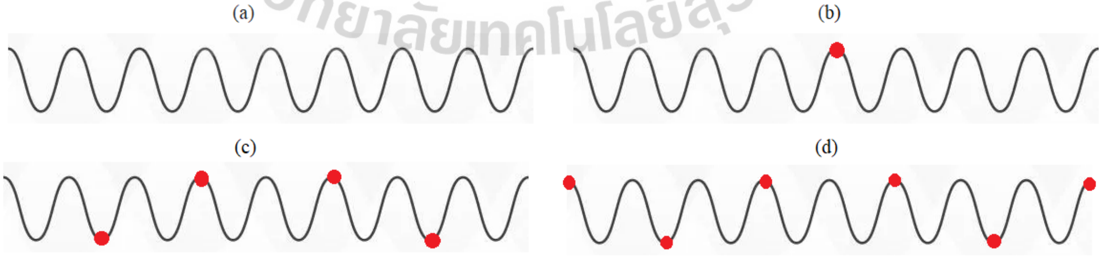

**Figure 4.33** Model of isotactic polypropylene with racemic defects for (a) 0 bead, (b) 1 bead at the 25th bead, (c) 4 beads at 10th, 20th, 30th, 40th and (d) 6 beads at 1st, 10th, 20th, 30th, 40th, 50th positions.

**Table 4.5** Discrete interaction energies (kJ/mol) for the first three shells.

| T (K) | First shell | Second shell | Third shell |
|---|---|---|---|
| 298 | 18.181 | 1.594 | -1.168 |
| 350 | 20.836 | 2.054 | -1.141 |
| 400 | 23.318 | 2.642 | -1.118 |
| 473 | 26.837 | 3.068 | -1.089 |

#### 4.2.3.1 Equilibration and Dynamics

Equilibration of polymer systems at each temperature was evaluated using the orientation autocorrelation functions (OACF) formulated from the end-to-end vector, <**R**(*t*).**R**(*0*)> and bond vector, <**m**(t).**m**(0)>. The decay of <**R**(*t*).**R**(*0*)> and <**m**(t).**m**(0)> are depicted in Figures 4.34 and 4.35, respectively. <**R**(*t*).**R**(*0*)> can decay below 1/*e* = 0.37 criteria at temperature below 400 K. For bond dynamics, <**m**(t).**m**(0)> can decay well below 1/*e* at all studied temperatures. Apparently, <**m**(t).**m**(0)> decays more rapidly than <**R**(*t*).**R**(*0*)> at any temperature for all systems because the reorientation of a local segment should be faster than the whole chain. iPP chains with larger amount of racemic defects can be relaxed readily as both 298 K and 350 K lines decay close to 1/*e*. Therefore, there is a reasonable equilibration for the local segments but equilibration on the whole chains may be incomplete. Although the simulation cannot provide enough time for the development of mature crystals as equilibration cannot be achieved at the over-distance scale for T < 400 K, it still can capture the onset of inhomogeneity before the formation of stable crystals.

#### 4.2.3.2 Average local conformation

To evaluate the tendency of *i*PP crystallization, the amount of helix conformation in the crystallize phase was determined. The $3_1$ helix of *i*PP has a conformation in which *gauche* (*g*) placements of the same sign alternate with *trans* (*t*) placements. The temperature dependence of one, two or three consecutive repetitions of this sequence is presented in Figure 4.36. The numerical data for the fraction of *tg*, *tgtg* and *tgtgtg* at four different temperatures are listed in Table 4.6. As expected, the *tg*, *tgtg* and *tgtgtg* fraction of *i*PP chains are increased at lower temperature and there is an increase in the tendency to prolong the *tg* sequences together. Clearly, the probability for *tg*, *tgtg* and *tgtgtg* sequence become lower when *i*PP chains contain larger amount of racemic defects. The fraction of *tgtg* and *tgtgtg* sequence are reduced by two and three times, respectively compared to *tg* content. It is apparent that racemic defect in *i*PP chains hinder the formation of $3_1$ helix and retard the crystallization of *i*PP.

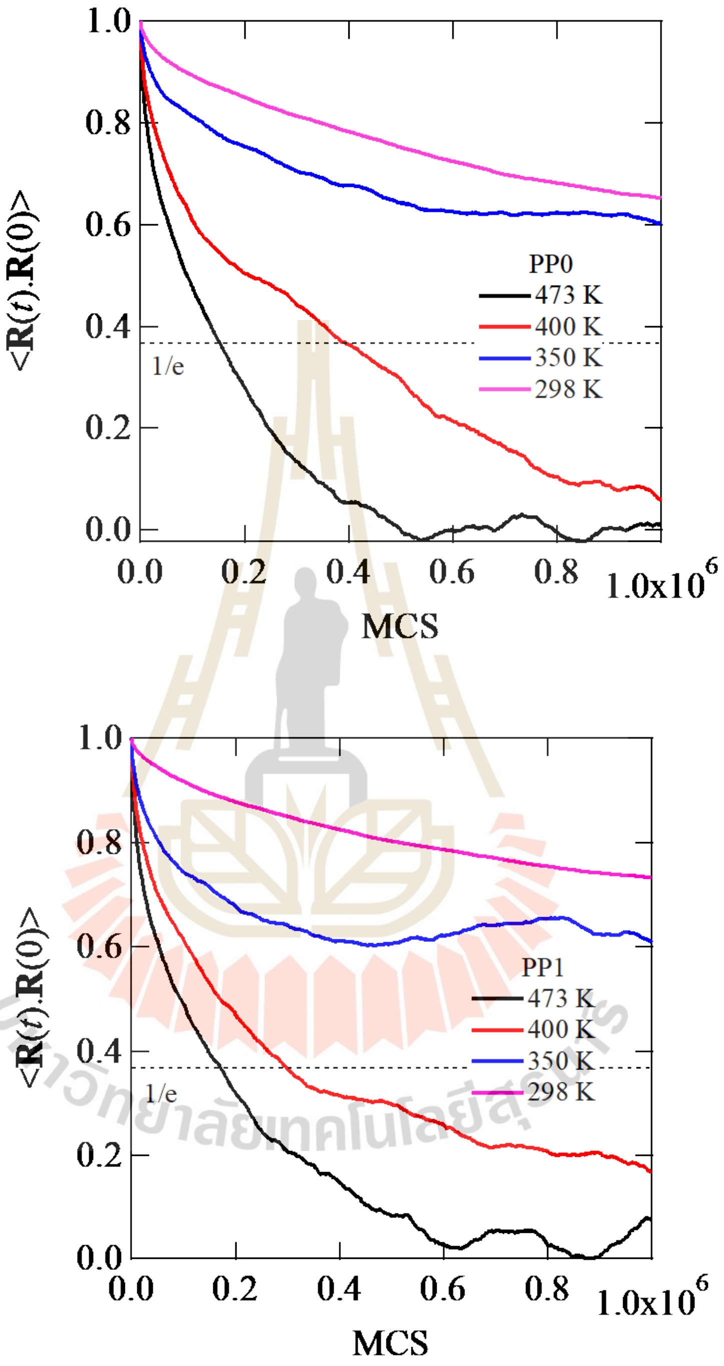

**Figure 4.34** Decay of the chain end-to-end vector orientational autocorrelation function, <**R**(*t*).**R**(*0*)> of iPP with racemic diad defect at 298, 350, 400 and 473 K. The horizontal dashed lines are 1/*e*.

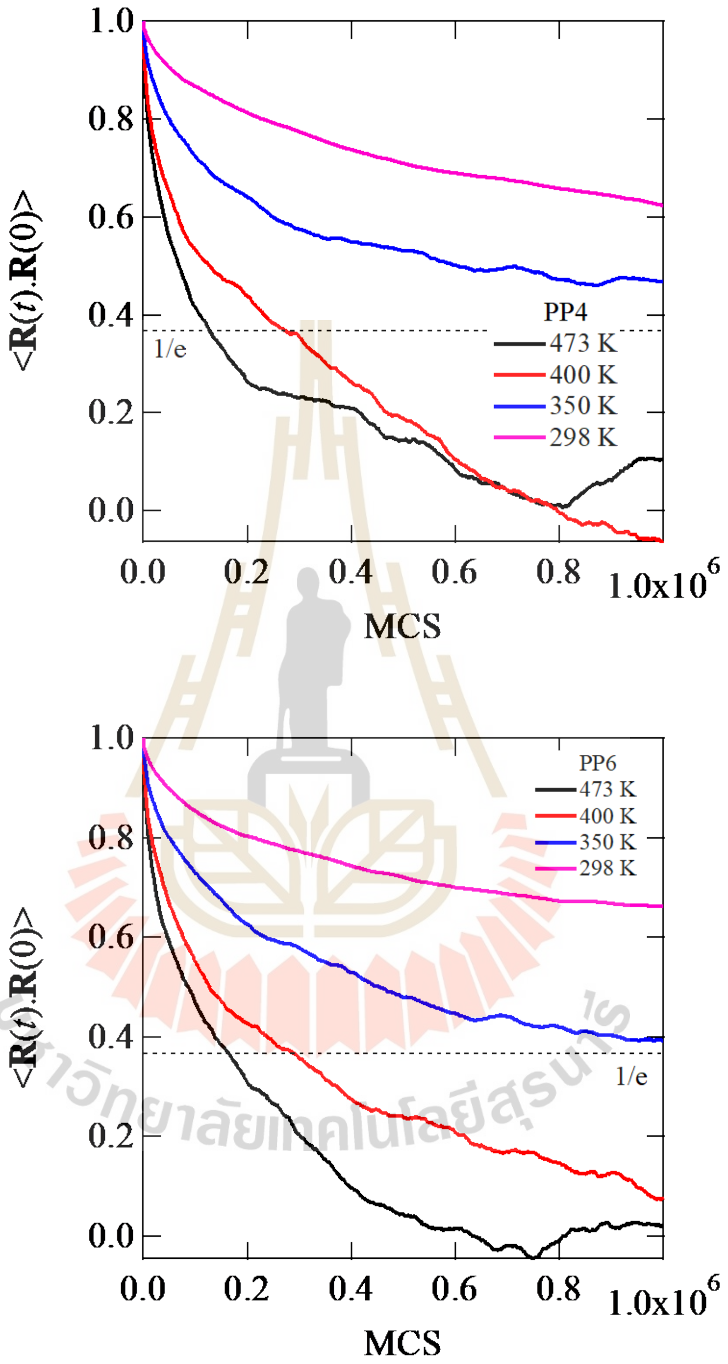

**Figure 4.34** (Continued) Decay of the chain end-to-end vector orientational autocorrelation function, <**R**(*t*).**R**(*0*)> of iPP with racemic diad defect at 298, 350, 400 and 473 K. The horizontal dashed lines are 1/*e*.

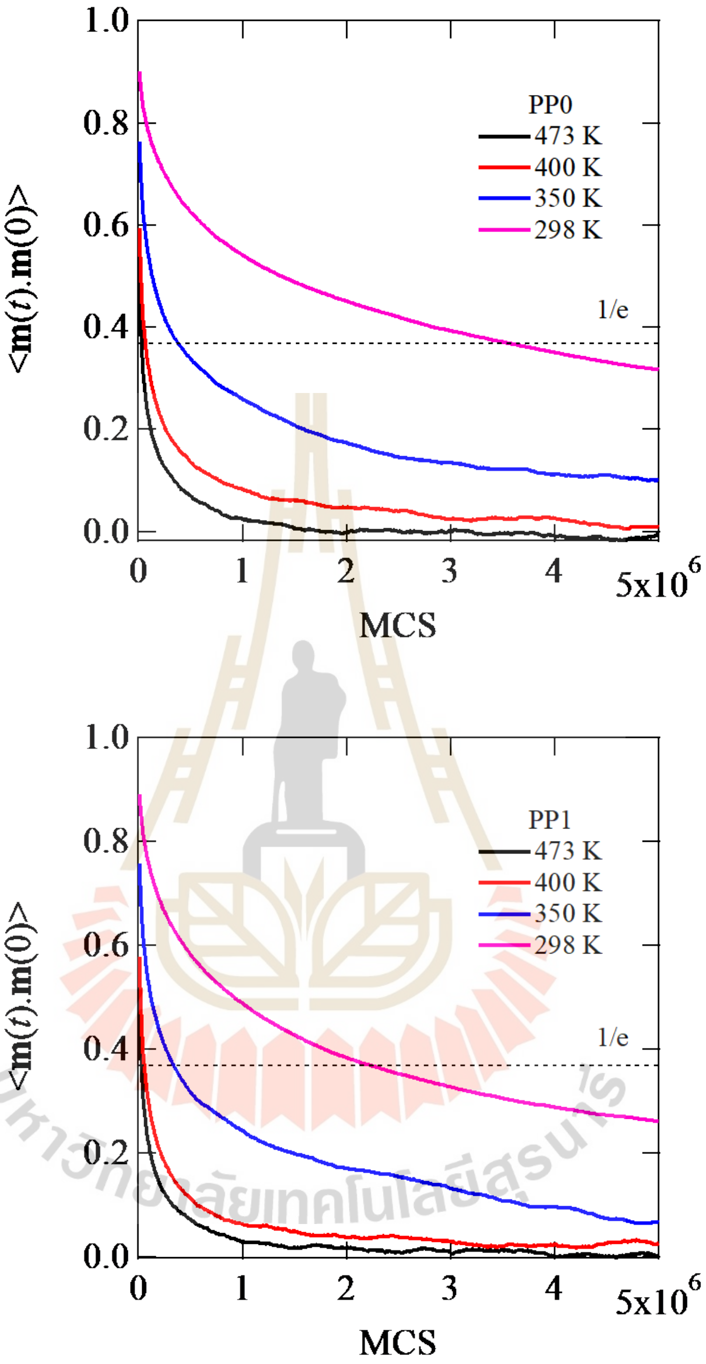

**Figure 4.35** Decay of the orientational autocorrelation function of bond vector, <**m**(t).**m**(0)> of iPP with racemic diad defect at 298, 350, 400 and 473 K. The horizontal dashed lines are 1/*e*.

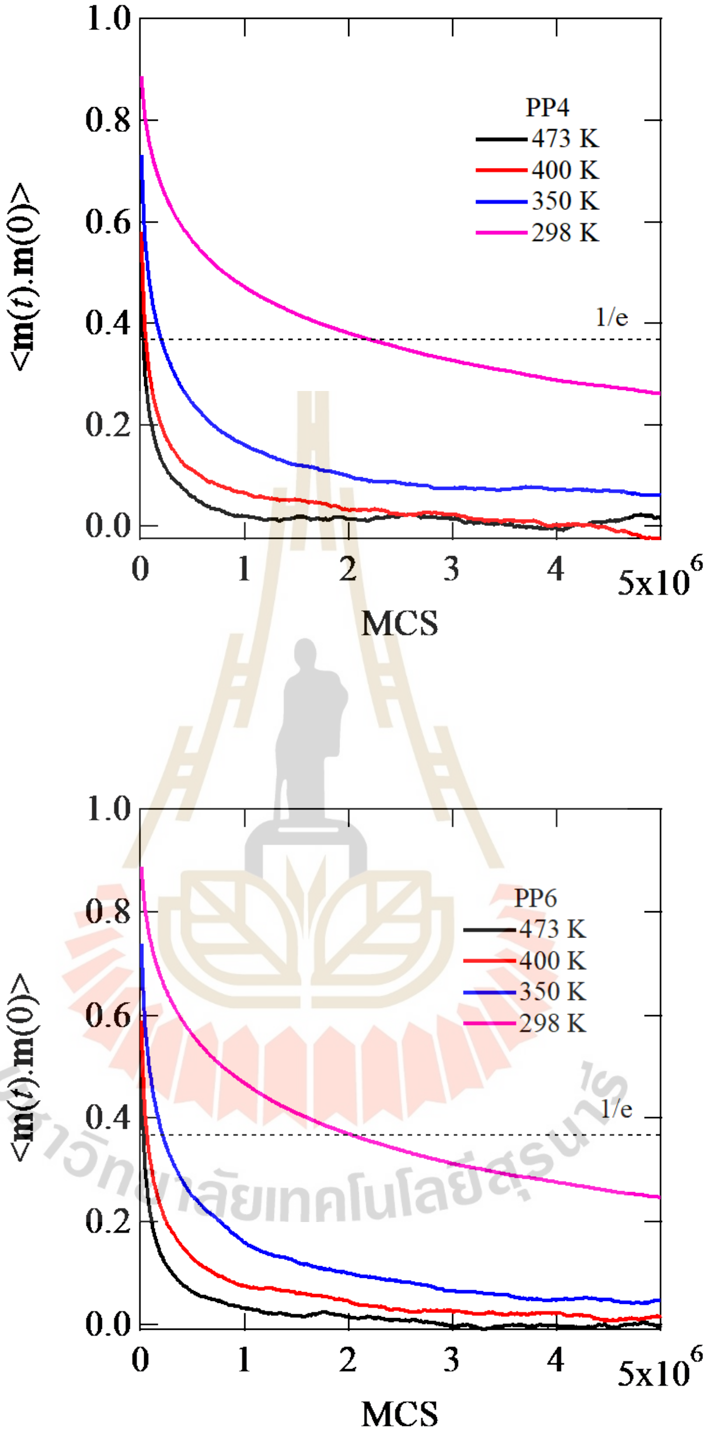

**Figure 4.35** (Continued) Decay of the orientational autocorrelation function of bond vector, <**m**(t).**m**(0)> of iPP with racemic diad defect at 298, 350, 400 and 473 K. The horizontal dashed lines are 1/*e*.

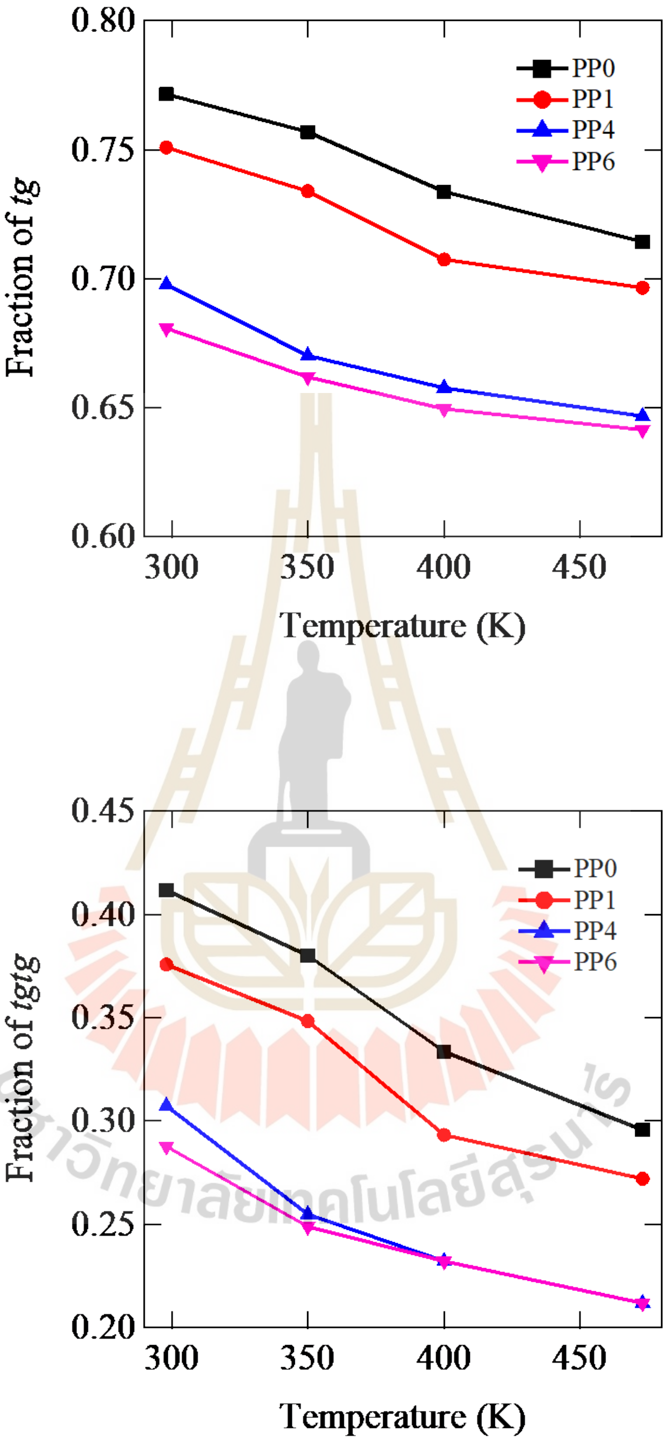

**Figure 4.36** Dependence on temperature of the populations of 2, 4 and 6 consecutive C-C bonds in helical *tg* (*gauche* states of the same sign) conformation of iPP with racemic diad defect.

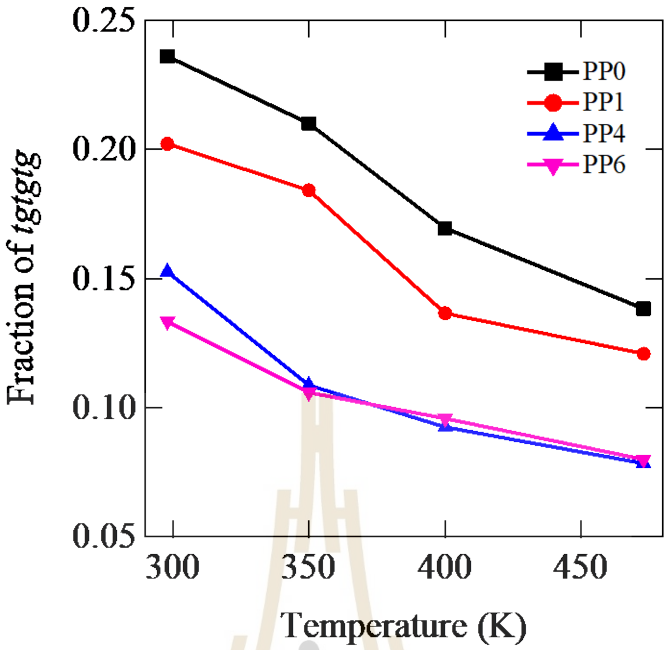

**Figure 4.36** (Continued) Dependence on temperature of the populations of 2, 4 and 6 consecutive C-C bonds in helical *tg* (*gauche* states of the same sign) conformation of iPP with racemic diad defect.

**Table 4.6** The fraction of *tg*, *tgtg* and *tgtgtg* at four different temperature of iPP with racemic diad defect.

| | Fraction | Temperature (K) | | | |
|---|---|---|---|---|---|
| | | 298 (±SD) | 350 (±SD) | 400 (±SD) | 473 (±SD) |
| PP0 | *Tg* | 0.77±0.02 | 0.76±0.02 | 0.73±0.02 | 0.71±0.02 |
| | *tgtg* | 0.41±0.03 | 0.38±0.03 | 0.33±0.03 | 0.30±0.03 |
| | *tgtgtg* | 0.24±0.03 | 0.21±0.03 | 0.17±0.03 | 0.14±0.03 |
| PP1 | *Tg* | 0.75±0.02 | 0.73±0.02 | 0.71±0.02 | 0.70±0.02 |
| | *tgtg* | 0.38±0.03 | 0.35±0.04 | 0.29±0.03 | 0.27±0.03 |
| | *tgtgtg* | 0.20±0.03 | 0.18±0.03 | 0.14±0.03 | 0.12±0.03 |
| PP4 | *Tg* | 0.70±0.02 | 0.67±0.02 | 0.66±0.02 | 0.65±0.02 |
| | *tgtg* | 0.31±0.03 | 0.25±0.02 | 0.23±0.02 | 0.21±0.02 |
| | *tgtgtg* | 0.15±0.03 | 0.11±0.02 | 0.09±0.02 | 0.08±0.02 |
| PP6 | *Tg* | 0.68±0.02 | 0.66±0.02 | 0.65±0.02 | 0.64±0.02 |
| | *tgtg* | 0.29±0.03 | 0.25±0.03 | 0.23±0.02 | 0.21±0.02 |
| | *tgtgtg* | 0.13±0.02 | 0.11±0.02 | 0.10±0.02 | 0.08±0.02 |

### 4.2.3.3 Chain ordering

To study the chain ordering, the intramolecular bond correlation functions, $M_2(j)$ and local intermolecular bond orientation correlation functions, $S_L$ at the melt (473 K) and crystallization temperature (298 K) are plotted and compared in Figures 4.37 and 4.38, respectively. iPP chains crystallize as the $3_1$ helix and this conformation can be observed from the bond correlation $M_2(j)$ especially at $j = 3$. At 473 K, $M_2(j)$ for all PP systems are not much different ($M_2(j) = 0.01 – 0.05$ at $j = 3$) but their magnitudes can be differentiated with the tendency as PP0 > PP1 > PP6 > PP4. The trend is also similar to results at 298 K, but the difference is more obvious. At 298 K, PP0 has the highest $M_2(j)$ about 0.19, PP1 and PP4 in the range of 0.11, while PP6 has the lowest value (almost 0.00). These results suggest that *i*PP with higher amount of racemic defects have more chain disordering and interrupt $3_1$ helix resulting in more difficult for iPP chains to crystallize.

The local intermolecular bond orientation correlation functions, $S_L$, defined by Eq. (4.17) is -0.5, 1.0 and 0.0 when the angle between two bonds is 90° (perpendicular), 0°(parallel) and randomly oriented, respectively. From Figure 4.38, $S_L$ values are in the range of -0.4 to 0.1 at both 473 K and 298 K and these mean that *i*PP chains tend to have local intermolecular bond arrangement in perpendicular direction as a result of helix conformation. The values of $S_L$ in all *i*PP systems are more or less the same at 473 K, but noticeably different at 298 K. When the temperature is lower and the crystallization tend to occur at 298 K, all PP systems can have different $S_L$ values especially at the second and third shells. As expected, increasing amount of racemic defect, less intermolecular bond orientation correlation can be observed, especially at the crystallization temperature.

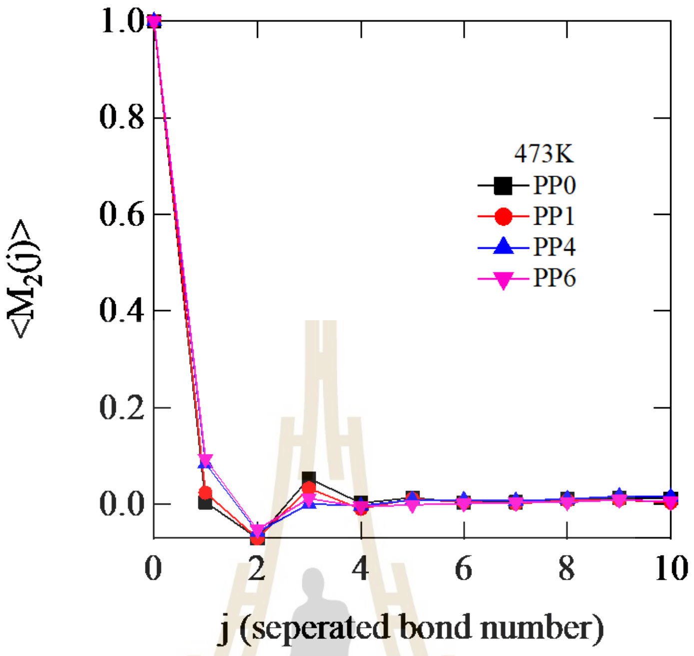

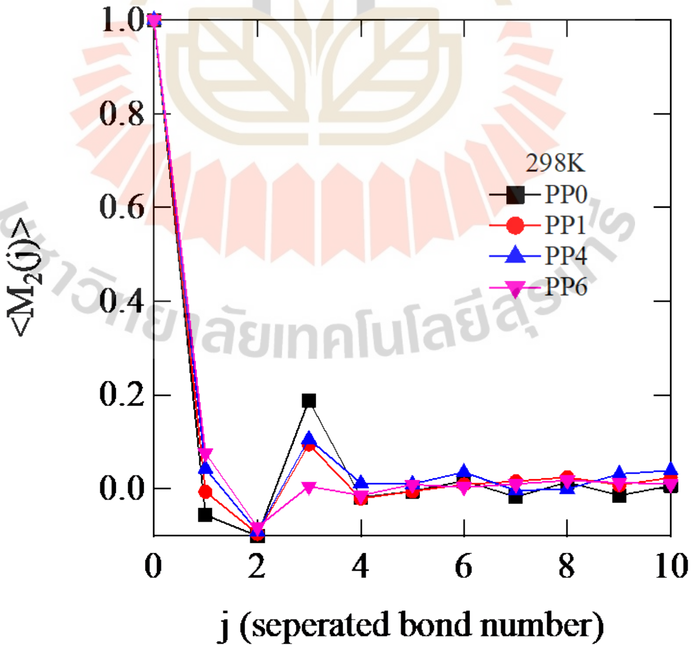

**Figure 4.37** Intramolecular bond orientation correlation functions, $M_2(j)$ as a function of $j$ within the same chain of iPP with racemic diad defect.

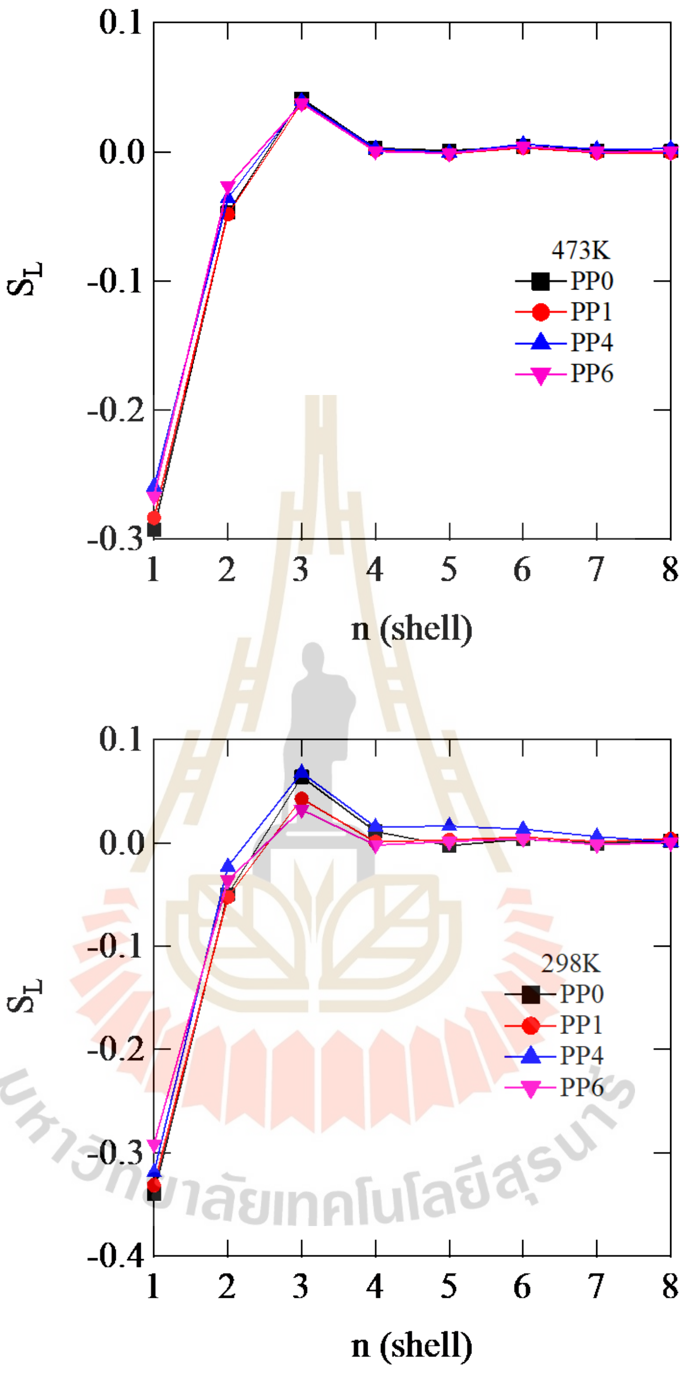

**Figure 4.38** Local intermolecular bond orientation correlation functions $S_L$ as a function of shell number of iPP with racemic diad defect.

#### 4.2.3.4 Average local packing

The local intermolecular packing can be determined by the pair correlation function (PCF) calculated from the probability of encountering particle A in a particular shell about another particle A. In Figure 4.39, the PCFs at different temperatures are compared for each *i*PP system. The PCFs maxima are seen at the third shell, as expected from the location of the minimum in the LJ potential. Focusing on the third shell, the order of local packing is decreased as a function of defect concentration. The PCF maxima increase as the temperature decreases and the difference can be clearly seen when the system has lower amount racemic defect.

In addition, Figure 4.40 depicts the comparison of all *i*PP with different fraction of stereo-defects at the melt (473 K) and crystallization temperature (298 K). In the melted state (473 K), all systems behaved the same, while there are slightly increase in the PCF for higher shells (4 to 6) of PP0 and PP1 systems in the crystallized state (298 K). Therefore, the racemic defects should also hinder the local intermolecular packing probably due to the steric effect of mismatch configuration between the neighboring chains.

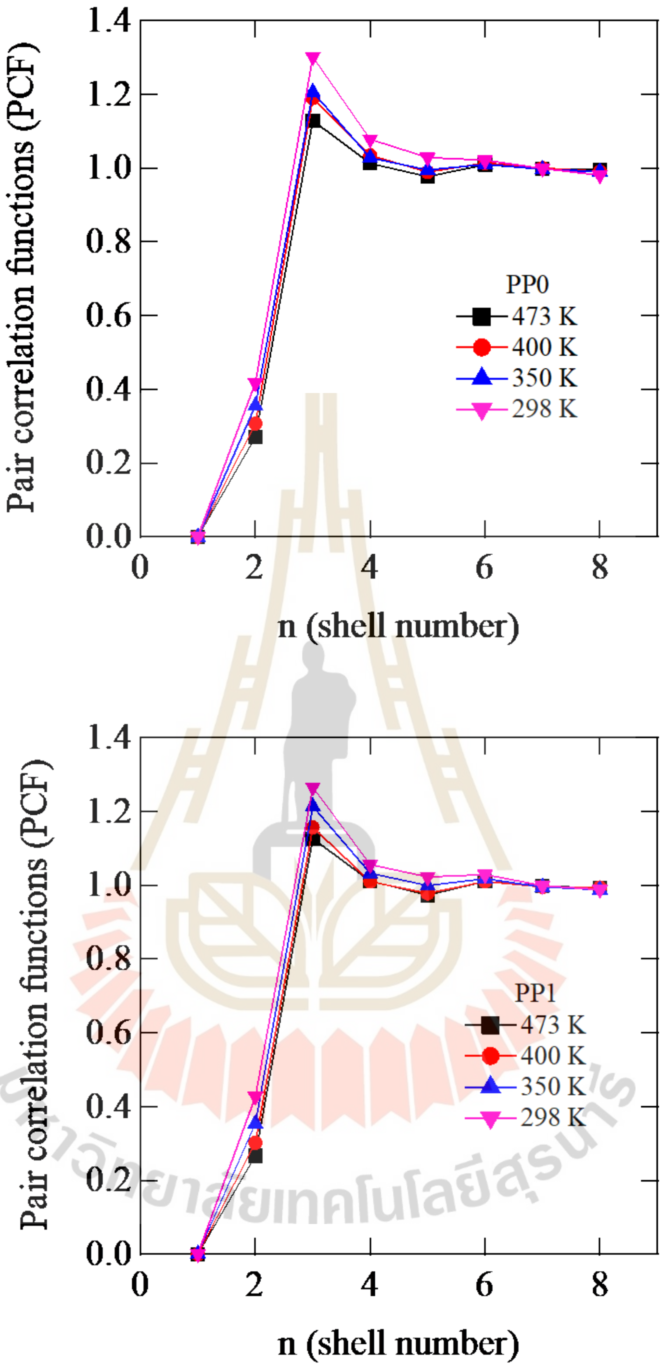

**Figure 4.39** Intermolecular pair correlation functions for each iPP with racemic defects at four temperature.

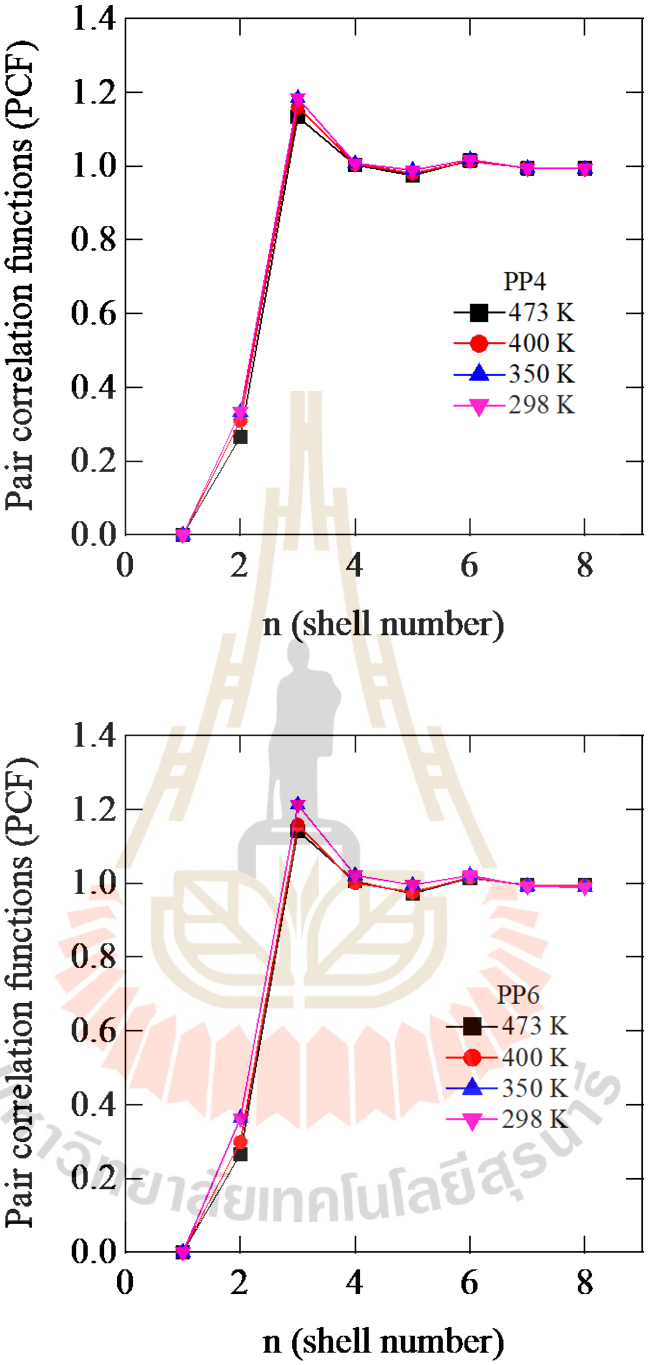

**Figure 4.39** (Continued) Intermolecular pair correlation functions for each iPP with racemic defects at four temperature.

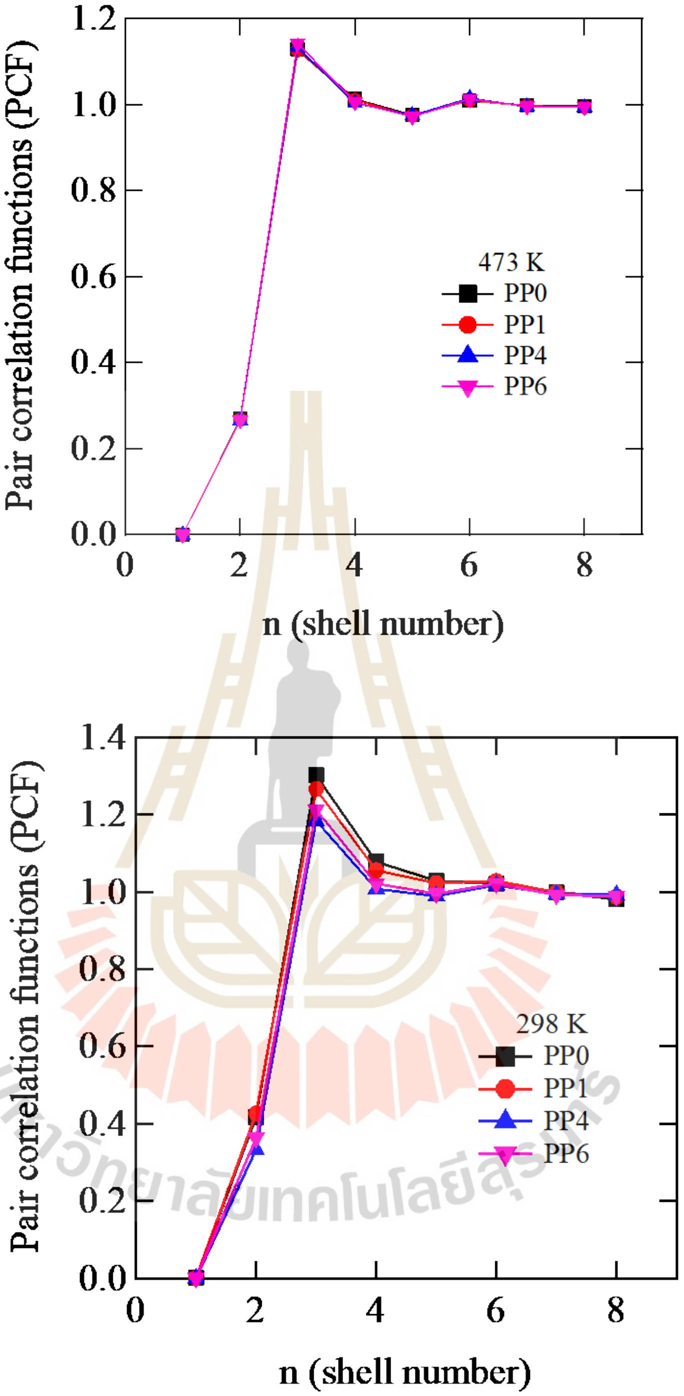

**Figure 4.40** Intermolecular pair correlation functions at 473 K and 298 K of iPP with racemic defects.

## 4.3 Solvation structure of end- and cation- doped carboxylated polyisoprene (PICOOH and PICOOM)

### 4.3.1 Molecular dynamic (MD) simulation of $PI_{10}COOH$ model

The starting model of end-carboxylated polyisoprene with 10 units, $PI_{10}COOH$ is shown in Figure 4.41. After equilibration by MD simulation, the trajectories were used to determine the radial distribution functions (RDF), g(r), the coordination number (CN) between hydrogen and oxygen (H-bond), the mean square displacement (MSD) and the rotational correlation function (RCF) as presented in Figures 4.42 – 4.44, respectively. From the RDF results, the coordination shell is evaluated at the peak position at 2.40 Å. The CN of H-bond of g(r) is 2.14 suggesting that this molecules could have 2 hydrogen bonds at the same time. The dynamics of polymer chains were then studied both in terms of translational (MSD) and orientational motion (RCF). The MSD of $PI_{10}COOH$ is about 16 $Å^2$ during 100 ns at 298 K and the relaxation of the head-to-middle (head-mid) vector and the middle-to-end (mid-end) vector decay to 0.87 and 0.85, respectively. Hence, the hydrogen bonds from the COOH group can apparently slow down the dynamics of $PI_{10}COOH$.

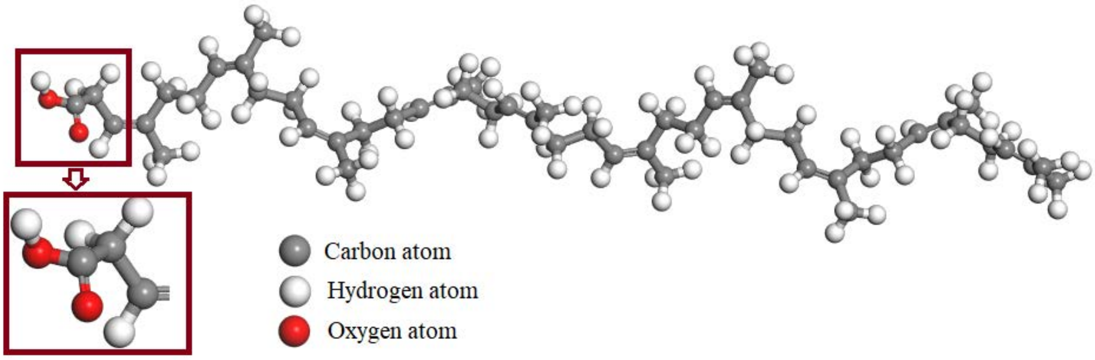

**Figure 4.41** The initial structure of end-carboxylated *cis*-1,4-polyisoprene with 10 units, $(PI)_{10}COOH$.

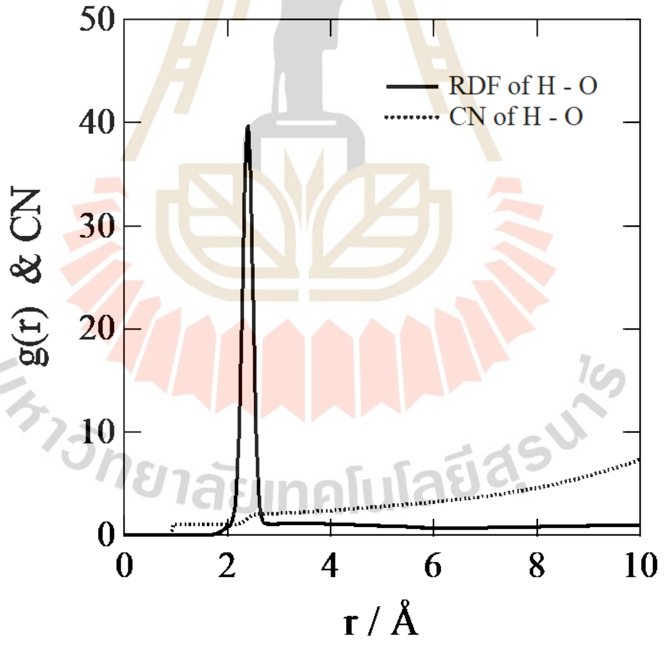

**Figure 4.42** Radial distribution functions (RDF) and running coordination number (CN) from MD simulations of $(PI)_{10}COOH$.

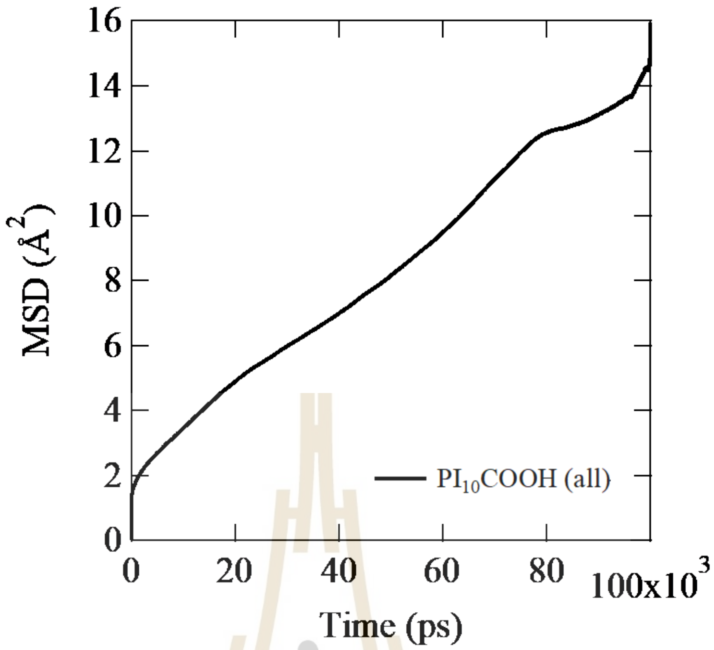

**Figure 4.43** MSD of PI$_{10}$COOH at 298K.

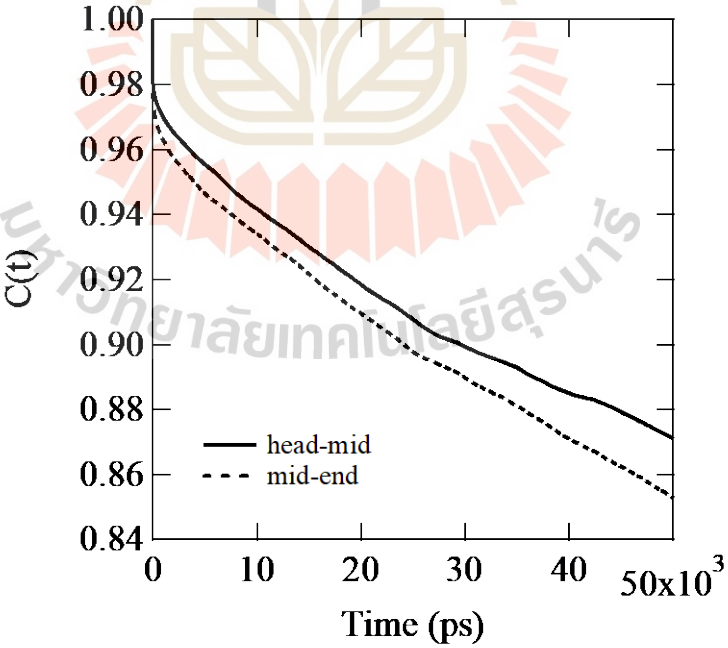

**Figure 4.44** Rotational correlation function of PI$_{10}$COOH.

### 4.3.2 Molecular dynamic (MD) simulation of $(PI_{10}COO)_2Ca$, $PI_{10}COOK$ and $PI_{10}COOLi$ model

The starting model of carboxylate polyisoprene anion with 10 units $(PI)_{10}COO^-$ before cation addition is depicted in Figure 4.45. After equilibration by MD simulation, the trajectories of $(PI_{10}COO)_2Ca$, $PI_{10}COOK$ and $PI_{10}COOLi$ were analyzed to determine the radial distribution functions (RDF), g(r), and the coordination number (CN) between cations with the surrounding oxygen and carbon atoms as presented in Figures 4.46 – 4.48 for $(PI_{10}COO)_2Ca$, $PI_{10}COOK$ and $PI_{10}COOLi$ systems, respectively. From these figures, the RDFs and CNs between the atom pairs of Ca…O (total), Ca…O=, Ca….O-, K…O (total), K…O=, K…O-, Li…O (total), Li…O= and Li…O- were determined. The solid line represents RDF of atom pair while the dot line represents CN of the solvated oxygen atoms. The oxygen environment around $Ca^{2+}$, $K^+$ and $Li^+$ ions obtained from these RDFs was presented in Table 4.7.

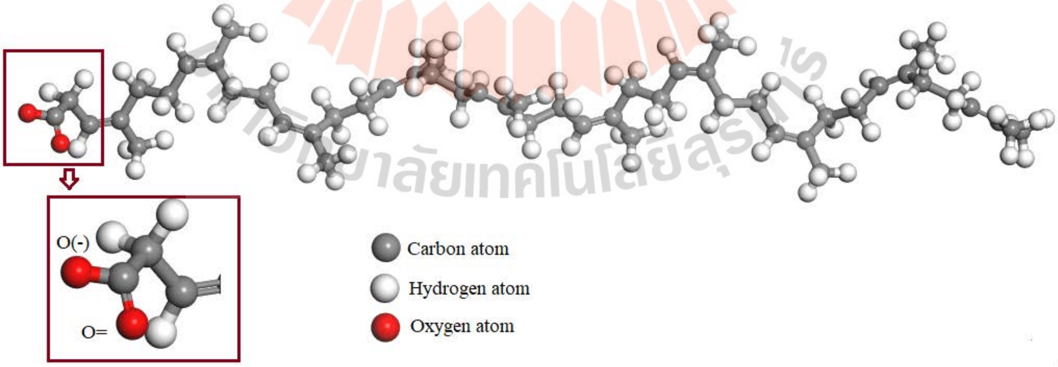

**Figure 4.45** The initial structure of carboxylate poly(cis-1,4-isoprene) with 10 units, $(PI)_{10}COO^-$.

For $PI_{10}(COO)_2Ca$, Figure 4.46, shows that the g(r) with total, O= and O- atoms exhibit a well-defined first coordination shell with a peak position at 2.52 Å. The CN of O atoms around $Ca^{2+}$ ion at the first minimum of g(r) (3.68 Å) is 5.43, which consists of 2.69 O= atom and 2.54 O- atom. The second peak at 4.58 Å has CN of 7.85 O atoms around $Ca^{2+}$ ion, which consists of 3.88 O= and 3.86 O- atom. These findings suggest that there should be about 4 $PI_{10}COO^-$ molecules, by average, to surround each $Ca^{2+}$ ion as illustrated in Figure 4.49.

For $PI_{10}COOK$, Figure 4.47, shows that the g(r) with total, O= and O- atoms show a well-defined first coordination shell and a distinct first peak at 2.94 Å. The CN of O atoms around $K^+$ ion at first minimum of g(r) (4.50 Å) is 4.43, which contains of 2.19 O- and O= atoms. The second peak of RDF is at 4.88 Å and there are 6.15 O atoms around $K^+$ ion, which are from 3.06 O- and O= atoms. From these results, there should be around 2 $PI_{10}COO^-$ molecules to solvate $K^+$ ion as depicted in Figure 4.50.

For $PI_{10}COOLi$, Figure 4.48, shows that the g(r) with total, O= and O- atoms show a well-defined first coordination shell and a distinct first peak at 2.02 Å. The CN of O atoms around $Li^+$ ion at first minimum of g(r) (2.96 Å) is 3.42, which contains of 1.70 O= and 1.72 O- atom. The second peak at 4.00 Å has CN of 7.95 O atoms around $Li^+$ ion, which consists of 3.80 O= and 3.81 O- atom. These results submit that there should be about 2 $PI_{10}COO^-$ molecules to solvate $Li^+$ ion as depicted in Figure 4.51.

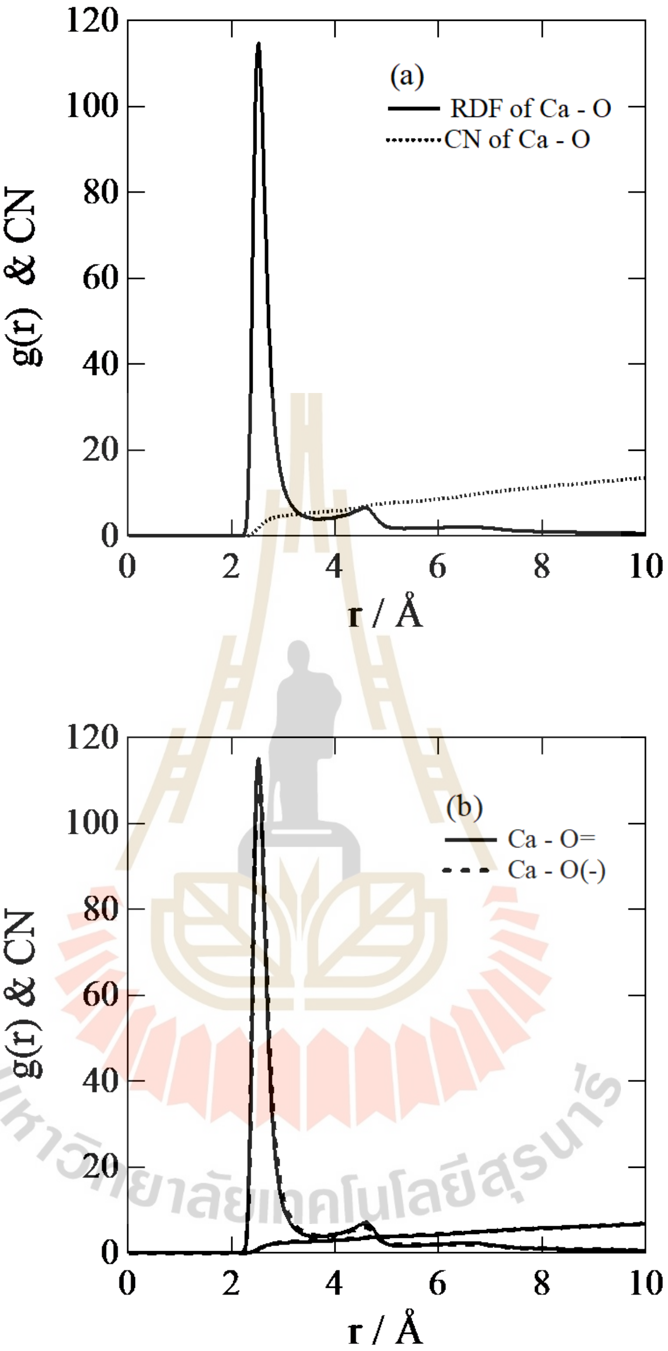

**Figure 4.46** RDF and CN from MD simulations of $(PI_{10}COO)_2Ca$ system: (a) Ca-O (all oxygen) and (b) Ca-O (each oxygen).

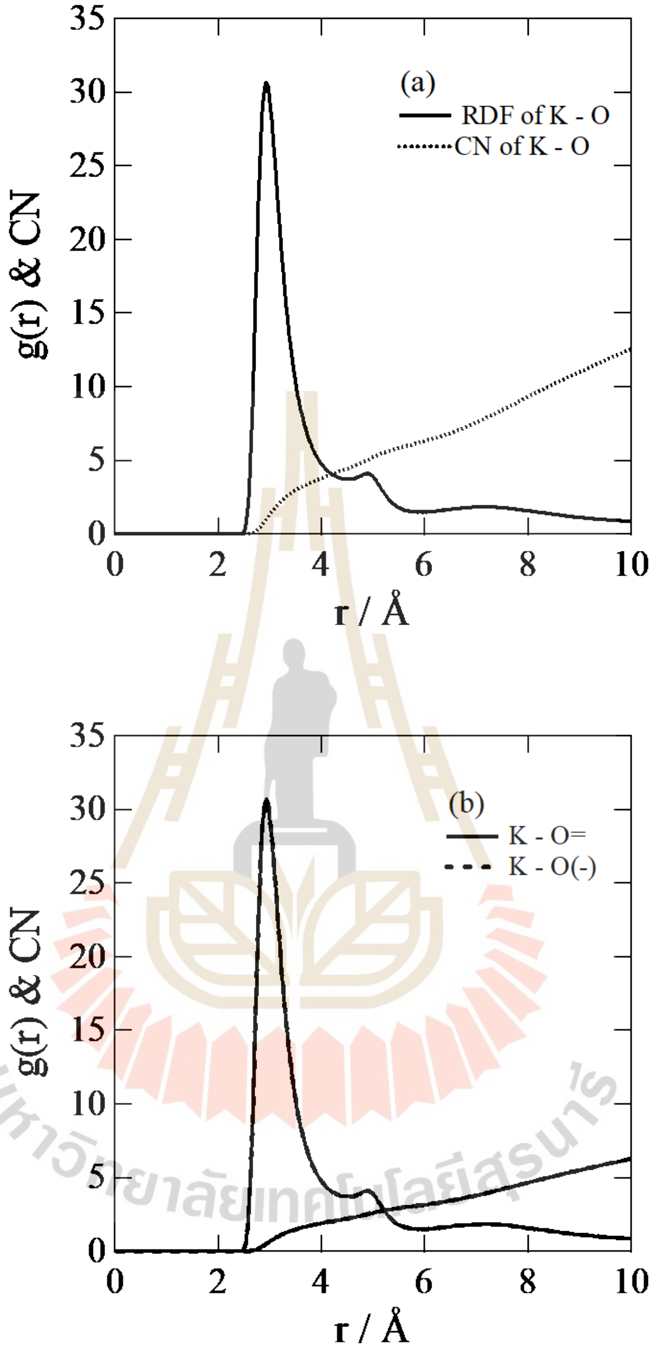

**Figure 4.47** RDF and CN from MD simulations of $PI_{10}COOK$ system: (a) K-O (all oxygen) and (b) K-O (each oxygen).

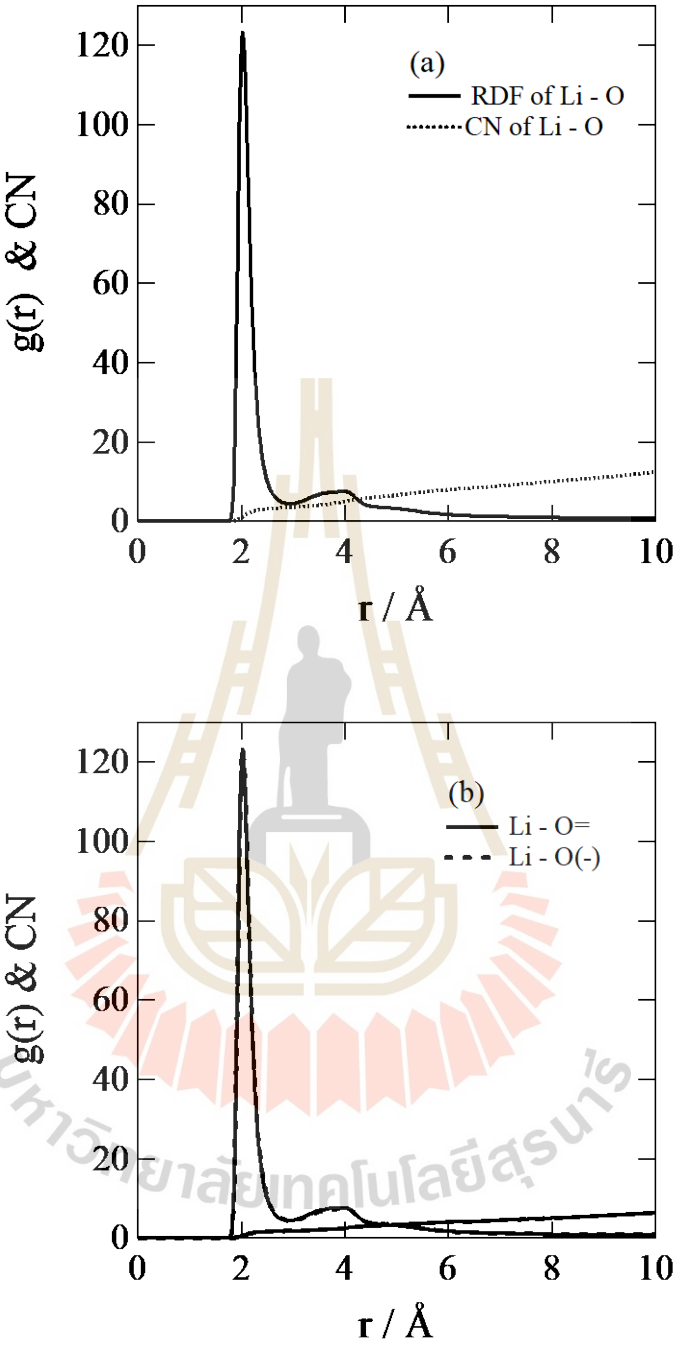

**Figure 4.48** RDF and CN from MD simulations of $PI_{10}COOLi$ system: (a) Li-O (all oxygen) and (b) Li-O (each oxygen).

**Table 4.7** Parameters characterizing the RDF from MD simulation of $Ca^{2+}$ and $K^{+}$ ions systems.

| System | Number of ions | 1st peak |  |  | 2nd peak |  |  |
|---|---|---|---|---|---|---|---|
|  |  | r (Å) 1st max | r (Å) 1st min | $n_{O2-}$ at 1st min | r (Å) 2nd max | r (Å) 2nd min | $n_{O2-}$ at 2nd min |
| Ca-O | 25 | 2.52 | 3.68 | 5.43 | 4.58 | 5.34 | 7.85 |
| Ca-O= | 25 | 2.52 | 3.50 | 2.69 | 4.62 | 5.24 | 3.88 |
| Ca-O(-) | 25 | 2.52 | 3.42 | 2.54 | 4.6 | 5.18 | 3.86 |
| K-O | 50 | 2.94 | 4.50 | 4.43 | 4.88 | 5.84 | 6.15 |
| K-O= | 50 | 2.94 | 4.46 | 2.19 | 4.96 | 5.80 | 3.06 |
| K-O(-) | 50 | 2.94 | 4.46 | 2.19 | 4.96 | 5.80 | 3.06 |
| Li-O | 50 | 2.02 | 2.96 | 3.42 | 4.00 | 6.14 | 7.95 |
| Li-O= | 50 | 2.02 | 2.96 | 1.70 | 3.92 | 5.76 | 3.80 |
| Li-O(-) | 50 | 2.02 | 2.96 | 1.72 | 3.92 | 5.76 | 3.81 |

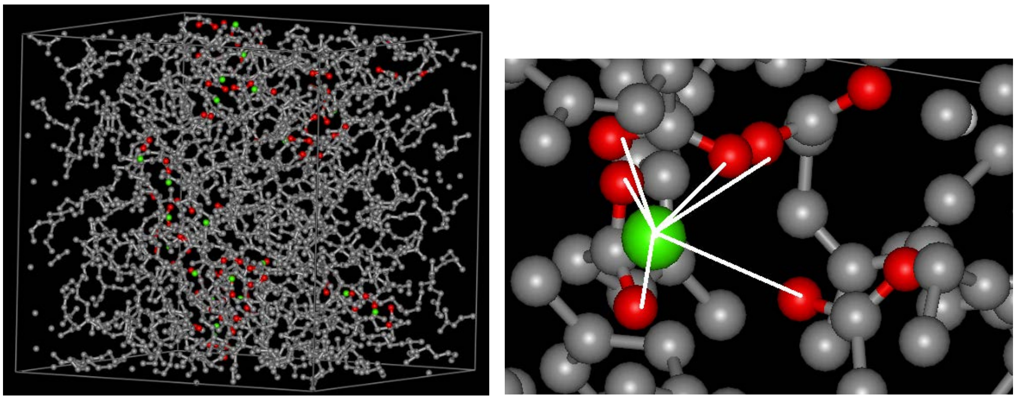
(a) (b)

**Figure 4.49** (a) overall snapshot without hydrogen atoms of $PI_{10}(COO)_2Ca$ and (b) zoom of one $Ca^{2+}$ ion in $PI_{10}(COO)_2Ca$.

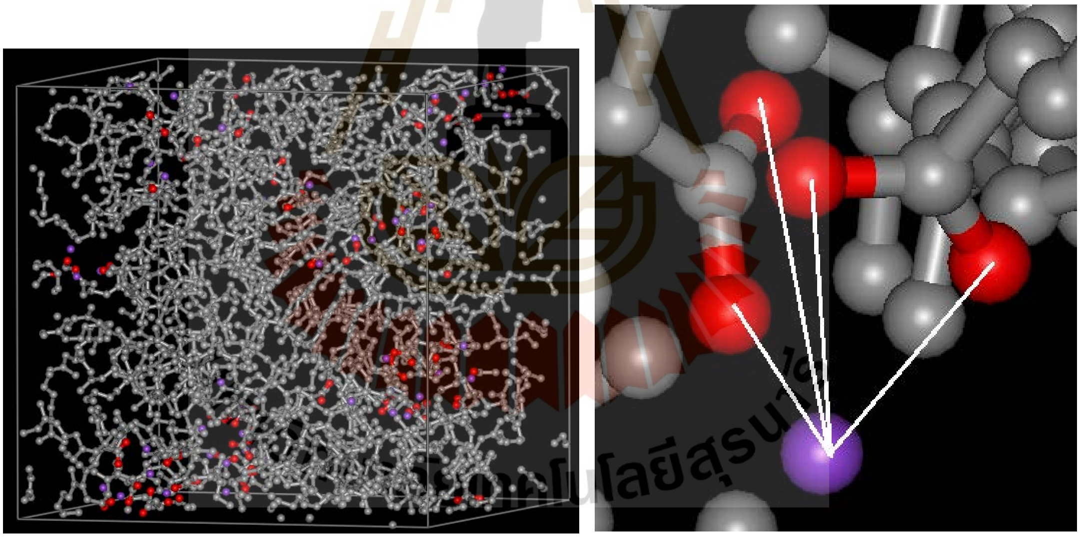
(a) (b)

**Figure 4.50** (a) overall snapshot without hydrogen atoms of $PI_{10}COOK$ and (b) zoom of one $K^+$ ion in $PI_{10}COOK$.

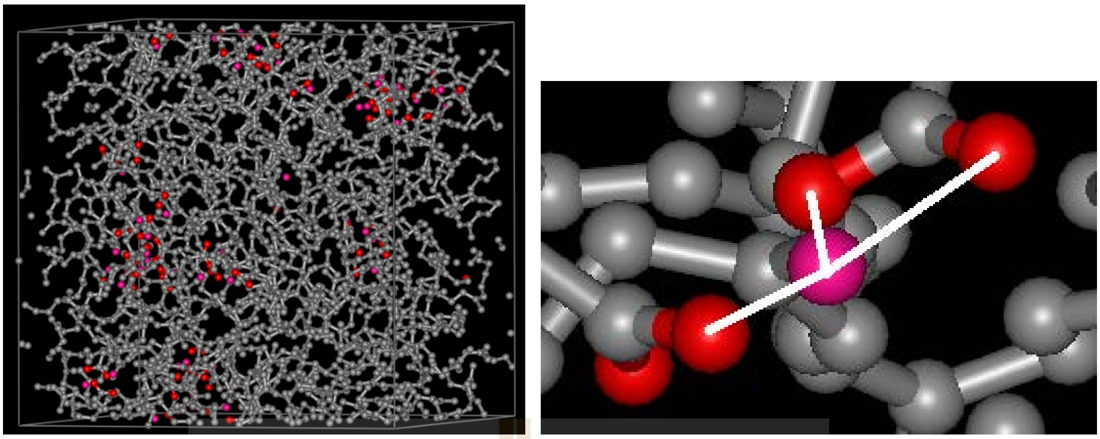

**Figure 4.51** (a) overall snapshot without hydrogen atoms of $PI_{10}COOLi$ and (b) zoom of one $Li^+$ ion in $PI_{10}COOLi$.

The dynamics of $PI_{10}COOM$ (M = $Li^+$, $K^+$, $Ca^{2+}$) were studied both in terms of translational and orientational motion. Translational dynamics were analyzed through the mean square displacement of cation ($Li^+$, $K^+$, $Ca^{2+}$) and oxygen atoms as presented in Figures 4.52 – 4.54. It was found that $K^+$ diffuse several times faster than $Li^+$ and $Ca^{2+}$ ion as: $K^+$ (160 $Å^2$) > $Li^+$ (30 $Å^2$) > $Ca^{2+}$ (6 $Å^2$) within the interval of 100 ns. In addition, the mobility of oxygen atoms in $PI_{10}COOK$ system also faster than in other systems while mobility of oxygen atoms in $PI_{10}COOLi$ diffuse slower than in $PI_{10}COOCa$. Based on the RDF results, each $Li^+$, $K^+$ and $Ca^{2+}$ ions are surrounded by 3, 4 and 6 oxygen atoms, respectively. Possible explanation why $Ca^{2+}$ diffuse slower than $K^+$ ions may be due to the physical network-like structure between bivalent ion and carboxylate group that decrease ion diffusivity.

The orientational dynamics of polymer chains in $PI_{10}(COO)_2Ca$, $PI_{10}COOK$ and $PI_{10}COOLi$ systems were analyzed through the rotational correlation function (RCF). In order to compare the dynamics between the chain segments near the head (carboxylate) and end group, the relaxation of the head-to-middle vector (head-mid) and the middle-to-end vector (mid-end) are compared in Figure 4.55. The RCF of polymer chains in $PI_{10}COOLi$ has the slowest relaxation and the rotational motion of $PI_{10}(COO)_2Ca$ is slower than that of $PI_{10}COOK$. The relaxation times for the mid-end vector in all systems are much greater than that for the head-mid vector due to the aggregation of the carboxylate groups. Bivalent cations cause slower chain relaxation especially for the segment near the head group.

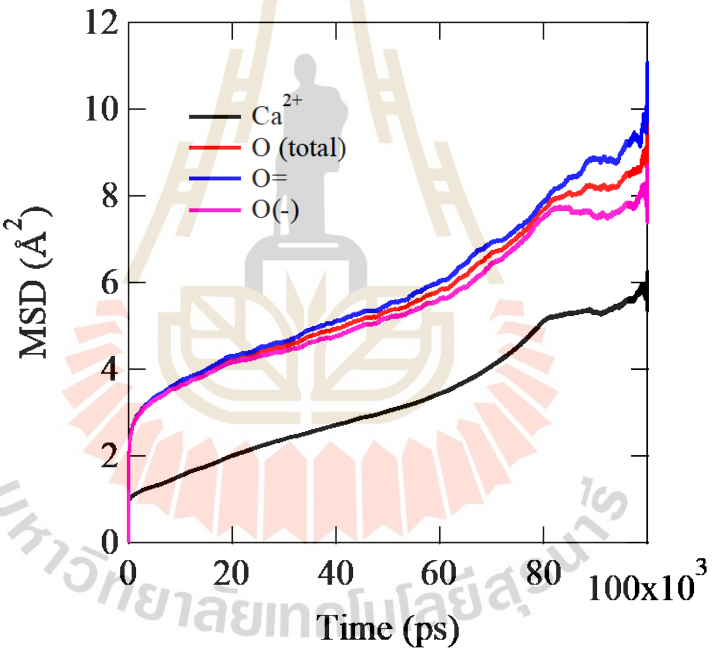

**Figure 4.52** Mean square displacements of $Ca^{2+}$ ion system in $Ca^{2+}$, O (total), O= and O(-) at 298 K.

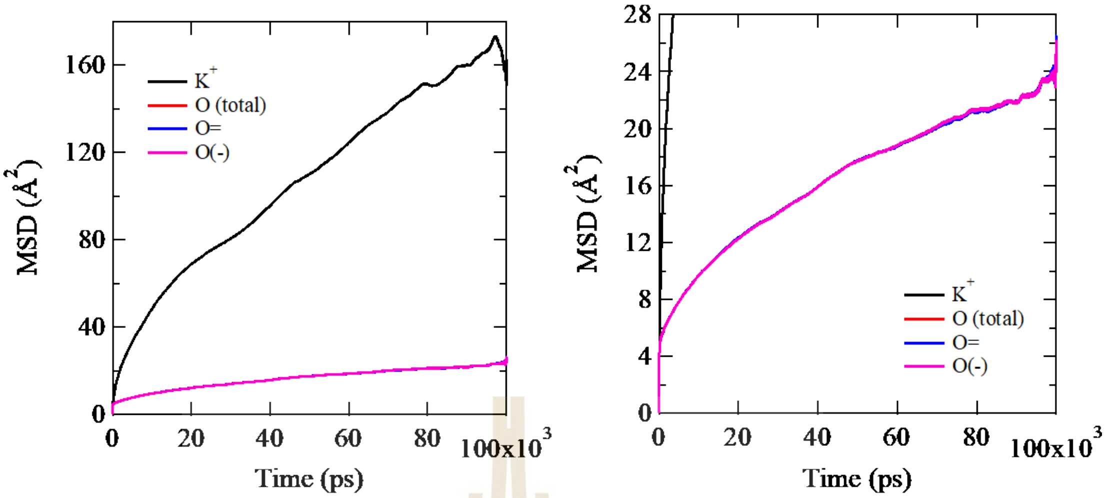

**Figure 4.53** Mean square displacements of K$^+$ ion system in K$^+$, O (total), O= and O(-) at 298 K.

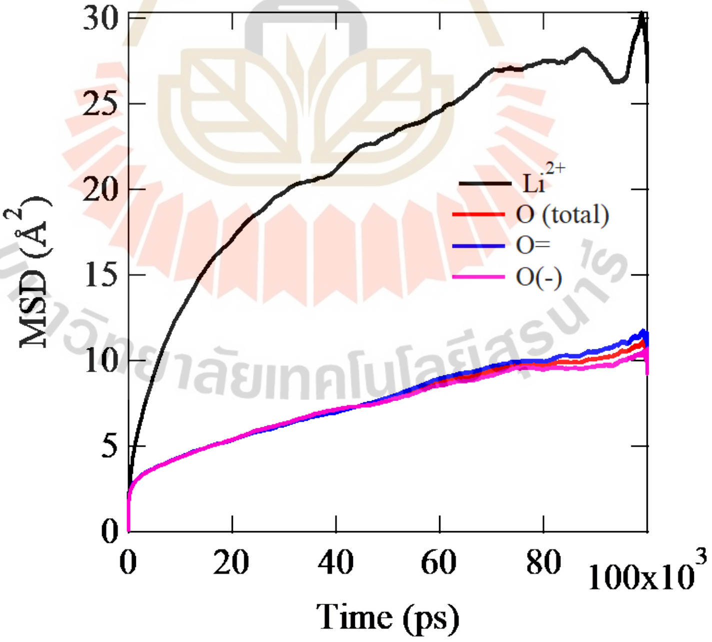

**Figure 4.54** Mean square displacements of Li$^+$ ion system in Li$^+$, O (total), O= and O(-) at 298 K.

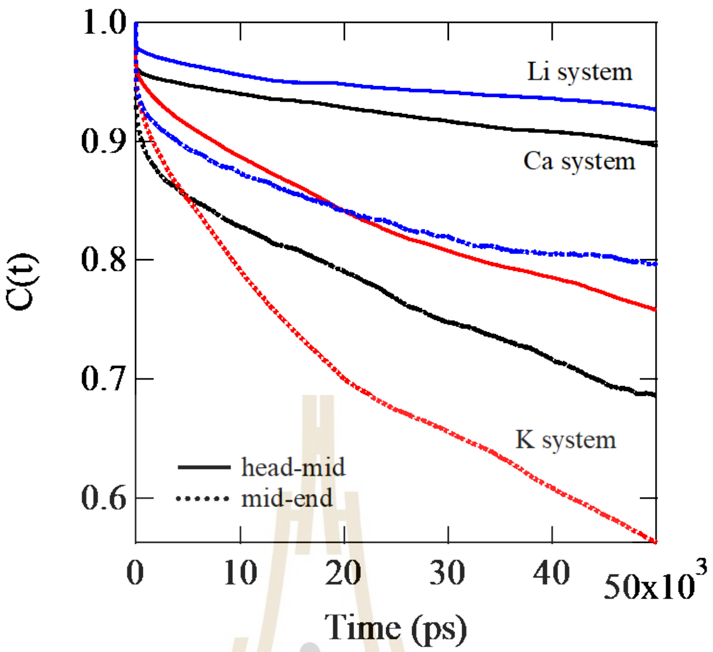

**Figure 4.55** Rotational correlation function of $(PI_{10}COO)_2Ca$, Ca system (black), $PI_{10}COOK$, K system (red) and $PI_{10}COOLi$, Li system (blue).

### 4.3.3 EXAFS studies of calcium and potassium carboxylate salt polyisoprene ($(PI_{30}COO)_2Ca$ and $PI_{30}COOK$)

Two samples of PICOOM (M = $K^+$ and $Ca^{2+}$) composed of either calcium or potassium ions neutralized with carboxylated poly(cis-1,4-isoprene) of 30 repeating units denoted by $(PI_{30}COO)_2Ca$ and $PI_{30}COOK$, respectively, were prepared. The background subtracted and normalized EXAFS spectra for $(PI_{30}COO)_2Ca$ and $PI_{30}COOK$ are plotted as $k^2\chi(k)$ vs. k and Fourier transforms was employed to convert these data from k-space to r-space to obtain the radial structure function (RSF), $|\chi(R)|$ vs. R as presented in Figure 4.56 and 4.57, respectively. Different pattern of $k^2\chi(k)$ and $|\chi(R)|$ can be observed for $(PI_{30}COO)_2Ca$ and $PI_{30}COOK$ implying different local structure of solvated cations. The quality of EXAFS signal for $(PI_{30}COO)_2Ca$ is generally better than $PI_{30}COOK$ system. A prominent first coordination shell of $Ca^{2+}$ and $K^+$ systems at 1.90 and 2.12 Å can be clearly seen. For $PI_{30}COOK$, the peaks at R < 1.44 Å in Figure 4.57 is an artifact due to the residual low-frequency background. Comparing EXAFS data between these two systems, the solvation structure of $Ca^{2+}$ and $K^+$ ions should be different. To compare the solvation structures of $(PI_{30}COO)_2Ca$ and $PI_{30}COOK$, the known crystal structure of structurally similar complexes *i.e.* calcium acetate ($(CH_3COO)_2Ca$) and potassium formate (HCOOK) crystals were used as the standard materials for the data fitting. The experimental EXAFS spectra of these crystals are presented in Figure 4.58 ($(CH_3COO)_2Ca$) and 4.60 (HCOOK). Next, the EXAFS patterns of these standard crystals to $(PI_{30}COO)_2Ca$ and $PI_{30}COOK$ were compared. The peak positions match quite well but the peak amplitude in $(PI_{30}COO)_2Ca$ and $PI_{30}COOK$ are higher than those in $(CH_3COO)_2Ca$ and HCOOK crystal, respectively. These results suggest that the solvation structure of $(PI_{30}COO)_2Ca$ and $PI_{30}COOK$ should be different from the reference crystals as the coordination number of oxygen atom around cation may be different. In this work, we will not try to use the atomic coordinates from MD trajectories to simulate the EXAFS spectra. Instead, we were interested in using them in the fitting procedure for EXAFS spectra in addition to the atomic coordinates from crystal structure. This approach should be interesting in case there is no known standard crystal for the fitting.

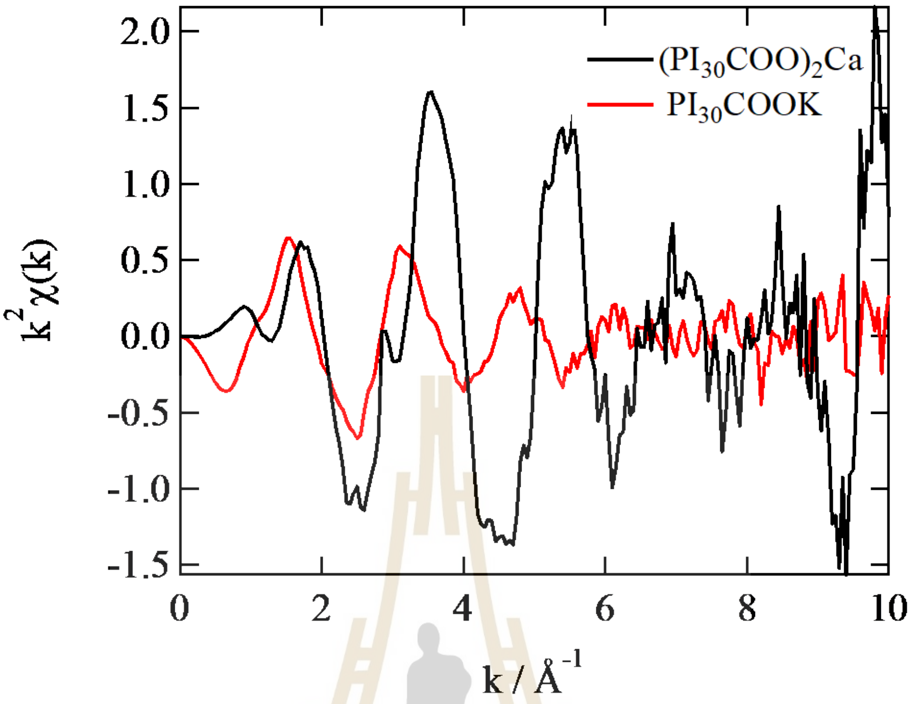

**Figure 4.56** EXAFS data expressed as $k^2\chi(k)$ for $(PI_{30}COO)_2Ca$ and $PI_{30}COOK$.

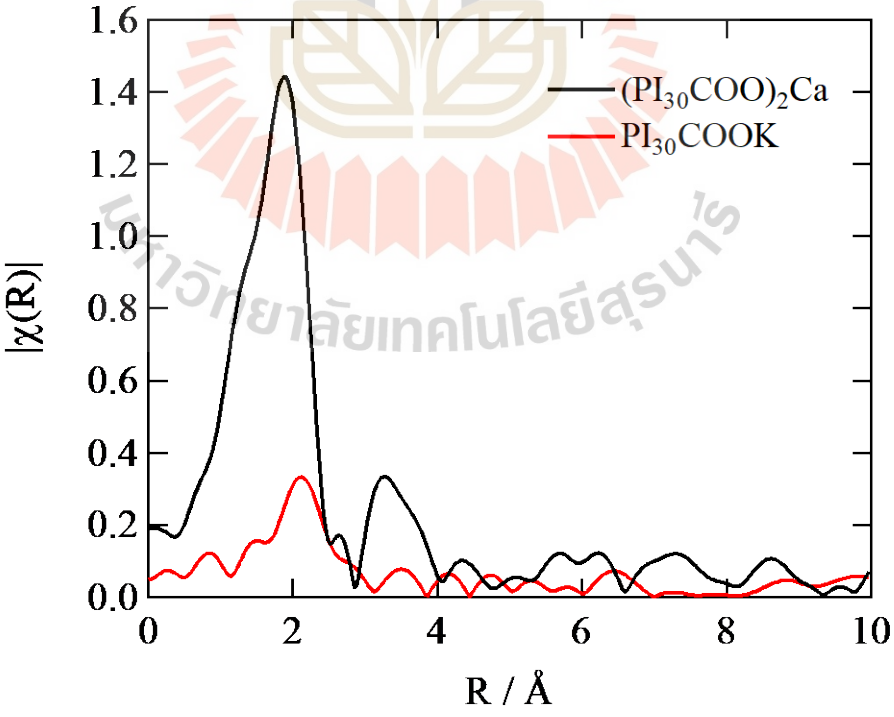

**Figure 4.57** Radial structure function for $(PI_{30}COO)_2Ca$ and $PI_{30}COOK$.

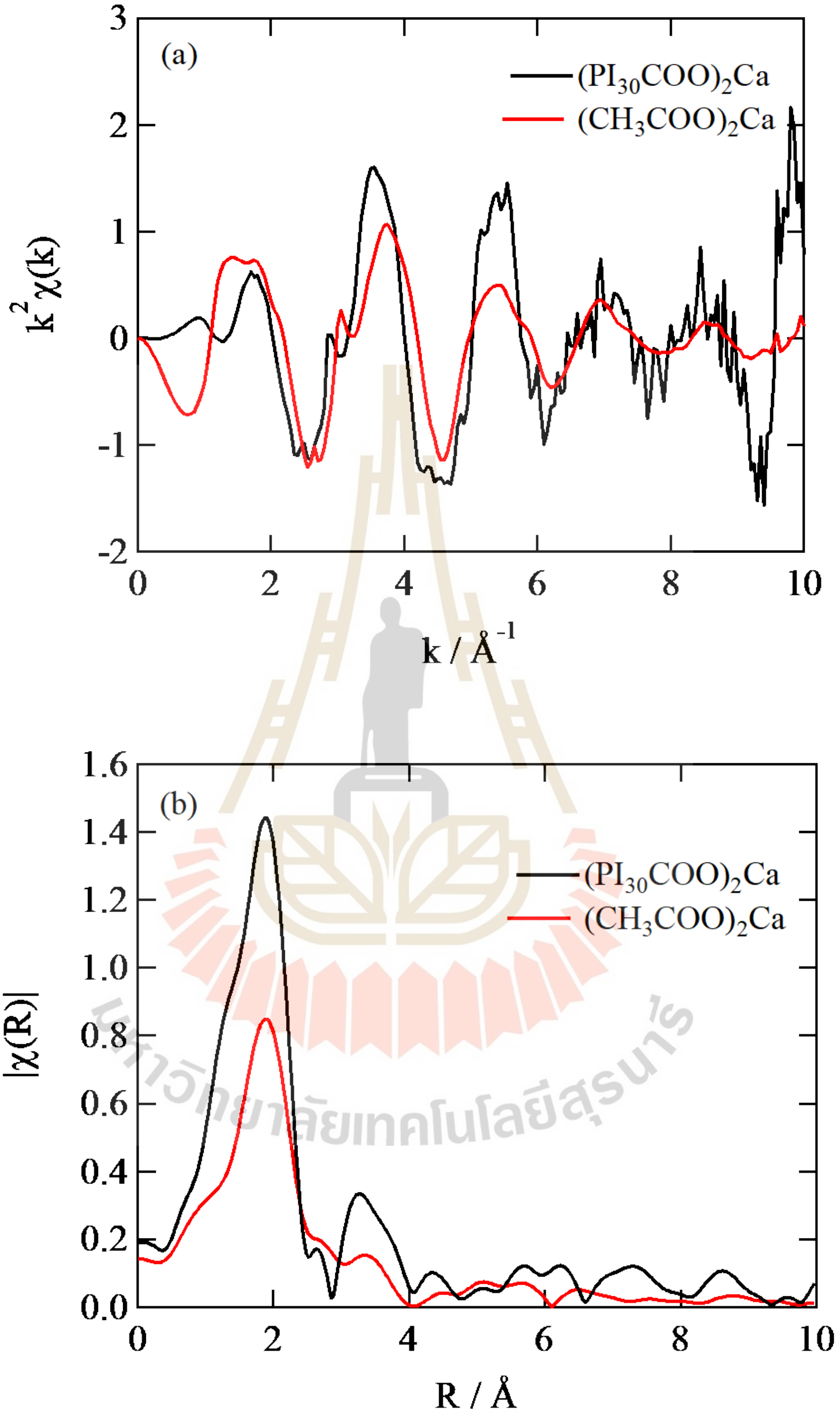

**Figure 4.58** EXAFS data expressed as (a) $k^2\chi(k)$ and (b) radial structure function for $(PI_{30}COO)_2Ca$ and $(CH_3COO)_2Ca$ (standard).

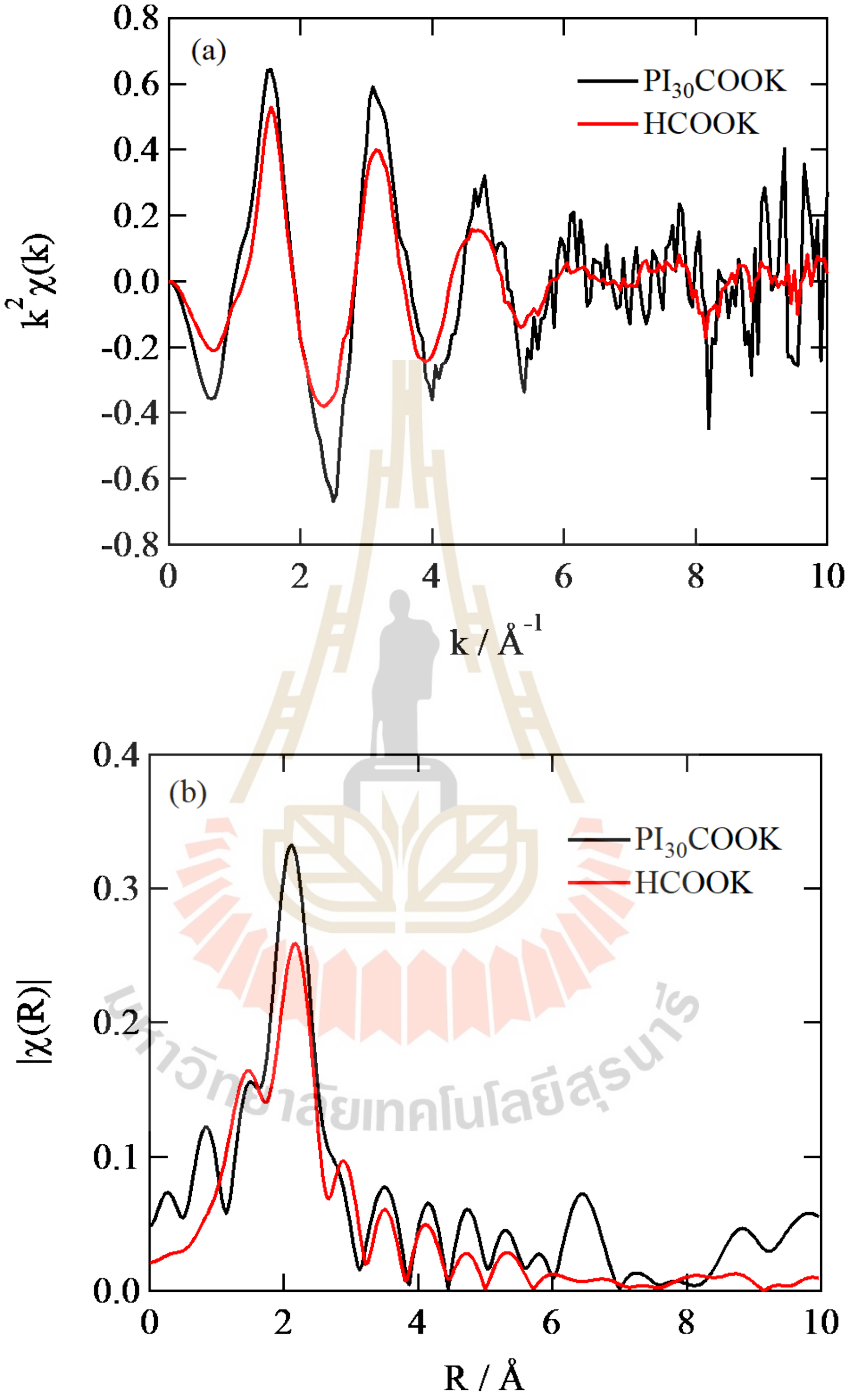

**Figure 4.59** EXAFS data expressed as (a) $k^2\chi(k)$ and (b) radial structure function for $PI_{30}COOK$ and HCOOK (standard).

### 4.3.4 MD-assisted EXAFS fitting

To obtain the detailed local structure of non-crystalline materials, the FEFF simulations and fitting process with ARTEMIS code take the experimental $\chi(k)_{exp}$ function and compare it with a theoretical $\chi(k)_{teo}$ function that is build-up using the theoretical EXAFS paths preciously calculated with FEFF. In this case we considered the number of neighbors = 12, so we decide to fit 4 parameters including the amplitude reduction factor ($S_0^2$), the edge shift ($E_0$), the deviation from the theoretical bond length (reff*delR) and Debye-Waller factor (ss). Three adjustable parameters (the first-shell oxygen Debye-Waller factors, the amplitude reduction and the edge energy) were used to fit the experimental data to the theory for PICOOM samples. EXAFS spectra from experiment and best fits of the structure using the atomic coordinates from MD trajectories of $(PI_{30}COO)_2Ca$ and $PI_{30}COOK$ are presented, respectively, in Figure 4.60 and 4.62. The fitting parameters are listed in Table 4.8.

For $(PI_{30}COO)_2Ca$, the first solvation shell at 2.54 Å should contain oxygen atoms. Using the mean-free-path value from the selected model in MD snapshot (4.8 ± 1.0 Å), the coordination number in $(PI_{10}COO)_2Ca$ was estimated to 6. The average distance and coordination number of oxygen atom from the fitting agree very well with the results from radial distribution function from experiment, which are around 2.54 Å. Therefore, we propose that $(PI_{30}COO)_2Ca$ should have 6 oxygen atoms surrounded $Ca^{2+}$ ion as shown in Figure 4.61. The first shell was surrounded by oxygen atoms from both =O and -O in carboxylate groups as $Ca^{2+}$ ion should be located near the negative charges to produce charge neutrality. In addition, this idea can be compared with the solvation structure of calcium (II) ion in aqueous solution, where eight oxygen atoms are hydrated by calcium (II) ion at the Ca-O distances about 2.46 Å. These distance and coordination number are different from our fitting results possibly because the carboxylate groups in $(PI_{30}COO)_2Ca$ are quite bigger than water molecules that might cause different coordination number whereas the Ca…O distance can be about the same. The best fit results for the first shell parameters using the model form MD trajectory to fit the experimental EXAFS data of $(PI_{30}COO)_2Ca$ system are shown in Table 4.9. The atomic coordinate lists for fitting model that used to create FEFF paths are presented in Table 4.10. As a result of this fit, it can be confirmed that the local atomic arrangement around the calcium ion in a dried $(PI_{30}COO)_2Ca$ has structurally consistent with the MD trajectory.

**Table 4.8** EXAFS parameters of $(PI_{30}COO)_2Ca$ and $PI_{30}COOK$ as determined from the model fitting in comparison with the RDF from MD trajectory.

| Sample | Shell No. | Atom | Distance ( ± 0.10 Å) | N ( ± 1.0) | $\sigma^2$ ($Å^2$) | $E^0$Shift (eV) | R-factor |
|---|---|---|---|---|---|---|---|
| $(PI_{30}COO)_2Ca$ Fitting | 1 | O | 2.54 | 6 | 0.015 | -13.31 | 0.045 |
| $(PI_{30}COO)_2Ca$ Experiment | 1 | O | 2.51 | - | - | - | - |
| $PI_{30}COOK$ Fitting | 1 | O | 2.67 | 4.4 | 0.025 | -12.68 | 0.050 |
| $PI_{30}COOK$ Experiment | 1 | O | 3.12 | - | - | - | - |

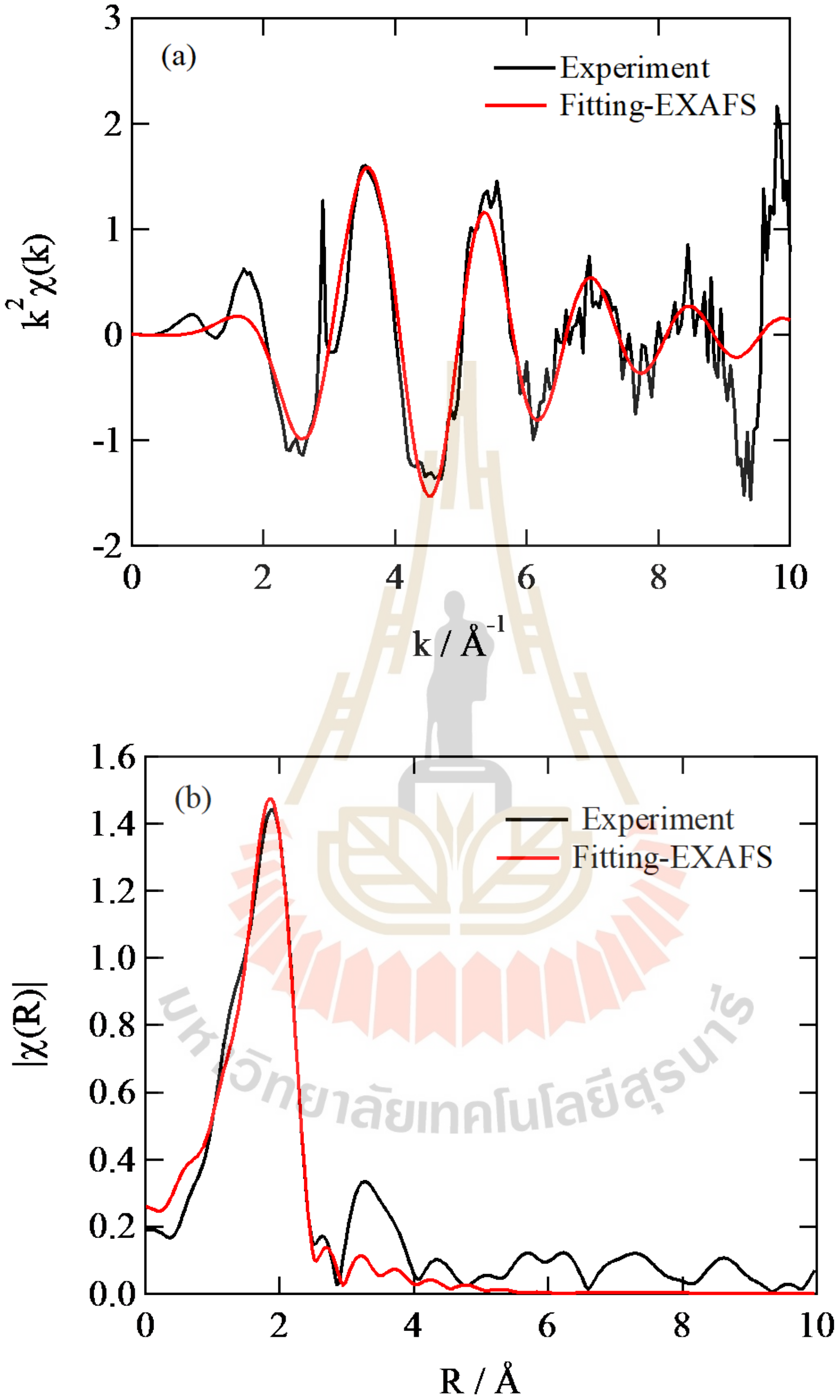

**Figure 4.60** Fit to the first shell of $(PI_{30}COO)_2Ca$ using a snapshot of $(PI_{10}COO)_2Ca$ from MD simulation: (a) $k^2\chi(k)$ and (b) radial structure function.

**Table 4.9** Fit results of $(PI_{30}COO)_2Ca$ by using MD trajectory of $(PI_{10}COO)_2Ca$ model.

| Atom | N | R | {reff + delr} | $E^0$Shift(eV) | $\sigma^2$(Å$^2$) |
|---|---|---|---|---|---|
| O | 1 | 2.223 | 2.22 | -13.310 | 0.0198 |
| O | 1 | 2.259 | 2.26 | -13.310 | 0.0198 |
| O | 1 | 2.353 | 2.35 | -13.310 | 0.0198 |
| C | 1 | 2.409 | 2.41 | -13.310 | 0.0081 |
| C | 1 | 2.721 | 2.72 | -13.310 | 0.0081 |
| O | 2 | 2.756 | 2.76 | -13.310 | 0.0198 |
| C | 2 | 2.790 | 2.79 | -13.310 | 0.0081 |
| C | 1 | 2.943 | 2.94 | -13.310 | 0.0081 |
| C | 1 | 2.992 | 2.99 | -13.310 | 0.0081 |
| O | 1 | 3.181 | 3.18 | -13.310 | 0.0198 |

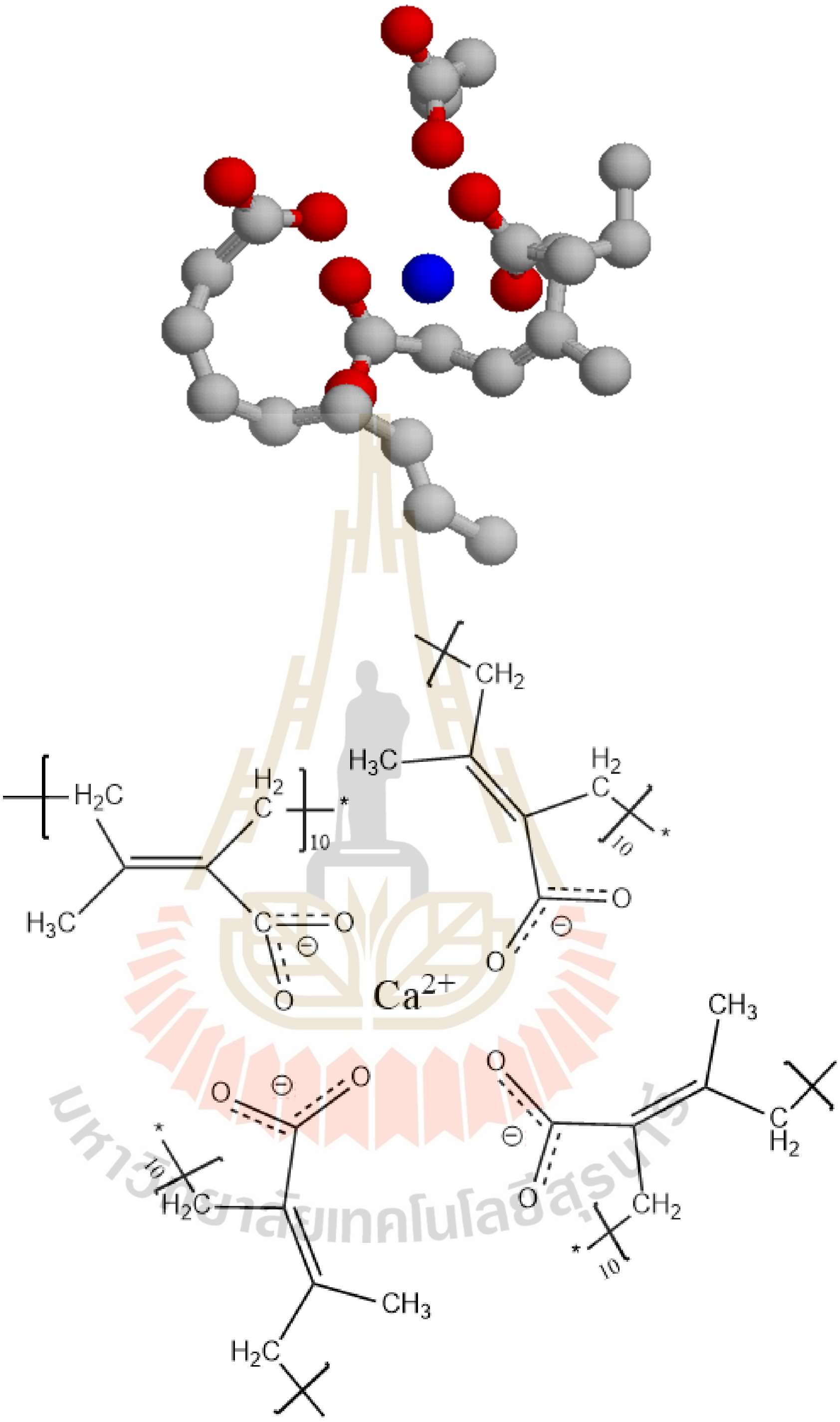

**Figure 4.61** A selected MD snapshot of $PI_{10}(COO)_2Ca$ system and the proposed solvation structure derived from MD results. The gray sphere = carbon atom, red = oxygen atom and blue = $Ca^{2+}$ ion.

**Table 4.10** Atomic coordinates for the fitting model of $(PI_{30}COO)_2Ca$.

| X(Å) | Y(Å) | Z(Å) | Atom type |
|---|---|---|---|
| 0 | 0 | 0 | Ca |
| 1.22 | -2 | 0.49 | O |
| -1.42 | 1.95 | -0.31 | O |
| 0.6 | -0.05 | -2.46 | O |
| -2.01 | 1.49 | 0.68 | C |
| -2.15 | -1.95 | 0.39 | C |
| -1.61 | 1.67 | 1.85 | O |
| 2.45 | 1.63 | -0.38 | O |
| -1.94 | -2 | -1.1 | C |
| -2.69 | -0.89 | 1.02 | C |
| -3.1 | 0.45 | 0.47 | C |
| 2.37 | -2.18 | 0.03 | C |
| 3.02 | -1.44 | -0.73 | O |
| 0.84 | -0.1 | 3.49 | C |
| 0.56 | 0.17 | -3.69 | C |
| -1.7 | -3.15 | 1.18 | C |
| 1.99 | 0.84 | 3.23 | C |
| 3.1 | 2.66 | -0.1 | C |
| 3.27 | 0.43 | -2.56 | Ca |
| 1.54 | 2.29 | 3.41 | C |
| 2.41 | 3.69 | 0.79 | C |
| -0.71 | -0.18 | -4.45 | C |
| -2.96 | -2.96 | -1.71 | C |
| -1.89 | 0.68 | -4.11 | C |
| 1.53 | 0.58 | -4.36 | O |
| 3.13 | -3.43 | 0.46 | C |
| 0.62 | -0.65 | 4.7 | C |
| -2.96 | -2.81 | -3.21 | C |
| 4.24 | 3.01 | -0.47 | O |
| -0.52 | -1.61 | 4.94 | C |
| 1.07 | 3.65 | -3.65 | C |
| 3.07 | 3.78 | 2.15 | C |
| 3.27 | 2.87 | -3.13 | O |
| 2.71 | 3.25 | 3.32 | C |
| 2.65 | -3.12 | -3.55 | C |
| 4.2 | -3.2 | 1.5 | C |
| 2.52 | 3.87 | -3.25 | C |
| -2.43 | 1.69 | -4.81 | C |

For $PI_{30}COOK$, according to Figure 4.62, the relatively small size of the peak over 3 Å in PI30COOK samples causes the fitting difficult when the peak is smaller. It also affects a greater shape by distorting from the background noise. Thus, it can be assigned the only the first shell coordination and the fitting parameters are listed in Table 4.8. Each potassium should be coordinated by 4 oxygen atoms at 2.67 Å for $PI_{30}COOK$. The previous report based on MD simulation with polarized QM-based force field (Borodin, 2001) and the experimentally observed values (Marcus, 1988) of $K^+$ ion in water suggest that $K^+$ ion should be surrounded by 6 - 7 oxygen atoms at a distance of 2.6 - 2.8 Å. This distance fall within the same range as our fitting results in both cases, and it is possible that 4 oxygen atoms are from two carboxylate groups as the model shown in Figure 4.63. The best fit results for the first shell parameters using the model form MD trajectory with the experimental EXAFS data of $PI_{30}COO_2K$ system are shown in Table 4.11. The atomic coordinates used to generate FEFF paths are presented in Table 4.12.

By comparing the distance of cation-oxygen, different cations also affect the number of oxygen atoms in the first coordination shell. The radius of the first coordination sphere of potassium in $PI_{30}COOK$ is larger than calcium in $(PI_{30}COO)_2Ca$. This result is reasonable because the Van der Waals radius ($Ca^{2+}$: 2.00 Å and $K^+$: 2.75 Å) of $Ca^{2+}$ ion is smaller, so the optimum radius at which the oxygen atoms can enter is reduced. Also, $K^+$ has a larger and lower electro-negativity than $Ca^{2+}$ ions, so the number of oxygen atoms around $K^+$ ions should be less than that of $Ca^{2+}$.

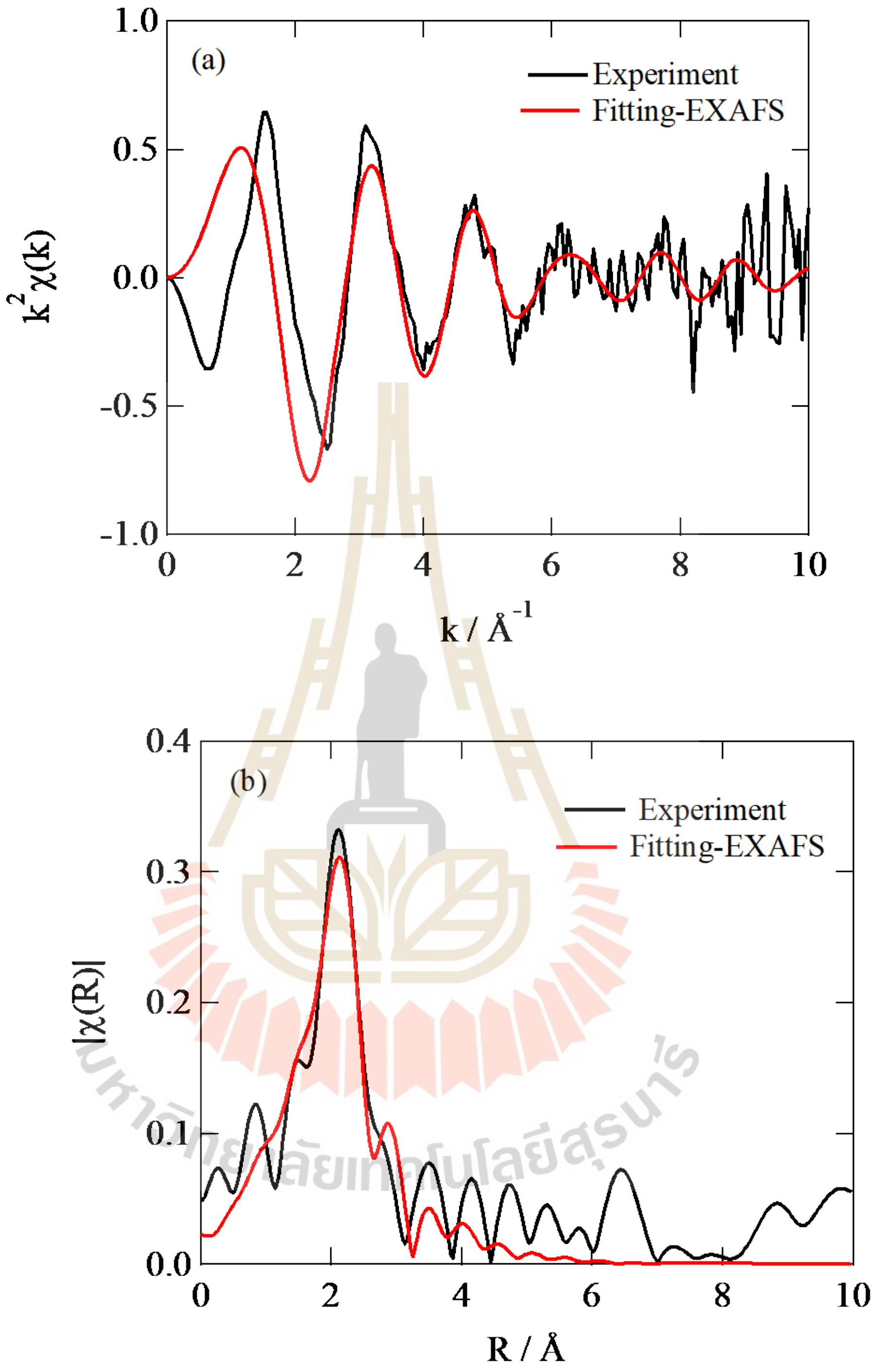

**Figure 4.62** Fit to the first shell of $PI_{30}COOK$ using a snapshot of $PI_{10}COOK$ from MD simulation: (a) $k^2\chi(k)$ and (b) radial structure function.

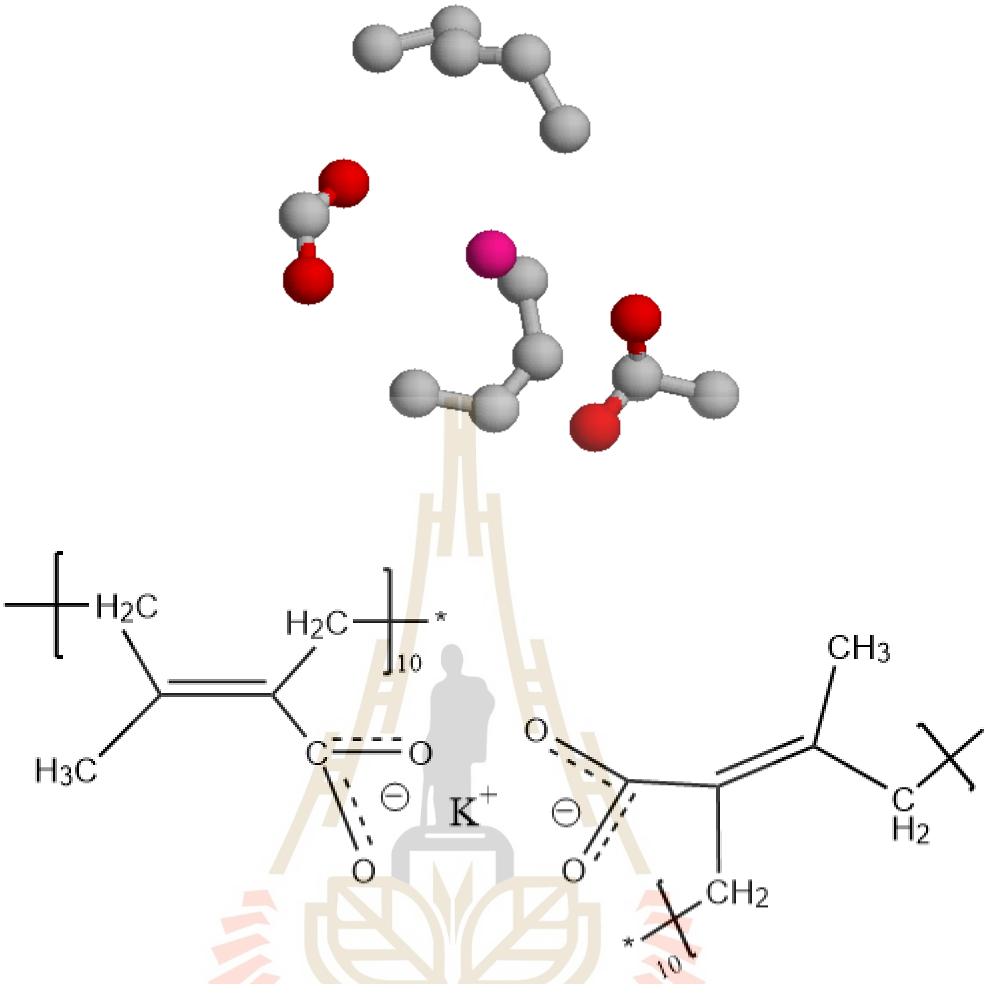

**Figure 4.63** A selected MD snapshot of $PI_{10}COOK$ system and the proposed solvation structure derived from MD results. The gray sphere = carbon atom, red = oxygen atom and pink = $K^+$ ion.

**Table 4.11** Fit results of $PI_{30}COOK$ by using MD trajectory of $PI_{10}COOK$ model.

| Atom | N | R | {reff + delr} | $E^0$Shift(eV) | $\sigma^2$(Å$^2$) |
|---|---|---|---|---|---|
| O | 1 | 2.980 | 2.98 | -12.676 | 0.0138 |
| C | 1 | 3.063 | 3.06 | -12.676 | 0.030 |
| O | 1 | 3.121 | 3.12 | -12.676 | 0.0138 |
| O | 1 | 3.269 | 3.27 | -12.676 | 0.0138 |
| C | 1 | 3.291 | 3.29 | -12.676 | 0.030 |
| C | 1 | 3.349 | 3.35 | -12.676 | 0.030 |
| C | 3 | 3.442 | 3.44 | -12.676 | 0.030 |
| C | 1 | 3.544 | 3.54 | -12.676 | 0.030 |
| C | 1 | 3.631 | 3.63 | -12.676 | 0.030 |
| C | 1 | 3.680 | 3.68 | -12.676 | 0.030 |

**Table 4.12** Atomic coordinates for the fitting model of $PI_{30}COOK$.

| X(Å) | Y(Å) | Z(Å) | Atom type |
|---|---|---|---|
| 0 | 0 | 0 | K |
| 1.28 | 0.29 | -2.88 | O |
| -0.97 | -3.08 | -0.39 | C |
| -1.53 | -2.59 | -1.39 | O |
| 0.22 | -3.44 | -0.41 | O |
| 0.21 | 2.83 | -2.04 | C |
| -3.04 | 0.41 | 1.8 | C |
| -1.09 | 1.45 | 3.17 | C |
| 0.34 | 0.76 | -3.56 | C |
| -0.76 | 3.34 | -1.28 | C |
| -1.76 | -3.2 | 0.91 | C |
| -2.44 | 1.6 | 2.52 | C |
| 3.9 | -0.24 | -0.05 | C |
| -0.33 | 4.05 | -0.02 | C |
| 0.09 | 2.25 | -3.43 | C |
| 3.06 | 2.35 | 1.64 | C |
| -2.21 | 3.2 | -1.68 | C |
| 1.88 | -1.7 | 3.43 | O |
| 3.63 | 1 | 2.04 | C |
| -0.41 | 0.08 | -4.29 | O |
| 0.61 | -2.72 | -3.38 | K |
| -1.38 | -0.76 | 4.29 | C |
| -1.02 | 0.69 | 4.49 | C |
| 3.27 | 0.6 | 3.27 | C |
| 4.62 | 0.21 | 1.22 | C |
| -3.04 | 2.79 | 2.51 | C |

# CHAPTER V

# CONCLUSION

There are three main parts in this thesis. The first part is to study the effect of some 1-butene defects on crystallization and morphology of isotactic polypropylene (*i*PP). The summary is as following. Isothermal crystallization of *isotactic* polypropylene with a small amount of 1-butene (G-resin samples; MT12-s and MT18-s) and linear *i*PP (V30G) was investigated by polarized optical microscopy (POM), differential scanning calorimetry (DSC) and synchrotron small/wide-angle X-ray scattering/diffraction (SAXS/WAXD). V30G, MT12-s and MT18-s, respectively, have similar average molecular weights of 233k, 283k and 236k g/mol with PDI = 7.7, 7.3, 6.8 and MFR at 230°C/2.16 kg = 23.3, 13.3, 19.7 g/10 min. The content of 1-butene in MT12-s and MT18-s are 6.43 and 5.20 wt%. The negative spherulites are observed for V30G, but the crystal sizes are too small to identify for MT12-S and MT18-s. So, 1-butene defects have some impact on the formation of negative spherulites and cause smaller spherulites size. The induction time is decreased and the crystallization is accelerated for short-branched PP. Isothermal crystallization kinetics of these samples can be more studied by Avrami analysis and the result suggests that the dimension crystal growth ($n$) and the crystallization rate ($k$) tend to increase for short-branched PP. For SAXS analysis, the electron density correlation function was used to estimate the long period (D) and the lamellar thickness (L). The D is increased for short-branched PP (from 19 to 26 nm). In general, short-branched PP samples have higher amorphous (*La*) and *L*, but lower *L/D* ratio than L-*i*PP. Namely, the degree of crystallinity is lower for short-branched PP, this result agrees with DSC, SAXS and WAXD. The diffraction peak of monoclinic $\alpha$ forms can be detected in all PP samples, whereas the orthorhombic $\gamma$ forms were found only for short-branched PP.

The second part employed molecular simulation to investigate the effect of bimodal mixed molecular weight and stereo-irregular defects on crystallization of short polyethylene (PE) and isotactic polypropylene (*i*PP) models, respectively. Monte Carlo (MC) simulations of structure formation for monodisperse PE, bidisperse PE mixtures and *i*PP with few stereo-irregular defects were performed based on the coarse-grained PE chains on a high coordination lattice. Local intra- and inter-chain interactions were treated by the rotational isomeric state (RIS) model and Lennard-Jones (LJ) potential, respectively. Properties determined from simulations were the mean square radius of gyration, the occupancy of *trans* state and orientation correlation functions, global orientation order parameter and the pair correlation functions. All these parameters reveal the crystallization process. The simulations of monodisperse PE show that a high degree of crystallinity can be achieved within reasonable computational time. For the bi-dispersed PE, there is the phase separation between the short and long chains before the crystallization starts. The shorter chains crystallize faster than the long chain components if their composition is high enough. Chain packing for short chain systems is denser than that of the long chains. For the crystallization of *i*PP with some stereo-irregular defects, the fractions of *trans-gauche* or helix sequence are decreased when *i*PP chains contain more content of racemic defects. Chains with larger amount of defects have more disordered conformation and hinder the intermolecular packing, because the steric effect causes the mismatch configuration between neighboring chains. It is apparent that racemic defects in iPP chains hinder the formation of $3_1$ helix, retard the crystallization and decreases the tendency to crystallize.

The final part is to employ a combination of molecular dynamics (MD) simulation and synchrotron X-ray absorption fine structure (EXAFS) spectroscopy to investigate the solvation structures and dynamics of cation-doped carboxylated poly(cis-1,4,isoprene), PICOOM (where M is $Li^+$, $K^+$ or $Ca^{2+}$) were used for MD studies but only $K^+$ and $Ca^{2+}$ were used for EXAFS experiment). For the PICOOM complex, the results indicated that there were two separated shells from PICOO-oxygen atoms to coordinate with lithium, potassium and calcium ions. The EXAFS patterns of $(PI_{30}COO)_2Ca$ and $PI_{30}COOK$ were compared with standard materials, which have known crystal structure *i.e.* calcium acetate $(CH_3COO)_2Ca$ and potassium formate (HCOOK). The solvation structure of $(PI_{30}COO)_2Ca$ and $PI_{30}COOK$ should be different from the reference crystals because the coordination numbers of the oxygen atom around the cation were different. A procedure fitting the EXAFS spectra using the selected atomic coordinates generated by molecular dynamic trajectories was used. From the MD result of PICOOLi, it was found that the Li…O coordination number (CN) = 3.35, 7.95 at r = 2.96, 4.00 Å for the first and second coordination, respectively. There should be two carboxylate groups with each group give one and two oxygens to solvate the $Li^+$ ion. For the $(PICOO)_2Ca$ system, the Ca…O coordination number (CN) = 6 at r = 2.54 Å is comparable to MD simulation that can resolve two coordination shells *i.e.*CN= 5.4, 7.8 at r = 3.68, 5.34 Å for the first and second coordination, respectively. The first coordination shell of $Ca^{2+}$ ion (within a distance of 3.68 Å) in the $(PICOO)_2Ca$ matrix is mainly from four carboxylate groups with three groups that give one oxygen each and another that gives two oxygen atoms to solvate the $Ca^{2+}$ ion to give the average number of about 5.4 oxygen atoms. For the PICOOK case, the K…O coordination number (CN) = 4 at r = 2.67 Å is close to that from MD simulation with two coordination shells *i.e.* CN = 4.43, 6.15 at r = 4.50, 5.84 Å for the first and second coordination, respectively. The first coordination shell of the $K^+$ ion (within a distance of 4.43 Å) in PICOOK matrix is mainly from two carboxylate groups with give two oxygens to solvate this cation.

# REFERENCES

# REFERENCES

Abe, A., Jernigan, R.L., and Flory, P.J. (1966). Conformational energies of n-alkanes and the random configuration of higher homologs including polymethylene. **Journal of the American Chemical Society.** 88: 631-639.

Adachi, K., and Kotaka, T. (1993). Dielectric normal mode relaxation. **Progress in Polymer Science.** 18(3): 585-622.

Ahmadi, M., Hawke, L.G.D., Goldansaz, H., and van Ruymbeke, E. (2015). Dynamics of Entangled Linear Supramolecular Chains with Sticky Side Groups: Influence of Hindered Fluctuations. **Macromolecules.** 48: 7300-7310.

Akten E.D., and Mattice, W.L. (2001). Monte Carlo Simulation of Head-to-Head, Tail-to-Tail Polypropylene and Its Mixing with Polyethylene in the Melt. **Macromolecules.** 34: 3389-3395.

Allen, M.P., and Tildesley, D.J. (1989). **Computer Simulation of Liquids.** First ed. Oxford University.

Anspoks, A., and Kuzmin, J. (2011). Interpretation of the Ni K-edge EXAFS in nanocrystalline nickel oxide using molecular dynamics simulations. **Journal of Non-Crystalline Solids.** 357: 2604-2610.

Auriemma, F., and Rosa, C.D. (2002). Crystallization of metallocene-made isotactic polypropylene: Disordered modifications intermediate between the α and γ forms. **Macromolecules.** 35(24): 9057-9068.

Balbontin, G., Dainelli, D., Galimberti, M., and Paganetto, G. (1992). Thermal behaviour of highly stereoregular syndiotactic polypropene from homogeneous catalysts. **Die Makromolekulare Chemie.** 193: 693-703.

Boese, D., and Kremer, F. (1990). Molecular dynamics in bulk cis-polyisoprene as studied by dielectric spectroscopy. **Macromolecules.** 23(3): 829-835.

Borodin, O., Bell, R. L., Li, Y., Bedrov, D. and Smith. G. D. (2001). Polarizable and nonpolarizable potentials for K+ cation in water. **Chemical Physics Letters.** 336: 292-302.

Bravakis, A.M., Bailey, L.E., Pigeon, M., and Collins, S. (1998). Synthesis of elastomeric poly(propylene) using unsymmetrical zirconocene catalysts, marked reactivity differences of “rac”- and “meso”-like diastereomers. **Macromolecules.** 31: 1000.

Chaodamrongsakul, J., Merat, K., Klysubun, W., and Vao-soongnern, V. (2013). A combined molecular dynamic simulation and X-ray absorption spectroscopy to investigate the atomistic solvation structure of cation in poly(vinyl alcohol): potassium thiocyanate (KSCN) solid electrolytes. **Journal of Non-Crystalline Solids.** 379: 21-26.

Charles, E., Seymour C., and Benedict R. (2003). Seymour/Carraher's polymer chemistry. **CRC Press.** 43-45. ISBN 978-0-8247-0806-1.

Chen, C.M., and Higgs, P.G. (1998). Monte Carlo simulation of polymer crystallization in dilute solution. **The Journal of Chemical Physics.** 108: 4305-4314.

Chen, Q., Huang, C., Weiss, R.A., and Colby, R.H. (2015). Viscoelasticity of Reversible Gelation for Ionomers. **Macromolecules.** 48: 1221-1230.

Chen, Q., Tudryn, G.J., and Colby, R.H. (2013). Ionomer dynamics and the sticky Rouse model. **Journal of Rheology.** 57: 1441-1462.

Chien, J.C.W., Iwamoto, Y., Rausch, M.D., Wedler, W., and Winter, H.H. (1997). Homogeneous binary zirconocenium catalyst system for polypropylene polymerizations. 1. Isotactic/atactic interfacial compatabilized polymer having thermoplastic elastomeric properties. **Macromolecules.** 30: 3447.

Cho, J., and Mattice, W.L. (1997). Estimation of long range interaction in coarse-grained rotational isomeric state polyethylene chains on a high coordination lattice. **Marcomolecules.** 30: 637-644.

Clancy, T.C., and Mattice, W.L. (2000). Rotational isomeric state chains on a high coordination lattice: dynamic Monte Carlo algorithm details. **The Journal of Chemical Physics.** 112: 10049-10055.

Clancy, T.C., and Mattice, W.L. (2001). Miscibility of Poly(vinyl chloride) Melts Composed of Mixtures of Chains with Differing Stereochemical Composition and Stereochemical Sequence. **Macromolecules.** 34: 6482-6486.

Cobzaru, C., Deisenhofer, S., Harley, A., Troll, C., Hild, S., and Rieger, B. (2005). Novel high and ultrahigh molecular weight polypropylene plastomers by asymmetric hafnocene catalysts. **Macromolecular Chemistry and Physics.** 206: 1231-1240.

Corradini, P. (2003). The discovery of isotactic polypropylene and its impact on pure and applied science. **Journal of Polymer Science Part A: Polymer Chemistry.** 42(3): 391-395.

Cui, K., Ma, Z., Tian, N., Su, F., Liu, D. and Li, L. (2018). Multiscale and Multistep Ordering of Flow-Induced Nucleation of Polymers. **Chemical Reviews.** 118: 1840-1886.

D'Angelo, P., Petit, P.E., and Pavel, N.V. (2004). Double-Electron Excitation Channels at the $Ca^{2+}$ K-Edge of Hydrated Calcium Ion. **The Journal of Chemical Physics.** 108: 11857-11865.

D'Angelo, P., Di Nola, A., Filipponi, A., Pavel, N.V., and Roccatano, D. (1994). **The Journal of Chemical Physics.** 100: 985-994.

D'Angelo, P., Di Nola, A., Mangoni, M., and Pavel, N.V. (1996). An extended x-ray absorption fine structure study by employing molecular dynamics simulations: Bromide ion in methanolic solution. **The Journal of Chemical Physics.** 104: 1779-1790.

Dang, L.X., Schenter, G.K., Glezakou, V.A., and Fulton, J.L. (2006). Molecular simulation analysis and X-ray absorption measurement of $Ca^{2+}$, $K^{+}$ and $Cl^{-}$ ions in solution. **The Journal of Chemical Physics.** B 110: 23644-23654.

Darsey, J.A. (1981). Selt-Consistent Field Conformational Energy Calculations for n-Alkanes and Characterizations of Polymethylene. **Macromolecules.** 14: 1575-1581.

Deisenhofer, S., Feifel, T., Kukral, J., Klinga, M., Leskela, M., and Rieger, B. (2003). Asymmetric metallocene catalysts based on dibenzothiophene: a new approach to high molecular weight polypropylene plastomers. **Organometallics.** 22: 3495-3501.

Di Cicco, A., Minicucci, M., and Filipponi, A. (1997). New advances in the study of local structure of molten binary salts. **Physical Review Letters.** 78: 460-463.

Dietrich, U., Hackmann, M., and Rieger, B. (2000). A new class of thermoplactic elastic polypropenes prepared with a high activity “dual-side” zirconocene catalyst. **Rubber Chemistry and Technology.** 73: 839-846.

Dietrich, U., Hackmann, M., Rieger, B., Klinga, M., and Leskela, M. (1999). Control of stereoerror formation with high activity “dual-side” zirconocene catalysts: A novel strategy to design the properties of thermoplastic elastic polypropenes. **Journal of the American Chemical Society.** 121: 4348-4355.

Dodda, L.S., Cabeza de Vaca, I., Tirado-Rives, J., Tirado-Rives, J., and Jorgensen, W.L. (2017). LigParGen web server: An automatic OPLS-AA parameter generator for organic ligands. **Nucleic Acids Research.** 45(W1): W331-W336.

Dodda, L.S., Vilseck, J.Z., Tirado-Rives, J., and Jorgensen, W.L. (2017). 1.14*CM1A-LBCC: Localized Bond-Charge Corrected CM1A Charges for Condensed-Phase Simulations. **The Journal of Physical Chemistry.** B 121(15): 3864-3870.

Doruker, P., and Mattice, W.L. (1997). Reverse mapping of coarse grained polyethylene chains from the second nearest neighbor diamond lattice to an atomistic model in continuous space. **Marcomolecules.** 30: 5520-5526.

Essmann, U., Perera, L., Berkowitz, M.L., Darden, T., Lee, H., and Pedersen, L.G. (1995). A smooth particle mesh Ewald method. **The Journal of Chemical Physics.** 103(19): 8577-8593.

Filipponi, A., and Di Cicco, A. (1995). Short-range order in crystalline, amorphous, liquid, and supercooled germanium probed by x-ray absorption spectroscopy. **Physical Review Journals.** 51: 12322-12336.

Flory, P.J. (1953). ‘‘Principles of Polymer Chemistry’’. **Cornell University Press.**

Freund, R.M. (2004). The Steepest Descent Algorithm for Unconstrained Optimization and a Bisection Line-search Method**. Massachusetts Institute of Technology.**

Fujiwara, S., and Sato, T. (1999). Molecular dynamics simulation of structure formation of short chain molecules. **The Journal of Chemical Physics.** 110: 9757-9764.

Gauthier, W.J., and Collins, S. (1995). Elastomeric poly(propylene), propagation models and relationship to catalyst structure. **Macromolecules.** 28: 3779.

Glatter, O., and Kratky, O. (1982). **Small Angle X-ray Scattering.** Academic Press, London.

Gou, Q.Q., Li, H.H, Yu, Z.Q., Chen, E.Q., Zhang, Y.D., and Yan, S.K. (2007). Crystallization behavior of a propylene-1-butene random copolymer in its α and γ modifications. **Colloid and Polymer Science.** 285: 1149-1155.

Hauser, G., Schmidtke, J., and Strobl, G. (1998). The Role of Co-Units in Polymer Crystallization and Melting: New Insights from Studies on Syndiotactic Poly(propene-co-octene). **Marcromolecules.** 31(18): 6250-6258.

Hess, B., Bekker, H., Berendsen, H.J.C., and Fraaije, J.G.E.M. (1997). LINCS: a linear constraint solver for molecular simulations. **Journal of Computational Chemistry.** 18(12): 1463-1472.

Hiltner, A., Dias, P.S., Poon, B., Ronesi, V., Chang, A., Ansems, P., and Baer, E. (2003). Elastomeric properties of new propylene-ethylene copolymers under cyclic loading. **ANTEC.** 1780-1784.

Hirschfelder, J.O., Curtiss, C.F., and Bird, R.B. (1954). Molecular theory of gases and liquids. **New York: Wiley.**

Hockney, R.W., Goel, S.P., and Eastwood, J.W. (1974). Quiet high-resolution computer models of a plasma. **Journal of Computational Physics.** 14(2): 148–158.

Hoffman, J.D., and Weeks, J.J. (1962). Melting process and the equilibrium melting temperature of polychlorotrifluoroethylene. **Journal of Research of the National Bureau of Standards, Section A: Physics and Chemistry.** 66: 13-28.

Hoffmann, M.M., Darab, J.G., Palmer, B.J., and Fulton, J.L. (1999). A transition in the $Ni^{2+}$ complex structure from six- to four-coordinate upon formation of ion pair species in supercritical water: an X-ray absorption fine structure, near-infrared, and molecular dynamics study. **The Journal of Physical Chemistry.** A 103: 8471-8482.

Hosier, I.L., Alamo, R.G., Estero, P., Isasi, J.R., and Mandelkern, L. (2003). Formation of the α and γ Polymorphs in Random Metallocene−Propylene Copolymers. Effect of Concentration and Type of Comonomer. **Marcromolecules.** 36: 5623-5636.

Hosier, I.L., Alamo, R.G., Esteso, P., Isasi, J.R., and Mandelkern, L. (2003). Formation of the α and γ Polymorphs in Random Metallocene−Propylene Copolymers. Effect of Concentration and Type of Comonomer. **Macromolecules.** 36(15): 5623-5636.

Hosoda, S., Hori, H., Yada K.I., Nakahara, S., and Tsuji, M. (2002). Degree of Comonomer Inclusion into Lamella Crystal for Propylene/Olefin Copolymers. **Polymer.** 43: 7451-7460.

Hu, W. (2000). The melting point of chain polymers. **The Journal of Chemical Physics.** 113: 3901-3908.

Hu, W., Mathot, V., Alamo, R., Gao, H., and Chen, X. (2016). Crystallization of statistical copolymers. **Advances in Polymer Science.** doi:10.1007/12_2016_349.

Ivanov, D.A., Amalou, Z., and Magonov, S.N. (2001). Real-time evolution of the lamellar organization of poly(ethylene terephthalate) during crystallization from the melt: high-temperature atomic force microscopy study, **Macromolecules.** 34(26): 8944-8952.

Ivanov, D.A., Legras, R., and Jonas, A.M. (1999). Interdependencies between the evolution of amorphous and crystalline regions during isothermal cold crystallization of poly(ether-ether-ketone), **Macromolecules.** 32(5): 1582-1592.

Jalilehvand, F., Spangberg, D., Patric, L-R. Hermansson, K., Ingmar Persson, I. and Sandstrolm M. (2001). Hydration of the Calcium Ion. An EXAFS, LargeAngle X-ray Scattering, and Molecular Dynamics Simulation Study. **Journal of the American Chemical Society.** 123: 431-441.

Jeon, K., Palza, H., Quijada, R., and Alamo, R.G. (2009). Effect of comonomer type on the crystallization kinetics and crystalline structure of random isotactic propylene 1-alkene copolymers. **Polymer.** 50: 832-844.

Jorgensen, W.L., and Tirado-Rives, J. (2005). Potential energy functions for atomic-level simulations of water and organic and biomolecular systems. **Proceedings of the National Academy of Sciences of the United States of America.** U.S.A.102: 6665-6670

Kalapat, D., Tang, Q., Zhang, X., and Hu, W. (2017). Comparing crystallization kinetics among two G-resin samples and iPP via Flash DSC measurement. **Journal of Thermal Analysis and Calorimetry.** 128: 1859-1866.

Keller, A. (1952). Morphology of crystallizing polymers. **Nature.** doi:10.1038/169913a0.

Keller, A. (1957). Single crystals in polymers: evidence of a folded-chain configuration. **Philosophical Magazine.** 2: 1171-1175.

Koberstein, J.T., and Stein, R.S. (1983). Small-angle x-ray scattering measurements of diffuse phase-boundary thicknesses in segmented polyurethane elastomers, **Journal of Polymer Science Polymer Physics Edition.** 21(10): 2181-2200.

Kumar, S.K., and Douglas, J.F. (2001). Gelation in Physically Associating Polymer Solutions. **Physical Review Letters.** 87: 188301-188304.

Lee, B., Shin, T.J., Lee, S.W., Yoon, J., Kim, J., and Ree, M. (2004). Secondary crystallization behavior of poly (ethylene isophthalate-co-terephthalate): time-resolved small-angle X-ray scattering and calorimetry studies, **Macromolecules.** 37(11): 4174-4184.

Lee, K.B., Kweon, J., Lee, H.J., and Park, H. (1996). A $13^{C}$ NMR Determination for Monomer Compositions in Ethylene-Propylene Copolymers, Ethylene-Propylene-Butene-1, and Ethylene-Propylene-Diene Terpolymers. **Polymer Journal.** 28(8): 696-702.

Lehmus, P., Kokko, E., Leino, R., Luttikhedde, H.J.G., Rieger, B., and Seppala, J. V. (2000). Chain end isomerization as a side reaction in metallocene-catalyzed ethylene and propylene polymerizations. **Macromolecules.** 33: 8534-8540.

Lei, Y., and Lodge, T.P. (2012). Effects of component molecular weight on the viscoelastic properties of thermoreversible supramolecular ion gels via hydrogen bonding. **Soft Matter.** 8: 2110-2120.

Leibler, L., Rubinstein, M., and Colby, R.H. (1991). Dynamics of reversible networks. **Macromolecules.** 24: 4701-4707.

Linford, R.G. (1995). EXAFS studies of polymer electrolytes. **Chemical Society Reviews.** 24: 267-277.

Lu, D.P., and Guan, R. (2000). Properties of Isotactic Polypropylene and iPP/Talc Blends Functionalized by Electron Beam Irradiation. **Polymer International.** 49: 1389-1394.

Luo, J., Liang, Y., Yang, J., Niu, H., Dong, J.Y., and Han, C.C. (2001). Mechanisms of nucleation and crystal growth in a nascent isotactic polypropylene/poly (ethylene-cooctene) in-reactor alloy investigated by temperature-resolved synchrotron SAXS and DSC methods, **Polymer.** 52(20): 4590-4599.

Machado, F., Lima, E.L., Pinto, J.C., and McKenna, T.F. (2005). Synthesis of propylene/1-butene copolymers with Ziegler–Natta catalyst in gas-phase copolymerizations, 1. Kinetics and macromolecular properties. **Macromolecular Chemistry and Physics.** 206: 2333-23341.

Machado, F., Lima, E.L., Pinto, J.C., and McKenna, T.F. (2008). In-situ preparation of polypropylene/1-butene alloys using a $MgCl_2$-supported Ziegler–Natta catalyst. **European Polymer Journal.** 44(4): 1130-1139.

Machado, F., Melo, P.A., Nele, M., Lima, E.L., and Pinto, J.C. (2006). Liquid pool copolymerization of propylene/1-butene with a $MgCl_2$- supported Ziegler–Natta catalyst. **Macromolecular Materials and Engineering.** 291: 540-551.

Mandelkern, L., Fatou, J.G., and Ohno, K. (1968). The molecular weight dependence of the crystallization rate for linear polyethylene fractions. **Journal of Polymer Science Part B: Polymer Letters.** 6: 615-619.

Martonák, R., Paul, W., and Binder, K. (1996). Monte Carlo simulation of crystalline polyethylene. **Computer Physics Communications.** 99: 2-8.

Matsumiya, Y., Watanabe H., Urakawa O., and Inoue T. (2016). Experimental Test for Viscoelastic Relaxation of Polyisoprene Undergoing Monofunctional Head-to-Head Association and Dissociation. **Macromolecules.** 49(18): 7088-7095.

Mattice, W.L., and Clancy T.C. (1999). Unperturbed Dimensions and Local Stiffness of Poly(vinyl chloride) with Stereochemical Sequences Composed of Repeating Units. **Macromolecules.** 32: 5444-5449.

Maxfield, J., and Mandelkern, L. (1977). Crystallinity, Supermolecular Structure, and Thermodynamic Properties of Linear Polyethylene Fractions. **Macromolecules.** 10(5): 1141-1153.

Merat, K., Chaodamrongsakul, J., Tanthanuch, W., and Vao-soongnern, V. (2013). Atomistic solvation structure of calcium ion in poly(vinyl alcohol) as studied by Molecular Dynamics simulation and X-ray Absorption Spectroscopy. **Journal of Non-Crystalline Solids.** 371-372: 47-52.

Metropolis, N., Rosenbluth, A.W., Rosenbluth, M.N., Teller, A.H. and Teller, E. (1953). Equation of state calculation by fast computing machines. **Journal of the American Chemical Society.** 21: 1087-1092.

Natta, G., Corradini, P., and Ganis, P. (1960). Chain conformation of polypropylene having a regular structure. **Macromolecular Chemistry and Physics.** 39: 238.

Natta, G., Pino, P., Corradini, P., Danusso, F., Mantica, E., Mazzanti, G., and Moraglio, G. (1955). Crystalline high polymers of a-olefins. **Journal of the American Chemical Society.** 77(6): 1708-1710.

Newville, M., Ravel, B., Haskel, D., Rehr, J.J., Stern, E.A., and Yacoby, Y. (1995). Analysis of multiple-scattering XAFS data using theoretical standards. **Physica B: Condensed Matter.** 208-209: 154-156.

Noro, A., Matsushita, Y., and Lodge T.P. (2009). Gelation Mechanism of Thermoreversible Supramacromolecular Ion Gels via Hydrogen Bonding. **Macromolecules.** 42: 5802-5810.

Noro, A., Matsushita, Y., and Lodge, T.P. (2008). Thermoreversible Supramacromolecular Ion Gels via Hydrogen Bonding. **Macromolecules.** 41: 5839-5844.

Nosé, S. (2002). A molecular dynamics method for simulations in the canonical ensemble. **Molecular Physics.** 100(1): 191-198.

Orwoll, R.A., and Mark, J.E.. (1996). Physical properties of polymer handbook. **Woodbury, NY: American Institute of Physics.**

Owczarek, E., and Hawlicka, E. (2006). Molecular Dynamics Study of $CaCl_2$ in Methanol. **The Journal of Physical Chemistry.** 110: 22712-22718.

Owczarek, E., Rybicki, M., and Hawlicka, E. (2007). Solvation of Calcium Ions in Methanol−Water Mixtures: Molecular Dynamics Simulation. **The Journal of Physical Chemistry.** 111: 14271-14278.

Pandey, A.K., Katiyar, V., Takagi, H., Shimizu, N., Igarashi, N., Sasaki, S., Sakurai. S. (2019). Structural Evolution in Isothermal Crystallization Process of Poly(L-lactic acid) Enhanced by Silk Fibroin Nano-Disc, **Materials.** 12: 1872.

Rapold, R.F., and Mattice, W.L. (1995). New High-coordination Lattice Model for Rotational Isomeric State Polymer Chains. **Journal of the Chemical Society, Faraday Transactions.** 91(16): 2345-2441.

Rapold, R.F., and Mattice, W.L. (1996). Introduction of short and long range energies to simulation of real chains on the 2nnd lattice. **Marcomolecules.** 29: 2457-2466.

Reid, R.C., Prausnitz, J.M. and Poling, B.E.. (1987). The properties of gases and liquids, 4th ed. **New York: McGraw-Hill.**

Rieger, B., Troll, C., and Preuschen, J. (2002). Ultrahigh molecular weight polypropylene elastomers by high activity “dual-side” hafnocene catalysts. **Macromolecules.** 35: 5742-5743.

Roccatano, D., Berendsen, H.J.C., and D’Angelo, P. (1998). Assessment of the validity of intermolecular potential models used in molecular dynamics simulations by extended x-ray absorption fine structure spectroscopy: A case study of $Sr^{2+}$ in methanol solution. **The Journal of Chemical Physics.** 108: 9487-9497.

Rosa, C.D., Auriemma, F., Ballesteros, O.R.D., Resconi, L., and Camurati, I. (2007). Crystallization Behavior of Isotactic Propylene−Ethylene and Propylene−Butene Copolymers: Effect of Comonomers versus Stereodefects on Crystallization Properties of Isotactic Polypropylene. **Macromolecules.** 40: 6600-6616.

Rubinstein, M., and Semenov, A.N. (1998). Thermoreversible Gelation in Solutions of Associating Polymers. 2. Linear Dynamics. **Macromolecules.** 31: 1386-1397.

Rubinstein, M., and Semenov, A.N. (2001). Dynamics of Entangled Solutions of Associating Polymers. **Macromolecules.** 34: 1058-1068.

Rungswang, W., Jarumaneeroj, C., and Chivatanasoontorn, V. (2015). Application of small-angle X-ray scattering (SAXS) via Synchrotron Radiation for structural analysis of semi-crystalline polymer: study cases from polypropylene for industrial usage. **Suranaree Journal of Science and Technology.** 22(3): 265-276.

Rungswang, W., Jarumaneeroj, C., Petcharat, N., Soontaranon, S., and Rugmai, S. (2017). Phase-separation of heterophasic polymer in solution: A model case of impact-resistant polypropylene copolymer. **Journal of Applied Polymer Science.** 134(28): 45069.

Sadler, D.M., and Gilmer, G.H. (1986). Rate-theory of polymer crystallization. **Physical Review Letters.** 56: 2708-2711.

Schick, C., Androsch, R., and Schmelzer, J.W.P. (2017). Homogeneous crystal nucleation in polymer. **Journal of Physics: Condensed Matter.** 29: 453002.

Sequeira, C., and Santos, D. (2010). **Polymer Electrolytes: Fundamentals and Applications.** Woodhead Publishing.

Shao, H.F., Wang, S.L., Dong, X., and He, A.H. (2016). Linear Viscoelastic Behaviors of Polybutene-1 Melts with Various Structure Parameters. Chin. **Journal of Polymer Science.** 34: 174-184.

Strobl, G. (1996). The Physics of Polymer: concepts of understanding their structures and behavior. **Springer.**

Strobl, G.R., Schneider, M.J., and Voight-Martin, I.G. (1980). Model of partial crystallization and melting derived from small-angle X-ray scattering and electron microscopic studies on low-density polyethylene. **Journal of Polymer Science Polymer Physics Edition.** 18: 1361-1381.

Takeuchi, H. (1998). Structure formation during the crystallization induction period of a short chain-molecule system: A molecular dynamics study. **The Journal of Chemical Physics.** 109: 5614-5621.

Tang, Y.J., Guo, M.F., Wang, Q., Ren, M.Q., and Song, W.B. (2012). An In Situ Small-Angle X-Ray Scattering Study of Propylene-Butene and Propylene-Ethylene Random Copolymers during Heating Process. **Macromolecular Symposia.** 312(1): 139–145.

Teo, B. (1986). EXAFS: Basic Principles and Data Analysis, **Springer-Verlag.** Heidelberg.

Utracki, L.A. (1998). Commercial polymer blends. **London: Chapman & Hall.**

van Ruymbeke, E., Vlassopoulos, D., Mierzwa, M., Pakula, T., Charalabidis, D., Pitsikalis, M., and Hadjichristidis, N. (2010). Rheology and Structure of Entangled Telechelic Linear and Star Polyisoprene Melts. **Macromolecules.** 43: 4401-4411.

Verma, R., Marand, H., and Hsiao, B. (1996). Morphological changes during secondary crystallization and subsequent melting in poly (ether ether ketone) as studied by real time small angle X-ray scattering, **Macromolecules.** 29(24): 7767-7775.

Voigt-Martin, I.G., Fischer, E.W., and Mandelkern, L. (1980). Morphology of melt-crystallized linear polyethylene fractions and its dependence on molecular weight and crystallization temperature. **Journal of Polymer Science: Polymer Physics Edition.** 18(12): 2347-2367.

Vonk, C.G., and Kortleve, G. (1967). X-ray small-angle scattering of bulk polyethylene. **Polymer.** 220: 1, 19-24.

Wang, Z.Z, Wu, X.S., and Zhou, G. (2005). Thermal and crystallization behavior of silane-crosslinked polypropylene. **Polymer International.** 54: 442-447.

Watanabe, H. (2001). Dielectric relaxation of type-A polymers in melts and solutions. **Macromoleular Rapid Communications.** 22(3): 127-175.

Watanabe, H. (2009). Slow dynamics in homopolymer liquids. **Polymer Journal.** 41: 929-950.

Watanabe, H. (2012). Fundamental findings in softmatter rheology on the basis of multiple methods. **Journal of the Society of Rheology Japan.** 40(5): 209-222.

Watanabe, H., Chen, Q., Kawasaki, Y., Matsumiya, Y., Inoue, T., and Urakawa, O. (2011). Entanglement Dynamics in Miscible Polyisoprene/Poly(p-tert-butylstyrene) Blends. **Macromolecules.** 44(6): 1570-1584.

Watanabe, H., Ishida, S., Matsumiya, Y., and Inoue, T. (2004). Viscoelastic and Dielectric Behavior of Entangled Blends of Linear Polyisoprenes Having Widely Separated Molecular Weights: Test of Tube Dilation Picture. **Macromolecules.** 37(5): 1937-1951.

Watanabe, H., Matsumiya, Y., and Inoue, T. (2002). Dielectric and Viscoelastic Relaxation of Highly Entangled Star Polyisoprene: Quantitative Test of Tube Dilation Model. **Macromolecules.** 35(6): 2339-2357.

Watanabe, H., Matsumiya, Y., Masubuchi, Y., Urakawa, O., and Inoue, T. (2015). Viscoelastic Relaxation of Rouse Chains undergoing Head-to-Head

Association and Dissociation: Motional Coupling through Chemical Equilibrium. **Macromolecules.** 48: 3014-3030.

Watanabe, H., Matsumiya, Y., van Ruymbeke, E., Vlassopoulos, D., and Hadjichirtdis, N. (2008). Viscoelastic and Dielectric Relaxation of a Cayley-Tree-Type Polyisoprene: Test of Molecular Picture of Dynamic Tube Dilation. **Macromolecules.** 41(16): 6110-6124.

Witkowska, A., Rybicki, J., Panfilis, S.D., and Cicco, A.D. (2006). The structure of liquid lead: EXAFS and MD studies. **Journal of Non-Crystalline Solids.** 352: 4351-4355.

Wunderich, B. (1976). Marcromolecuar physics. **New York: Academic Press.**

Xu, G., and Mattice, W.L. (2000). Rotational isomeric state chains on a high coordination lattice: dynamic Monte Carlo algorithm details. **The Journal of Chemical Physics.** 112: 10049-10055.

Xu, G., and Mattice, W.L. (2001). Study on structure formation of short polyethylene chains via dynamic Monte Carlo simulation. **Computational and Theoretical Polymer Science.** 11(6): 405-413.

Xu, W., Martin, D.C., and Arruda, E.A. (2005). Finite strain response, microstructural evolution and b → a phase transformation of crystalline isotactic polypropylene. **Polymer.** 46: 455-470.

Yabe, M., Mori, K., Ueda, K., and Takeda, M. (2019). Development of PolyPreGen software to facilitate the determination of molecular dynamics simulation parameters for polymers. **Journal of Computer Chemistry, Japan-International Edition.** 5: 2018-0034.

Yamamoto, T. (1997). Molecular dynamics simulation of polymer crystalliza¬tion through chain folding. **The Journal of Chemical Physics.** 107: 2653-2663.

Yu, H., Krejchi, M.T., Shah, C.D., Myers, C.L., and Waymouth, R.M. (1998). Elastomeric polypropylenes from unbridged (2-phenylindene) zirconocene catalysts. **Macromolecules.** 31: 6908.

Yue, K., Liu, G., Feng, X., Li, L., Lotz, B. and Cheng, S.Z.D. (2018). A few rediscovered and challenging topics in polymer crystals and crystallization. **Polymer Crystallization.** 1: e10053.

Zeng, W., Liu, J.C., Zhou, J.F., Dong, J.Y., and Yan, S.K. (2008). A comparison study on the melt crystallization kinetics of long chain branched and linear isotactic polypropylene. **Chinese Sciences Bulletin.** 53(2): 188-197.

# APPENDIX

# APPENDIX

# PAPER PRESENTATIONS

## The 10th International Polymer Conference of Thailand (PCT-10) August 6-7, 2020

## Synchrotron SAXS/WAXD and DSC studies of melt crystallization kinetics of short branched and linear isotactic polypropylene

**Natchamon Sukhonthamethirat**[1] Siriwat Soontaranon[2], Supagorn Rugmai[2] and Visit Vao-soongnern[1*]
[1]Laboratory of Computational and Applied Polymer Science, School of Chemistry, Institute of Science, Suranaree University of Technology
[2]Synchrotron Light Research Institute, Nakhon Ratchasima 30000
Phone +66 4422 4639, Fax +66 4422 4185, [*]E-Mail: visit@sut.ac.th

**Abstract**

The isothermal and non-isothermal crystallization kinetics of short branched **(**SBPP) and linear isotactic polypropylene (L-iPP) were investigated by Synchrotron small/wide angle X-Ray scattering/diffraction (SAXS/WAXD) and differential scanning calorimetry (DSC). SBPP samples contain few amount of 1-butene randomly placed onto polypropylene chains and L-iPP was used for comparison. Three polymer samples were used having similar molecular weights around 233k, 283k and 236k g/mol with polydispersity index about 7.7, 7.3 and 6.8 and the melt flow rates (MFR under 230°C/2.16 kg) are 16, 12 and 18 g/10 min for L-iPP and two SBPP denoted by V30G, MT12-s and MT18-s, respectively. DSC results for the non-isothermal crystallization process show that the crystals of SBPP grow slower (MT12-s < MT18-s) than the crystals of L-iPP. The SBPP gives lower crystallinity than that of L-iPP. Avrami, Ozawa and Mo models were used to analyze the non-isothermal crystallization kinetics. The fitting results indicates that only Avrami and Mo models can give linear lines. From Avrami results, the crystal dimention for V30G is closed to 3D while SPBB exhibits more likely toward 2D. The analyses of the non-isothermal crystallization processes indicate an increment in crystallization rate with increasing cooling rate. But at any cooling rate, L-iPP crystallizes more quickly than the SBPP. In addition, the melt isothermal crystallization behavior was investigated for SBPP and L-iPP by means of simultaneous small-angle X-ray scattering SAXS/WAXD measurements using synchrotron radiation source at Nakhon Ratchasima. The electron density correlation function was calculated to estimate the lamellae with long period of *ca*. 18 (V30G) and 24 (MT12-s and MT18-s) nm were formed and stabilized. SBPP has thicker amorphous region than L-iPP while the crystal thickness are about the same. These results suggest that the short branch defects cannot incorporate into the crystalline structure of isotactic polypropylene but should be excluded to the amorphous region. The degree of crystallinity determined by WAXD also give smaller values for SBPP as MT18-s (31.03) $\leq$ MT12-s (31.32) < V30G (46.24).

**Keywords:** polypropylene, SAXS/WAXD, DSC, crystallization

## 1. Introduction

As one of the most widely used polyolefin materials, isotactic polypropylene (*i*PP), firstly synthesized by Natta *et al.*[1,2] possesses attractive features like high strength, excellent chemical resistance, good process ability and reasonable price.[3] However, the applications of PP have been limited due to its poor impact strength, especially at low temperature. There are numerous attempts to improve the impact properties of PP resins through physical or chemical methods. As isotactic poly(1-butene) (*i*PB), with a similar molecular structure to *i*PP, has some advantages compared to *i*PP, copolymerization of 1-butene units to *i*PP chain in random pattern might be a possible method to improve properties of iPP. In this work, G-resin (SINOPEC) which is the commercial thermoplastic brand of iPP containing some amount of 1-butene will be investigated for the effect of short branch defects on the crystallization characteristics of isotactic polypropylene. G-resin exhibits high transparency and relatively low soluble content for food package and medical articles. The chemical confinement effect of 1-butene co-monomers on the crystallization behaviors of statistical copolymers should be an important issue for polyolefin products.[4] In this report, we employ differential scanning calorimeter (DSC) and synchrotron Small/Wide Angle X-ray Scattering/Diffraction (SAXS/WAXD) to study the crystallization and morphological changes of commercial iPP and poly(propylene-co-1-butene) samples.

## 2. Materials and methods

### 2.1 Samples

All polymer samples were kindly provided by Beijing Research Institute of Chemistry and Industry, SINOPEC, China. MT12-s and MT18-s G-resins have some 1-butene defects whereas V30G is isotactic PP used for comparison. The melt flow rates (MFR under 230°C/2.16 kg) are 16, 12 and 18 g/10 min for V30G, MT12-s and MT18-s, respectively.[5] Molecular weight and molecular weight distribution determined using GPC-IR5 (Polymer Char with infrared detector. and the results are Mn (PDI) = 30,407 (7.68), 38,567 (7.33) and 34,753 (6.81) g/mol for V30G, MT12-s and MT18-s, respectively.

### 2.2 DSC

The melting temperature ($T_m$), crystallization temperature (Tc), enthalpy of crystallization ($\Delta H_c$) and percentage crystallinity of polypropylene were investigated using NETZSCH DSC204 F1 Phoenix calibrated with indium sample. The weights of all samples used for DSC measurements were 6-10 mg loaded using aluminum pans. Samples for non-isothermal crystallization were heated from 50°C to 200 °C and hold for 5 min to erase the previous thermal history. Then the samples were cooled down to 50°C at various cooling rates (5, 10, 15, 20, 25 and 30 °C/min). All measurements were done under nitrogen atmosphere.

### 2.3 SAXS/WAXD

Isothermal crystallizations of V30G, MT18-s and MT12-s were investigated using BL1.3W beamline of Synchrotron Light Research Institute, Nakhon Ratchasima, Thailand. The 2D-SAXS patterns were recorded by the Mar SX165 CCD detector. SAXS measurement was performed at the sample-to-detector distance (SDD) of about 4.5 m. Styrene-ethylene-butadiene-styrene block copolymer (SEBS) with d = 32.8 nm was used as a standard material for calibrating the scattering angle. The WAXD measurement was performed at the SDD of about 0.2 m, where the calibration was carried out by 4-bromobenzoic acid with a spacing of 0.47 nm. The X-ray wavelength was fixed at 0.138 nm. An ionization chamber installed in front of the sample holder and a photodiode attached in front of a beam stop were used to monitor the beam intensity before and after the sample, respectively. The samples were filled into the sample cell with Kapton windows. During the isothermal crystallization experiment, the samples were heated from room temperature to 200°C and held for 5 min to completely eliminate any possible crystalline phase. After that, the samples were quenched to 132°C (crystallization temperature) with cooling rate 4°C/min. SAXS measurements were carried out at different crystallization times (0, 5, 10, 15, 20, 25, 30, 35, 40, 45, 50, 55, 60 min) with the exposure time of 120 s. The 2D-SAXS patterns were reduced to 1D-SAXS profile by circularly averaging the 2D patterns using the SAXSIT program. SAXS data were analyzed using the 1D-electron density correlation function using SasView 4.2.1 to determine the parameters of semi-crystalline morphologies of all samples.

## 3. Results and discussion

### 3.1 DSC

The characteristic data including crystallization onset temperature ($T_i$), crystallization peak temperature ($T_p$), and the enthalpy of crystallization ($\Delta H_c$) are summarized in Table 1. Both the crystallization onset and peak temperatures have a tendency shift to lower temperature with increasing cooling rate. The half-time of non-isothermal crystallization ($t_{0.5}$) decrease with the increasing cooling rates. Adding short branch defect causes slower crystallization. Next, Avrami, Ozawa and Mo models were employed to analyze the non-isothermal crystallization kinetics. The fitting results indicates that only Avrami (Figure 1) and Mo models (Figure 2) can give linear lines. For Avrami model, Crystallization rate constant (Z) is increased with faster cooling rate. Although the exponent ($n$) shows scattered data in broader range, *n* for V30G is larger than other samples at the same cooling rate. For Mo model, the F(T) values are increased with the increase of relative crystallinity. The larger the relative crystallinity required to attain at a unit time is, the faster the required cooling rate will be.

In overall, DSC results for non-isothermal crystallization process show that the crystals of SBPP grow slower than L-iPP. This may be from the lower chain diffusion rate of SBPP due to the existence of butene defects. SBPP also exhibits lower enthalpy of crystallization than that of L-iPP. This might be related to the higher nucleation ability of SBPP since the crystallization process of both SBPP and L-iPP should be nucleation-dominated. Avrami analysis indicates that The crystal dimension for V30G is closed to 3D while SPBB exhibits more likely toward 2D. The analyses of the non-isothermal crystallization processes indicate an increment in crystallization rate with increasing cooling rate. But at any cooling rate, L-iPP crystallizes more quickly than the SBPP. This implies that the non-isothermal crystallization processes of SBPP and linear-iPP are diffusion-dominated, in which the lower chain diffusion rate of SBPP results in slower crystallization.

**Table 1** Non-isothermal crystallization parameters

| Sample | Cooling rate (°C/min) | Ti (°C) | Tp (°C) | ΔHc (J/g) |
|---|---|---|---|---|
| V30G | 5 | 111.8 | 114.6 | -99.1 |
| | 10 | 106.8 | 111.0 | -97.9 |
| | 15 | 102.9 | 108.8 | -95.1 |
| | 20 | 99.5 | 106.9 | -93.7 |
| | 25 | 97.6 | 106.0 | -98.3 |
| | 30 | 97.5 | 106.1 | -92.4 |
| MT18-s | 5 | 118.6 | 123.1 | -69.9 |
| | 10 | 112.4 | 119.6 | -75.6 |
| | 15 | 108.2 | 117.0 | -74.5 |
| | 20 | 102.3 | 114.4 | -80.9 |
| | 25 | 100.5 | 112.8 | -78.2 |
| | 30 | 99.4 | 112.6 | -77.1 |
| MT12-s | 5 | 116.8 | 124.4 | -74.4 |
| | 10 | 115.3 | 121.5 | -93.3 |
| | 15 | 113.4 | 119.7 | -73.1 |
| | 20 | 112.3 | 118.3 | -71.3 |
| | 25 | 110.3 | 117.1 | -71.0 |
| | 30 | 109.4 | 116.0 | -70.2 |

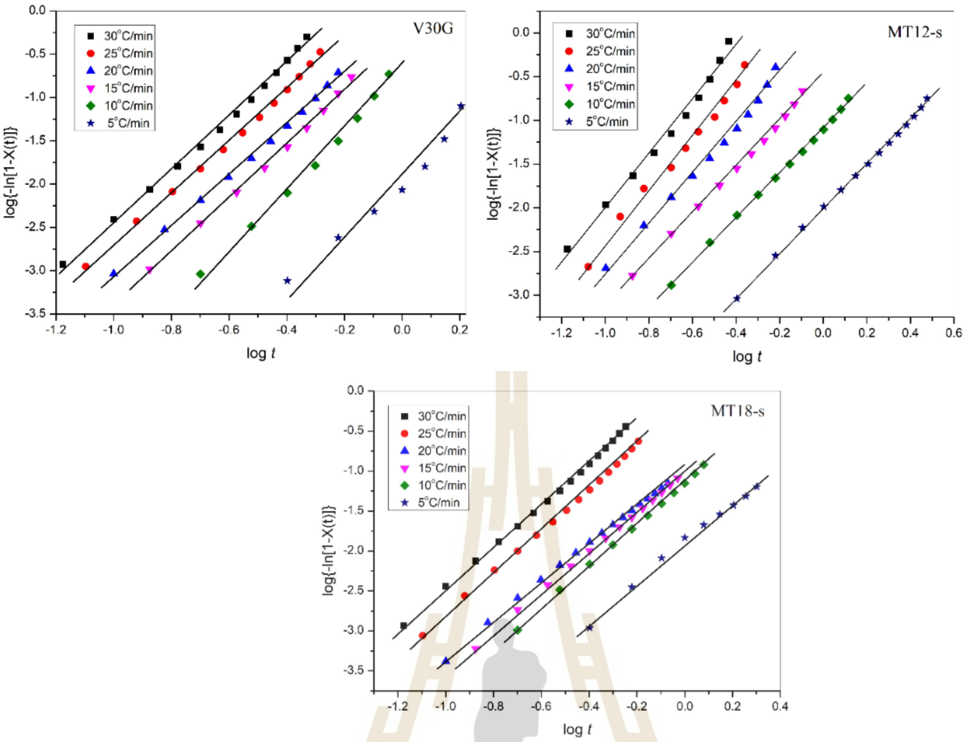

Figure 1 Avrami plots at different cooling rates.

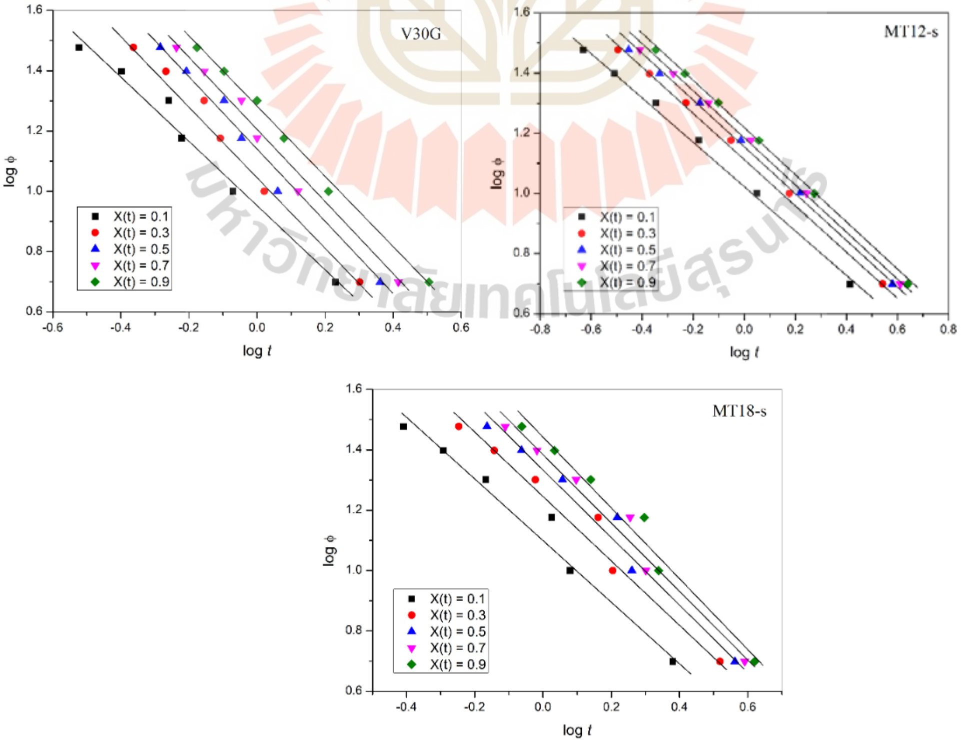

Figure 2 Mo plots at different relative crystallization.

### 3.2 SAXS

The melt isothermal crystallization behavior was investigated for SBPP and L-iPP by means of simultaneous small-angle X-ray scattering SAXS/WAXD measurements using synchrotron radiation source at Nakhon Ratchasima. The Lorentz-corrected SAXS profiles of V30G, MT18-s and MT12-s at 132°C for different crystallization times are determine (Figure not shown). The evolution of the first scattering peak of V30G is the slowest indicating that V30G has longer induction time compared to MT18-s and MT12-s. Considering the overall data of all samples in the same $Iq^2$ scale, the scattering peak of V30G is significantly higher than other samples implying larger amount of crystallinity of V30G compared to MT18-s and MT12-s. The crystallization proceeds rapidly at initial time (0-5 minutes). After about 20 min, the scattering peak of V30G did not show any difference indicating that the crystallization process of V30G seemed to be finished after 15 min whereas the slight increase in the intensity was observed for MT18-s and MT12-s. The SAXS intensity of MT12-s is quite constant at 40 min, but continues to change after 60 minutes for MT18-s. The lamellar parameters can be evaluated using the 1D-electron density correlation function, $K_{(z)}$. This method can be used to determine the long period ($L_p$), as shown in figure 3 and give 18 nm and 24 nm for V30G and MT18-s/MT12-s. SBPP has thicker amorphous region than L-iPP while the crystalline thickness are about the same. These resuls suggest that the short branch defects cannot incorporate into the crystal structure of isotactic polypropylene but should be excluded to the amorphous region.

### 3.3 WAXD

PP is capable of crystallizing in three polymorphic forms, α (monoclinic), β (pseudohexagonal), and γ (triclinic), with α-crystal being the most stable structure. The WAXD patterns of all PP samples are shown in Fig. 4. The diffractogram of PP indicated that the strong diffraction peaks located at 2θ of 12.2, 14.5, 16.1, 18.5, 19.0 and 22.0, correspond to the α (110), α (040), α (130), α (111), and α (131) planes, respectively. However, the diffraction peak at 2θ of 17.1 appears for MT18-s and MT12-s. For WAXD profiles indicating that the unit cell of polymer may be changed. The degree of crystallinity can be calculated using the equation. [6]

$$\emptyset_{\mathrm{WAXS}} = \frac{\sum \mathrm{A_c}}{\sum \mathrm{A_C} + \mathrm{A_a}} \qquad (1)$$

where $\sum A_c$ is the summation of the peak area of the crystalline peaks and $A_a$ is the peak area of the amorphous halo. The percent of crystallinity are 46.24, 31.32 and 31.03 for V30G, MT12-s and MT18-s, respectively. This result indicate that 1-butene defects hinder the crystallization process of iPP.

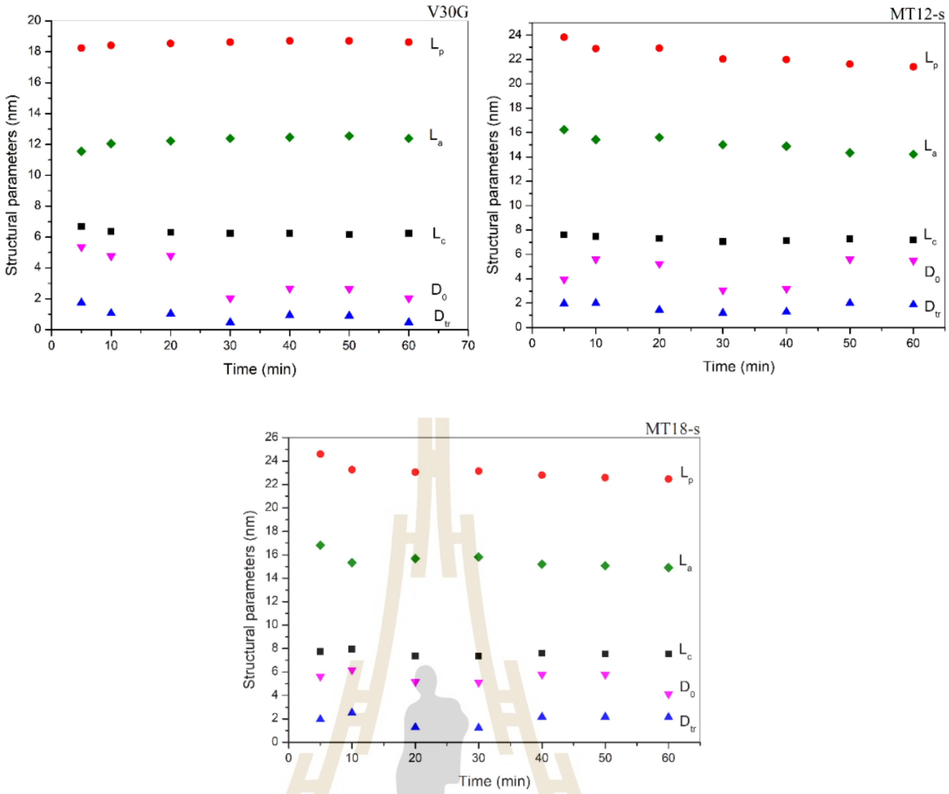

Figure 3 Structural parameters under isothermal crystallization at 132°C from fitting 1-D electron density correlation function for lamellar parameter evaluation.

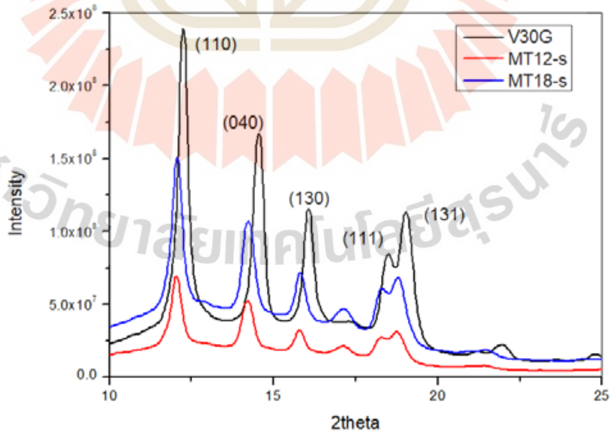

Figure 4 WAXD diffractogram of PP samples.

## 4. Conclusion

The isothermal and non-isothermal crystallization kinetics of short branched **(**SBPP) and linear isotactic polypropylene (L-iPP) were investigated by Synchrotron small/wide angle X-Ray scattering/diffraction (SAXS/WAXD) and differential scanning calorimetry (DSC). The crystalization of SBPP is slower and has lower crystallinity than that of L-iPP. Avrami and Mo models can give reasonble fitting for the non-isothermal crystallization kinetics. The crystal dimension changed from 3D toward 2D for branch samples. At the same cooling rate, L-iPP crystallizes faster than the SBPP. Based on SAXS results, SBPP has thicker amorphous region than L-iPP while the crystal thickness are about the same. The degree of crystallinity determined by WAXD also give smaller values for SBPP.

## 5. Acknowledgement

We thank SINOPEC (China) for polymer samples and IRPC Public Company Limited for GPC and DSC measurement.

## 6. References

1. Natta G., Pino P., Corradini P., Danusso F., Mantica E., Mazzanti G., Moraglio G. Crystalline high polymers of a-olefins. *J. Am. Chem. Soc.* **1955**, 77, 6, 1708–1710.
2. Corradini P. The discovery of isotactic polypropylene and its impact on pure and applied science. *J. Polym. Sci.* **2003**, 42, 3, 391–395.
3. Lu D.P., Guan R. Properties of Isotactic Polypropylene and iPP/Talc Blends Functionalized by Electron Beam Irradiation. *Polym. Int.* **2000**, 49, 1389-1394.
4. Hu W., Mathot V., Alamo R., Gao H., Chen X. Crystallization of statistical copolymers. *Adv Polym Sci.* **2016**.
5. Duenpen Kalapat, Qiyun Tang, Xiaohong Zhang, Wenbing Hu. Comparing crystallization kinetics among two G-resin samples and iPP via Flash DSC measurement. *J. Therm. Anal. Calorim.* **2017**,128, 1859-1866.
6. Amit Kumar Pandey, Vimal Katiyar, Hideaki Takagi, Nobutaka Shimizu, Noriyuki Igarashi, Sono Sasaki, Shinichi Sakurai. Structural Evolution in Isothermal Crystallization Process of Poly(L-lactic acid) Enhanced by Silk Fibroin Nano-Disc, *Materials.* **2019**, 12, 1872.

Preferred type of talk (Oral, Poster): **Oral**
Preferred conference session: **Advanced and Functional Polymers**

The 21st International Union of Materials Research Societies –
International Conference in Asia (IUMRS-ICA2020), February 23-26,
2021

# Isothermal crystallization and some rheological properties of linear and branched isotactic polypropylene

Natchamon Sukhonthamethirat[1] Shinichi Sakurai[2], Shigeru Okamoto[3],
Visit Vao-soongnern[1*]
[1]*Laboratory of Computational and Applied Polymer Science, School of Chemistry, Institute of Science,*
*Suranaree University of Technology, Nakhon Ratchasima 30000, Thailand*
[2]*Department of Biobased Materials Science, Kyoto Institute of Technology, Matsugasaki, Sakyo-ku, Kyoto, 606-8585, Japan*
[3]*Nagoya Institute of Technology, Gokiso-cho, Showa-ku Nagoya 466-8555, Japan*
*Corresponding Author's E-mail: visit@sut.ac.th

---

**Abstract**

Isothermal crystallization kinetics of short branched (SBPP) and linear *isotactic* polypropylene (L-*i*PP) were investigated using Synchrotron SAXS/WAXD and DSC. SBPP samples contain few amount of 1-butene randomly placed in *i*PP chain. All polymers have similar molecular weights which were 233k, 283k and 236k g/mol with PDI = 7.7, 7.3, 6.8 and MFR at 230°C/2.16 kg = 16, 12, 18 g/10 min for L-*i*PP and two SBPP, denoted by V30G, MT12-s and MT18-s, respectively. DSC isothermal crystallization showed that SBPPs crystallize slower *i.e.* crystallization rate was in the order as L-*i*PP > MT12-s ≥ MT18-s. The crystallinity for SPBBs are also lower than L-*i*PP. Avrami model was used to analyze the isothermal crystallization kinetics. Simultaneous synchrotron SAXS/WAXD were also used to study melt isothermal crystallization. The eletron density correlation function was calculated to estimate the lamellar thickness. The long period (*D*) of L-*i*PP and two SBPP samples are around 19, 25.8, 25.8 *nm* for V30G, MT12-s and MT18-s, respectively. SBPP samples have larger amorphous portion, higher crystalline thickness (*L*) but *L*/*D* is lower than L-*i*PP. It seems that the short branch (1-butene) defects can not be incorporated into the crystalline structure of isotactic polypropylene but should be excluded to the amorphous region. The degree of crystallinity by WAXD also give smaller values for SBPP *i.e.* MT18-s (31%) ≈ MT12-s (31%) < V30G (> 50%). The effect of molecular structure of PP on the dynamic mechanical analysis showed that storage (E') modulus was lower at all temperature for branched PP while loss (E") modulus was higher at $T$

< 50 $^{o}$C. The slope of G’ in the plot of G’ vs shear rate for branched PP was almost the same, but seemed to be larger than that of L-*i*PP at low frequency whereas it was almost the same for G”. Zero shear viscosity is larger for branched sample.

Keywords: Polypropylene; branched polymer; SAXS/WAXD; crystallization.

Preferred type of talk (Oral, Poster): **Oral**
Preferred conference session: **R1 Rheology**

**International Polymer Characterization Forum (POLY-CHAR 2020) April 12-14, 2021**

# Effect of few 1-butene defects on isothermal crystallization and morphology of isotactic polypropylene

Natchamon Sukhonthamethirat[1] Shinichi Sakurai[2], Shigeru Okamoto[3],
Visit Vao-soongnern[1]

[1] *Laboratory of Computational and Applied Polymer Science, School of Chemistry, Institute of Science, Suranaree University of Technology, Nakhon Ratchasima 30000, Thailand.*
[2] *Department of Biobased Materials Science, Kyoto Institute of Technology, Matsugasaki, Sakyo-ku, Kyoto, 606-8585, Japan.*
[3] *Department of Materials Science and Engineering, Nagoya Institute of Technology, Gokiso-cho, Showa-ku Nagoya 466-8555, Japan.*
*email: natchamon.nach@gmail.com, visit@sut.ac.th*

## Abstract

Isothermal crystallization of *isotactic* polypropylene with few amount of 1-butene **(**1BPP**)** and linear chain (L-*i*PP) was investigated by synchrotron small- and wide-angle X-ray scattering/diffraction (SAXS/WAXD) and differential scanning calorimetry (DSC)**.** One linear and two branched samples, denoted by V30G, MT12-s and MT18-s, respectively, have similar molecular weights of 233k, 283k and 236k g/mol with PDI = 7.7, 7.3, 6.8 and MFR at 230°C/2.16 kg = 16, 12, 18 g/10 min**.** The content of 1-butene in MT12-s and MT18-s are 6.43 and 5.20 wt**%.** Avrami analysis of DSC isothermal crystallization suggests that the dimension crystal growth (*n*) and the crystallization rate (*k*) tend to increase for 1BPP**.** For the SAXS analysis, the eletron density correlation function was used to estimate the repeating period ($L_p$) and the average thickness of lamellae ($L_c$)**.** The $L_p$ is increased for 1BPP (from 19 to 25.8 *nm*)**.** In general, SBPP samples have higher amorphous (*La*) and $L_c$ but lower *Lc*/*Lp* ratio than L-*i*PP**.** Namely, the degree of crystallinities are lower for 1BPP**.** The diffraction peak of monoclinic α

forms can be detected in all PP samples whereas the orthorhombic γ forms were found only for 1BPP.

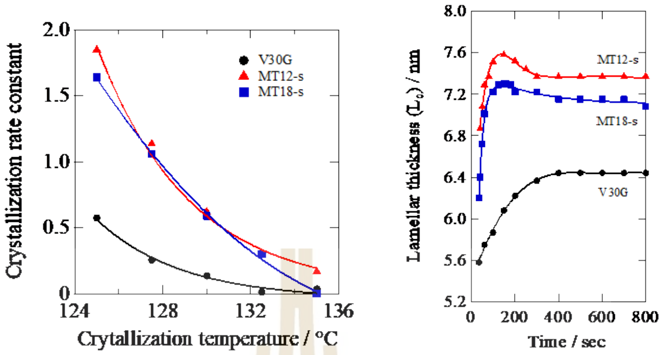

Figure 1 Crystallization rate constant (*k*) and lamellar thickness (*Lc*) of isotactic polypropylene with linear vs branched structures with 1-butene defects.

## Acknowledgements

VV and NS thank *IRPC Public* Company Limited for GPC analysis and Neha Manojkumar Mulchandani (KIT) for NMR measurement.

## References

[1] D. Kalapat, Q. Tang, X. Zhang, and W. Hu, J. Therm. Anal. Calorim. 2017, 128, 1859-1866.

[2] Y.J. Tang, M.F. Guo Q. Wang, M.Q. Ren and W.B. Song, Macromol. Symp. 2012, 312(1), 139–145.

Preferred type of talk (Oral, Poster): **Oral**

Preferred conference session: **SESSION G: Polymer Physics, Theory and Simulations**

# CURRICULUM VITAE

Natchamon Sukhonthamethirat was born on October 4, 1996 in Nakhon Ratchasima, Thailand. She earned her Bachelor’s Degree in Chemistry from Suraneree University of Technology (SUT) in 2019. She then continued her Master’s degree in Chemistry at School of Chemistry, Institute of Science at Suranaree University of Technology. Her expertise includes the frame work of polymer characterization, polymer crystallization and molecular simulation techniques (Monte Carlo (MC) and Molecular Dynamic (MD) simulation). During Master’s degree study, she was a student intern at Institute for Chemical Research (ICR), Kyoto University, and Department of Biobased Materials Science, Kyoto Institute of Technology, Japan. She presented poster and short oral presentation entitled of “Molecular simulation of the stereochemistry effect on structural and dynamic properties of polypropylene melts” in The 14th International Workshop for East Asian Young Rheologists (IWEAYR-14). She also presented oral presentation entitled of “Effect of few 1-butene defects on isothermal crystallization and morphology of isotactic polypropylene” in The international Polymer Conference of Thailand (PCT-10), The 21st International Union of Materials Research Societies - International Conference in Asia (IUMRS-ICA 2020) and IUPAC POLY-CHAR 2020 [Venice, Italy] - International Polymer Characterization forum. She published one paper, one is “Synchrotron SAXS/WAXD and DSC studies of melt crystallization kinetics of short branched and linear isotactic polypropylene” in PCT-10 proceeding book.